Understanding Silicon Nanowire Field-Effect Transistors for Biochemical Sensing

Inauguraldissertation

zur
Erlangung der Würde eines Doktors der Philosophie
vorgelegt der
Philosophisch-Naturwissenschaftlichen Fakultät
der Universität Basel

von

Ralph Lukas Stoop
aus Schänis SG

Basel, 2016

Genehmigt von der Philosophisch-Naturwissenschaftlichen Fakultät
auf Antrag von
Prof. Dr. C. Schönenberger
PD Dr. M. Calame
Prof. Dr. N. Clément
Prof. Dr. S. Ingebrandt

Basel, den 13. Oktober 2015

Prof. Dr. Jörg Schibler
Dekan

Contents

Introduction

The capability to respond to external stimuli is a main element of living systems. Leaves of a plant turning towards the sun or a mouse escaping from a hungry snake are only two examples of this aspect of nature. Over thousands of years, evolution has led to an enormous diversity of senses with incredible capabilities including the detection of physical stimuli such as sunlight, temperature or pressure and chemical stimuli such as odor or taste. Not surprisingly, the successful concept of sense has been applied to the technical world leading to the *sensor*: A transducer which detects a specific quantity of the environment. Although the application of sensors goes back centuries, their importance has increased tremendously during the past decades. After the digital revolution completely changed processing, storing and exchanging information, a sensor revolution is considered to change the way information is generated [1]. As the usual suspect, silicon (Si) technology is believed to play again a vital part. Physical sensors have already benefit greatly from Si technology as accelerometers, gyroscopes or cameras integrated in today's smartphones prove. The advantages of Si sensors are their simplicity, established fabrication at low cost, simple electronic interfacing and their potential to be integrated in portable devices. The hope that a similar success could be repeated in the field of chemical and biochemical sensors is obvious.

These sensors give information about the composition of a gas or a solution and their demand is growing rapidly. In many western countries, the aging population and the resulting need for prevention, monitoring and treatment of chronic diseases requires specialists operating sophisticated equipment. As a result, the health care costs are currently exploding. State-of-the-art methods often have sufficient accuracy for various applications (e.g. magnetic resonance spectroscopy for cancer screening). However, their operation requires trained specialists. This complicates the early detection of diseases, because patients have to visit the doctor or hospital, even in the absence of symptoms. The current technology is challenging to

be integrated in portable devices. In developing countries, environmental monitoring, in particular for improving and maintaining the drinking water quality and monitoring urban air pollution, requires cheap biochemical sensors. In conclusion, cheap, easy-to-operate chemical and biochemical sensors for medical diagnostics, personalized medicine, point-of-care diagnostics and environmental monitoring would have a huge beneficial impact on society all over the world.

Silicon field-effect transistors (Si FETs) are promising candidates for electronic biochemical sensors due to their potentially cheap fabrication in a CMOS-compatible process. Advances in micro- and nanofabrication techniques allow downscaling their size to the nanoscale leading to highly integrated sensor arrays. In particular FETs based on Si nanowires (SiNWs) are under intense focus in research. In combination with recent progress in microfluidics, the implementation of a multifunctional sensing platform or a *lab-on-a-chip* seems to be feasible in the near future. The function principle is based on the ion-sensitive field-effect transistor (ISFET) invented by P. Bergveld in the 1970's[2]. The idea of having the gate dielectrics of the sensor in direct contact with the analyte solution has led to a large number of publications demonstrating pH and ionic sensing[3–7] and various biological sensing including protein-ligand kinetic studies[8], DNA sensing[9–12] and even DNA sequencing[13]. Disregarding the specific application, the working principle is based on the change of the surface potential induced by charges adsorbed at the sensor surface which influences the electrostatic gating of the transistor.

Until today, commercial products based on ISFETs are using the device as a pH sensor only, despite the promising results obtained in biochemical sensing experiments. The reason for this development lies in the incomplete understanding of the complex interface between the electrolyte and the solid-state sensor. In particular, the role of the surface material and its interaction with the electrolyte have to be elaborated in further studies. Additionally, a discussion of the most important limitations and parameters to optimize the sensor performance is needed. This includes the discussion of the role of the device geometry on the performance of the sensor and the potential benefits of nanostructured objects used as ISFETs.

In this PhD project, we address these points by studying arrays of SiNW ISFETs and investigate their potential as an integrable sensing platform. The results of the project are presented in Part I of this thesis. The measurements were obtained in the *Nanoelectronics Group* at the *University of Basel* in collaboration with other research groups, which are mentioned in

the text correspondingly. In Part II of the thesis, we expand our search for approaches for biochemical sensing even further. Thereby, the conductive polymer poly(3,4-ethylenedioxythiophene):polystyrene sulfonate (PEDOT:PSS) was investigated for future sensing applications in collaboration with the *University of Valencia*.

Part I of this thesis starts with a general introduction of biochemical sensors and compares the ISFET with the classical ion-selective electrode (ISE) in Chapter 1. When studying biochemical sensors, the question arises what the ideal sensor actually is and how it could be realized. The ideal chemical sensor is not only capable of detecting a single entity of the analyte (a single ion, molecule, protein or other structure). It should also allow to measure a large change in concentration of the analyte. One is tempted to say that the ideal sensor has single analyte sensitivity over the whole concentration of interest. Such a sensor would have a linear output characteristic, with the slope given by the change in signal per adsorption of a single species. However, for large concentration changes in the analyte solution, this system would lead to huge output signals which could not be handled by any electronics. Therefore, the ideal sensor might be extremely sensitive (single entity) when exposed to small analyte concentrations but much less sensitive at higher concentrations. This is only achieved with a non-linear output characteristics. As we will see in the beginning of Chapter 1, the ISFET fulfills these requirements, if it exhibits a Nernstian response. In Chapter 1, the experimental details of this PhD work are also given. The chapter finally closes with a theoretical discussion of limitations of the sensing platform and how they lead to a deviation from the ideal behavior. The ideal sensor should also display perfect selectivity, meaning that only the targeted species gets adsorbed at the sensor surface, leading to a change in sensor signal. In Chapter 2, we present our approach of using gold-coated SiNW ISFETs functionalized with self-assembled monolayers of functional molecules as selective ion sensors. The limitations present in our SiNWs are discussed in Chapter 3 focusing on competing reactions at the electrolyte/sensor interface and the electrical noise of the transistor. Finally, in Chapter 4, we demonstrate successful detection of a clinically relevant protein using gold-coated SiNWs.

Besides the ongoing research to expand the possibilities of Si-based devices to biochemical sensing, another part of the scientific community is working on alternative approaches for sensing devices. Organic transistors are promising due to their ease of fabrication, bio-compatibility and the possibility of combining them with flexible substrates. A very interesting member of the organic transistor family is based on the reversible

exchange of ions with an electrolyte modulating the conductivity of the transistor channel. This concept is called the organic electrochemical transistor (OECT) and has been applied to various biosensing applications [14–16]. Part II of this thesis summarizes the progress obtained in a collaboration with the *University of Valencia*. In this collaboration the noise properties of organic electrochemical transistors based on PEDOT:PSS are investigated. In Chapter 5 the working principle is introduced and two different fabrication techniques are presented. In Chapter 6 the noise of PEDOT:PSS OECTs is discussed and compared with the noise of our SiNW platform.

Part I

Arrays of Silicon Nanowires for Biochemical Sensing

<div style="text-align: right">

1

</div>

Basic Terminology and Methods

1.1 Basic Concepts and ISFET Theory

In this section, a short introduction to (bio-)chemical sensing using ion-sensitive field-effect transistors (ISFETs) is provided. Starting from a general overview of potentiometric chemical sensing, the ISFET concept is introduced. Special focus is put on the difference between the ISFET and its predecessor, the classical ion-selective electrodes (ISE). Two common models explaining the pH response of ISEs and ISFETs are presented.

1.1.1 An Introduction to Potentiometric Sensing

Generally, a biochemical sensor provides information about the composition of its environment which is either a liquid or a gas phase. The latter case of a gas phase is excluded from this thesis. When studying biochemical sensors in the following, we assume a system as represented in Figure 1.1 which consists of a transducer with a sensitive layer and the analyte solution. The sensing process can be divided into two steps, recognition and transduction. In the recognition step, the targeted analyte interacts selectively with the sensing layer which leads to the adsorption of the target at the sensor surface. The adsorption event leads to a change of different physical parameters which can be detected and transduced as a sensor output signal in the transduction step. The choice of the physical parameter being read out in the transduction step greatly determines the performance of the sensor.

One established group of biochemical sensors is based on the change of

optical properties in the vicinity of the sensor surface. For example, state of the art plasmon spectroscopy sensors (Biacore system, *GE healthcare*) read out the adsorption as a shift in the plasmon resonance frequency of the optically excited electron oscillations at the sensor surface. Another possibility is to read out the mass change due to the adsorption of the targeted species as a shift of the resonance frequency used in quartz crystal microbalances. The ISFET studied in this part of the thesis belongs to the group of potentiometric (bio-)chemical sensors. Generally, potentiometric sensors measure the electrical potential difference ϕ_i at a solid/liquid interface as function of the concentration of the chemical species. Detecting the charge of targeted species rather than the mass or optical properties is beneficial for the detection of very small, charged species, in particular ions.
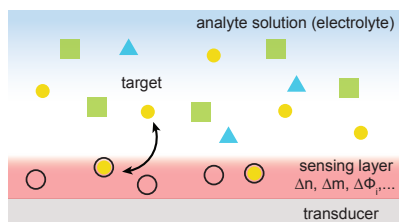
Figure 1.1: Concept of biochemical sensing. Adsorption of chemical species leads to a change of optical properties (e.g. Δn), mass (Δm) or interfacial potential ($\Delta \phi_i$) which is read out by the transducer.

1.1.2 From Ion-Selective Electrodes to Ion-Sensitive Field-Effect Transistors

When introducing the ISFET, a discussion of ion-sensitive electrodes is a good starting point. Ion-selective electrodes (ISEs) have been used in analytical chemistry for over 100 years [17]. Its most prominent member is the glass electrode, which is used for pH sensing in standard pH-meters [18,19]. Constant efforts have been taken to increase their sensitivity and stability. By changing the properties of the sensing layer (usually called membrane in the case of ISEs), ISEs for several ions, mostly metallic cations such as (Na^+), potassium (K^+), calcium (Ca^{2+}), etc. have been developed [20]. Figure 1.2a shows the schematic of an ISE with the sensing layer (for pH electrodes a glass membrane, for other ions it might be an organic mem-

brane) in contact with the analyte solution on one side and with the internal reference solution on the other side. From measuring the potential difference ϕ_{meas} between the two electrodes, the concentration of the targeted species can be obtained. Fundamentally, the maximum possible change of ϕ_{meas} upon a change of the target analyte[1] $\Delta p = \log(c_2/c_1)$ when changing the concentration of the target from c_1 to c_2 is limited by the Nernst equation given by

$$\Delta\phi_{meas} = \frac{2.3kT}{ze} \cdot \Delta p \qquad (1.1)$$

with k the Boltzmann constant, T the absolute temperature, e the electronic charge and z the charge number of the targeted species. Therefore, the ideal Nernstian response of a pH sensitive glass ISE is $59.6\,\mathrm{mV/pH}$. Note, ϕ_{meas} is the measured quantity and contains all boundary potentials of the electrodes and the sensing layer. However, we will find in Section 1.1.4, that only the interfacial potential difference ϕ_i between the sensing layer and analyte solution depends on the target concentration. Therefore $\Delta\phi_{meas} = \Delta\phi_i$ when the concentration changes from c_1 to c_2. It follows that $\Delta\phi_i$ is also governed by the Nernst equation. The derivation of ϕ_i and its connection to the Nernst equation is discussed in the first part of Section 1.1.4.

The internal electrode, usually a Ag/AgCl electrode, is immersed in a solution of its own salt at high concentration. It is not in direct contact with the sensing layer. For the working principle of the ISE, the use of the internal reference solution is unavoidable, although it was identified as a major drawback for making the devices smaller to move towards an integrated sensor array. The internal solution ensures an electrochemically stable interface with the measuring electrode via a well-defined redox reaction needed for the potentiometric measurement[20]. The potential of the internal reference electrode is measured against the external reference electrode. The external reference electrode is also based on the Ag/AgCl or similar reference system and therefore also needs a reference solution. Instead of the sensing layer, the external reference solution is separated by a liquid junction from the analyte solution. The liquid junction ensures electrical connection while minimizing the mixing of the external reference solution with the analyte solution. The potential at the reference electrode is independent of the composition of the analyte solution.

A lot of efforts have been made to replace the two reference electrodes by solid-state contacts to achieve an integrated chemical sensor. While the

---

[1]Throughout this thesis, the notation $\log x = \log(x) = \log_{10}(x)$ is used.
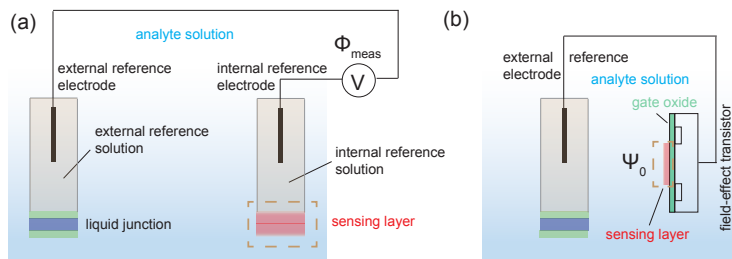
Figure 1.2: Comparison of the classical ion-selective electrode (ISE) and the ion-sensitive field-effect transistor (ISFET). (a) The ISE configuration comprises a reference electrode and the sensing electrode. (b) The ISFET configuration replaces the sensing electrode directly by placing the sensitive layer on top of the FET gate. The external reference electrode comprises a liquid junction which ensures electrical contact with the analyte solution while preventing mixing with the external reference solution.

integration of the external reference electrode is still a big challenge, the integration of the inner reference electrode has led to various successful approaches including the ion-sensitive field-effect transistor (ISFET). During the rise of silicon (Si) microtechnology, the development of metal oxide field-effect transistors (MOSFETs) has led to further insight in the interfaces between oxides, metals and semiconductors. Especially the Si/SiO_2 interface was heavily studied. It is therefore not surprising that an alternative approach based on Si has been proposed by Piet Bergveld in the 1970's[2]. In order to replace the inner solution, the use of a field-effect transistor (FET) was suggested as shown in Figure 1.2b. Originally, the ISFET concept was also believed to abandon the need of the external reference electrode[2]. However, this assumption has been proven wrong and it is now accepted that the external reference electrode is unavoidable[21,22]. Therefore, the integration of ISFET sensors is still limited by the relatively large reference electrode.

It is commonly assumed that adsorbed species within or at the sensitive layer lead to a redistribution of ions in the liquid resulting in a potential drop Ψ_0, called the surface potential. As we will show in Section 1.1.4, Ψ_0 depends on the concentration of the targeted species in the analyte in a very similar way as ϕ_i for the ISE. Correspondingly, the ISFET also obeys the Nernst equation and shares this fundamental limit with the ISE. By comparing the structure of the ISE and ISFET qualitatively, one major difference

becomes apparent: Whereas the sensing layer is placed symmetrically between the analyte solution and the internal reference solution in the case of the ISE, this symmetry is broken for the ISFET where the solid phase of the semiconductor or oxide is in direct contact with the sensing layer (Figure 1.2a and 1.2b). It has been suggested that the lack of symmetry might lead to long-term drift [23–25]. Interestingly, the historical close relationship of ISEs with ISFETs is not apparent in the models used to describe the devices. The ISEs have traditionally been studied by electrochemists who consider charge adsorption in thick, ion-selective membranes [26]. Also in the case of pH sensitive glass electrodes where the sensitive layer is a thick layer of glass, charge adsorption is assumed to occur within the so-called hydration layer. On the contrary, the models explaining the response of ISFET devices consider charge adsorption at the sensor surface solely. We will address this point more in detail in Section 1.1.4.

From Figure 1.2b, we also gather that the ISFET is based on a standard metal oxide semiconductor FET where the polysilicon gate is replaced by the electrolyte, gated via the reference electrode. The following part gives a general introduction to the working principle of FETs and ISFETs.

1.1.3 From Transistors to Ion-Sensitive Devices

Electronic Working Principle: The Field-Effect Transistor

The FET is a three terminal device where the conductance of the Si channel between the source and drain contact is modulated using the gate contact. In a standard metal oxide field-effect transistor (MOSFET), the metal gate electrode is separated from the Si channel by a thin oxide layer, usually SiO_2. A subclass of MOSFETs is based on silicon on insulator (SOI) wafers, where an additional insulating layer of SiO_2 is isolating the device layer from the bulk substrate, shown in Figure 1.3a. Clean silicon is characterized by a relatively small number of charge carriers equally distributed among electrons and holes. Introduction of doping atoms (e.g. boron for p-doping or phosphorus for n-doping) allows adjusting the number of charge carriers in a controlled way, making the device suitable for a specific application. Here we focus on a low-doped p-type SOI MOSFET with highly p-doped source and drain contacts similar to the devices investigated in this thesis (see Section 1.2). The high doping ensures good ohmic contact to the silicon channel which results in a low contact resistance. Furthermore, the doping suppresses the inversion regime of the transistor which is therefore not discussed in this thesis. As a consequence, the p-doped transistor does

only work in accumulation mode where the charge carriers are the holes
of the Si channel. If a voltage V_{sd} is applied between source and drain
contact, a source-drain current I_{sd} will flow in the transistor channel. The
source-drain current normalized by the bias voltage yields the conductance
$G = I_{sd}/V_{sd}$. Importantly, the conductance of the channel is controlled by
the gate voltage V_g applied to the gate contact. A qualitative sketch of the
resulting transfer curve is depicted in Figure 1.3b. A decreasing gate voltage
accumulates holes in the semiconductor channel and increases the current
until saturation occurs due to the finite contact resistance of the device.
For a large range of gate voltages, I_{sd} increases linearly with V_g which is
therefore called the linear regime of the transistor. The transconductance
g_m, defined as $g_m = \partial I_{sd}/\partial V_g$ is constant in the linear regime. Note that
this definition of the g_m, although often used in literature, depends on
the source-drain voltage V_{sd}. Therefore its value is meaningless, until V_{sd} is
given. This is taken into account by using the normalized transconductance
$g_m^* = dG/dV_g = dI_{sd}/dV_g \cdot 1/V_{sd}$. However, if not stated differently, the
source-drain voltage is kept constant at $V_{sd} = 100\,\text{mV}$.

Increasing the gate voltage decreases I_{sd} until at the so-called threshold
voltage V_{th} the current drops approximately to zero. In a first approxi-
mation, the gate voltage allows turning the transistor on ($V_g \ll V_{th}$) and
off ($V_g \geq V_{th}$, $I_{sd} = 0$). This simple approximation is only justified for
small source-drain voltage $V_{sd} \ll V_g - V_{th}$. In the accumulation regime, the
current I_{sd} through the channel can be approximated as [27]

$$I_{sd} = \mu C_{ox}^{\square} \frac{W}{L}(V_g - V_{th})V_{sd} \tag{1.2}$$

with μ the charge carrier mobility, $C_{ox}^{\square}$ the gate oxide capacitance per unit
area and W and L the width and length of the channel. Throughout this
thesis, the symbol $^{\square}$ means per unit area and is used to explicitly differ
between the absolute and the area normalized capacitance. The threshold
voltage is given by [27]

$$V_{th} = \phi_{ms} - \frac{Q_{ox}}{C_{ox}} \tag{1.3}$$

with $\phi_{ms} = \phi_m - \phi_s$ the work function difference between the metal gate
(ϕ_m) and the semiconductor ϕ_s. The second term includes the potential
contribution from all charges of the oxide Q_{ox}. Note that for a transistor
operated in accumulation the threshold voltage corresponds to the flat-band
condition where the band bending is equalized by applying the flat-band
voltage V_{fb} at the gate. Of course, the simple picture assuming $I_{sd} = 0$
for $V_g \geq V_{th}$ is not very accurate. In the subthreshold regime, the current

actually depends exponentially on the gate voltage due to thermally activated charge carriers. The number of charge carriers follows a Boltzmann distribution

$$n_a = n_i e^{-\frac{eV_g}{kT}} \tag{1.4}$$

with n_i the intrinsic carrier concentration, k the Boltzmann constant and T the temperature. The exponential dependence of the current on the gate voltage is characterized by a straight line on the log scale of Figure 1.3b. The subthreshold swing S which determines the ratio of the on- and offset currents is defined as the reciprocal slope of the line in the subthreshold regime:

$$S = \frac{\partial V_g}{\partial (\log I_{sd})} = -2.3 \frac{kT}{e} \cdot n. \tag{1.5}$$

The subthreshold factor n is defined as

$$n = 1 + \frac{C_d}{C_{ox}} \tag{1.6}$$

with C_d the depletion capacitance and C_{ox} the oxide capacitance. n is always greater than 1 and describes the discrepancy between the actual and the ideal device. For an ideal device, $n = 1$ and $S = 59.6\,\mathrm{mV/dec}$ at room temperature.

The ISFET

Figure 1.3c shows the schematic of the ISFET where the metal or polysilicon gate is replaced with a reference electrode immersed in the analyte solution. Additionally, the top part of the transistor surface is covered by a sensing layer. Note that for pH sensing, the sensing layer is directly part of the gate oxide due to the well-known pH sensitivity of oxide materials. Therefore pH sensing is the simplest application for this device. The ISFET threshold voltage receives an additional term Ψ_0 which depends on the chemical composition of the electrolyte [20,22]

$$V_{th} = \phi_{ref} - \phi_s - \Psi_0 - \frac{Q_{ox}}{C_{ox}} \tag{1.7}$$

where ϕ_{ref} is the constant reference electrode potential. Ψ_0 is the potential drop in the electrolyte solution. Ideally, Ψ_0 is the only term varying upon changes in the electrolyte composition. For pH sensing, Ψ_0 is the only pH sensitive quantity. From Equation 1.7 it follows that $\Delta \Psi_0 = -\Delta V_{th}$. The remaining question to understand the working principle of the ISFET device is how Ψ_0 is related to pH. This is discussed next.
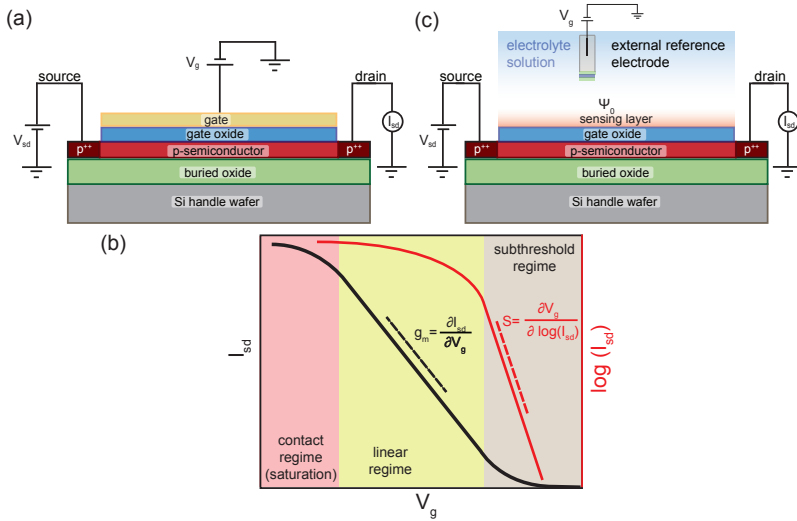
Figure 1.3: (a) Sketch of a p-type SOI MOSFET with highly p-doped contacts. (b) Sketch of the transfer curve of a p-type FET. Source-drain current I_{sd} (black curve, left axis) and $\log I_{sd}$ (red curve, right axis) versus gate voltage V_g. The high p-doping of the contacts suppresses the inversion regime for increasing gate voltages. (c) Sketch of the corresponding ISFET configuration with the gate oxide plus sensitive layer in direct contact with the electrolyte. The metal gate is replaced by an external reference electrode.

1.1.4 The Sensing Interface and its Models

Interestingly, the established models originating from the ion-selective electrodes are usually not applied to its integrated counterpart. For example, the pH response of the glass membrane is explained by a hydration layer within which charge is adsorbed. At the core of this model lies the assumption that all interfaces including the electrolyte/membrane interface are non-polarized. A detailed discussion of the concept of non-polarized and polarized interfaces is beyond the scope of this thesis and the interested reader is referred to the literature [20,28]. Here, we will characterize a non-polarized interface by the fact that one or more species is/are allowed crossing the interface [26]. This leads to a constant electrochemical potential through the interface in the thermodynamic equilibrium. Therefore, the interfacial potential difference ϕ_i can be calculated from simple thermodynamic considerations as carried out in the following paragraph. This characteristic of the interface is represented by an interfacial resistance R_{inter} in the equivalent circuit of Figure 1.4a. Therefore, the interface is also called resistive [29].

In contrast, the site-binding model explains the ISFET pH response as a purely capacitive effect meaning that the interface is ideally polarized [30]. An ideally polarized interface does not allow charge transfer through the interface. In the equivalent circuit diagram shown in Figure 1.4b, this is expressed by an interfacial capacitance C_{dl}. To better understand the boundary conditions of the site-binding model, a short analysis of the hydration model is useful.
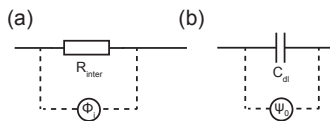

Figure 1.4: Equivalent circuit diagram of (a) a non-polarized interface and (b) an ideally polarized interface.

Non-Polarized Interfaces: Hydration Layer Model

Figure 1.5 shows the classical ISE configuration where the membrane is placed symmetrically between the analyte solution and the internal solution. In the case of a pH sensitive glass electrode, the membrane is a layer

of conductive SiO_2 (doped with Na^+ or Li^+) forming a permeable hydration layer for hydrogen ions. For other ion-selective ISEs, the membrane is often an organic phase permeable for only the targeted species thereby ensuring selectivity. In the following, all interfaces are assumed to be nonpolarized. The measured potential difference ϕ_{meas} between the external reference electrode placed in the analyte solution and the internal reference electrode includes all boundary potentials of the structure. However, we assume that all potentials at the reference electrodes are independent of the solution composition. Under this assumption, the difference in the electrostatic potential in the analyte solution ($\phi(sol)$) and the internal reference solution ($\phi(ref)$) is the quantity of interest ($\phi_{meas} = \phi_M + const$):

$$\phi_M = \phi(sol) - \phi(ref). \tag{1.8}$$

ϕ_M is called the membrane potential in the following and is commonly separated into three different contributions

$$\phi_M = \phi_i + \phi_{inner} + \phi_{dif}. \tag{1.9}$$

ϕ_i is the interfacial potential difference at the membrane/analyte solution interface, ϕ_{inner} the interfacial potential at the membrane/internal (reference) solution interface and ϕ_{dif} the diffusion potential within the membrane as indicated in Figure 1.5. Since the composition of the inner solution is fixed, ϕ_{inner} is assumed to be constant. The diffusion potential may become significant in presence of high ionic gradients within the membrane. Under most conditions, ϕ_{dif} can be neglected and the membrane potential is simply given by ϕ_i and a constant offset:

$$\phi_M = \phi_i + const. \tag{1.10}$$
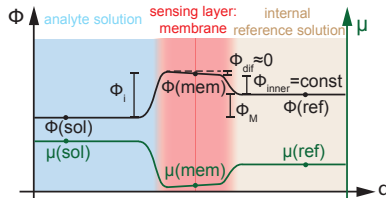

Figure 1.5: Electrostatic potential ϕ (black, left axis) and chemical potential μ (green, right axis) versus distance d through the ISE structure with the analyte solution separated from the internal solution by the membrane. Ideally, $\phi_{dif} = 0$, $\phi_{inner} = const$ and only ϕ_i depends on the analyte composition.

The phase boundary potential ϕ_i is the only quantity which depends on the analyte composition leading to the desired sensitivity to ions. Since $\phi_i = \phi(mem) - \phi(sol)$, only the analyte solution/membrane interface has to be considered. Because this interface is assumed to be non-polarized, we use the fact that the electrochemical potential is constant through the interface:

$$\bar{\mu}(sol) = \bar{\mu}(mem) \qquad (1.11)$$

with $\bar{\mu}(sol)$ and $\bar{\mu}(mem)$ the electrochemical potential in the analyte solution and membrane respectively. In fact Equation 1.11 is valid for every species crossing the interface. However, we assume in the following that only one species can enter the membrane and change ϕ_i. For the formulation of the electrochemical potential, we will use the chemical activity a instead of the concentration c. The chemical activity is a thermodynamic quantity of the effective concentration of a species and defines the chemical potential. a is a dimensionless quantity by definition and depends on the standard state of the species. For ideal solutions, the standard state is given by $c_0 = 1\,\mathrm{M}$ (mol/l) and correspondingly $a = c/c_0$. In a more realistic picture describing non-ideal solutions, the activity deviates from the linear dependence on the concentration due to interactions between the species of the solution and more complex models are needed to describe the activity accurately. For ionic solutions, the Debye-Hückel approximation might be considered [28]. However, if not stated differently, we will always assume ideal solutions. In this thesis, the activity will be used whenever theoretical models are discussed. However, the concentration is the actual experimental parameter. Therefore, the distinction between activity and concentration is not always strictly made because the unit M (mol/l) is usually still added to the activity. This simplifies reading figures with both theoretical fits and experimental data because the concentration range is directly evident.

Assuming an ideal solution, the electrochemical potential $\bar{\mu}$ of species I in the analyte is given by

$$\bar{\mu}(sol) = \mu(sol) + ze\phi(sol) = \mu^0(sol) + 2.3kT\log a^I(sol) + ze\phi(sol) \quad (1.12)$$

and correspondingly in the membrane

$$\bar{\mu}(mem) = \mu(mem) + ze\phi(mem) = \mu^0(mem) + 2.3kT\log a^I(mem) + ze\phi(mem)$$
$$(1.13)$$

with μ the chemical potential, μ^0 the chemical potential under standard conditions, z the valency of ion I and a^I the activity of the uncomplexed ion I. ϕ is the electrical potential, k the Boltzmann constant, T the absolute

temperature and e the electric charge. Inserting Equations 1.12 and 1.13 into Equation 1.11 leads to

$$\phi_i = \phi(mem) - \phi(sol) = \frac{\mu^0(sol) - \mu^0(mem)}{ze} + \frac{2.3kT}{ze}\log\frac{a^I(sol)}{a^I(mem)}. \quad (1.14)$$

An ideal membrane is designed in such a way that the activity of the uncomplexed ion within the membrane $a^I(mem) = const$ and does not change upon a change in the concentration of ion I of the analyte solution. The requirements to achieve such a membrane are discussed qualitatively in [26]. Assuming $a^I(mem) = const$, the interfacial potential depends logarithmically on the activity of the targeted ion in the analyte solution: $\phi_i \propto \log a^I(sol)$. Measuring the change of the interfacial potential $\Delta\phi_i = \phi_i(a_2^I(sol)) - \phi_i(a_1^I(sol))$ upon changing the activity from a_1^I to a_2^I yields

$$\begin{aligned}
\Delta\phi_i = \Delta\phi_{meas} &= \phi_i(a_2^I(sol)) - \phi_i(a_1^I(sol)) \\
&= \frac{2.3kT}{ze}\log\frac{a_2^I(sol)}{a^I(mem)} - \frac{2.3kT}{ze}\log\frac{a_1^I(sol)}{a^I(mem)} \quad (1.15) \\
&= \frac{2.3kT}{ze}\log\frac{a_2^I(sol)}{a_1^I(sol)}
\end{aligned}$$

which is the Nernst equation as introduced in Equation 1.1.[1]

To achieve selectivity to a specific ion, ionophores complexing the targeted ion must be incorporated into the membrane. Thanks to countless studies on membrane materials, today's ISEs display Nernstian behavior over a large concentration for various ions. However, the application of ISEs for biosensing is not straight-forward. The difficulty lies in designing a membrane where the targeted, large biomolecules dominate the establishment of the membrane potential[20]. Therefore, most protein detection measurements presented for ISEs are based on the indirect detection via a well-established ion[31–33].

Ideally Polarized Interfaces: The Site-Binding Model

The first gate material applied to ISFET devices was SiO_2, where a sub-Nernstian response was found[2,22]. Soon after, Nernstian pH responses were

---

[1]Note that the Nernst equation presented by Equation 1.15 is given in terms of activities, the Nernst equation introduced by Equation 1.1 in terms of concentration. However, $\log\frac{a_2}{a_1} = \log\frac{c_2/c_0}{c_1/c_0} = \log\frac{c_2}{c_1}$.

presented with gate materials like silicon nitride (SiN) and aluminum oxide (Al_2O_3)[20]. Since these materials are not expected to form a substantial hydration layer, the origin of their pH sensitivity was debated again. The site-binding model proposed by Yates et al.[34] allows describing the pH sensitivity as charging of a double layer capacitance due to the chemical reactions of surface hydroxyl groups with protons of the solution. The model is now widely used to describe the ISFET pH response.

In short, the site-binding model assumes that the surface hydroxyl groups (MOH for a metal (M) oxide) are amphoteric with the following equilibrations:

$$\begin{aligned} MOH \rightleftharpoons MO^- + H^+, \ K_a &= \frac{\nu_{MO^-} \cdot a_{H_s^+}}{\nu_{MOH}} \\ MOH_2^+ \rightleftharpoons MOH + H^+, \ K_b &= \frac{\nu_{MOH} \cdot a_{H_s^+}}{\nu_{MOH_2^+}} \end{aligned} \tag{1.16}$$
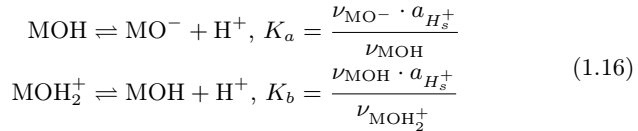
with $a_{H_s^+}$ the activity of protons at the oxide/electrolyte interface and ν the number of sites per unit area (m^{-2}) of a particular surface group. K_a, K_b are the acid and base dissociation constants. Alternatively, the dissociation constants are expressed in their logarithmic presentation: $pK_a = \log K_a$ and $pK_b = \log K_b$. The activity of protons at the surface $a_{H_s^+}$ can be related to the corresponding bulk activity $a_{H_b^+}$ assuming a Boltzmann distribution

$$a_{H_s^+} = a_{H_b^+} e^{-\frac{e\Psi_0}{kT}} \tag{1.17}$$

where Ψ_0 is the potential drop from the surface to the bulk solution as shown in Figure 1.6a. We refer to this quantity as the surface potential.

Without presenting the proof in this thesis, it follows from these equations that a Nernstian response for Ψ_0 versus pH is obtained if the ratio $\nu_{MOH_2^+}/\nu_{MO^-}$ at the surface remains constant. In other words, according to the Boltzmann equation, a change of bulk $pH_b = -\log a_{H_b^+}$ can be compensated either by a change of the surface $pH_s = -\log a_{H_s^+}$ or surface potential Ψ_0. For a surface with a constant ratio $\nu_{MOH_2^+}/\nu_{MO^-}$ the surface pH is buffered leading to a constant $a_{H_s^+}$. Correspondingly, the surface potential responses in a Nernstian manner when changing the proton activity from $a_{H_b^+,1}$ to $a_{H_b^+,2}$: $\Delta\Psi_0 = 2.3kT/e \log(a_{2,H_b^+}/a_{1,H_b^+}) = 2.3kT/e\Delta pH_b$. To obtain an analytical relation between Ψ_0 and the bulk pH we need to relate the charge per unit area at the oxide surface σ_0 to Ψ_0. For this we first assume that the total number of surface hydroxyl groups per unit area N_s is a constant:

$$N_s = \nu_{MOH} + \nu_{MOH_2^+} + \nu_{MO^-}. \tag{1.18}$$

The described reactions build up a surface charge (per unit area) σ_0 at the oxide/electrolyte interface which is given by the sum of all charged groups:

$$\sigma_0 = e(\nu_{\text{MOH}_2^+} - \nu_{\text{MO}-}). \tag{1.19}$$

The point of zero charge (PZC) is characterized by the condition $\sigma_0 = 0$ fulfilled for $pH = (\text{p}K_a + \text{p}K_b)/2$. The wanted expression connecting Ψ_0 with σ_0 follows from the double layer theory which assumes a purely capacitive interface. Figure 1.6a shows a drawing of the oxide/electrolyte interface for a positive σ_0. To maintain charge neutrality, a layer of counter ions (An$^-$) builds up at some small distance from the interface, which is called the Stern layer. A single layer of counter ions can not sufficiently screen the surface charges and a diffuse layer extends until the electrostatic potential approaches its value Ψ_{bulk} in the bulk of the electrolyte. The total charge in the electrolyte is σ_d. The layers can be modeled as two capacitances C_{Stern} and C_{dif} in series. In this structure, the relation between Ψ_0 and σ_d follows from solving the Poisson-Boltzmann equation [35]:

$$-\Psi_0 = \frac{2kT}{e}\sinh^{-1}\left(\frac{\sigma_d}{\sqrt{8kTc\epsilon}}\right) + \frac{\sigma_d}{C_{Stern}^{\square}}. \tag{1.20}$$

c is the ion concentration of the solution and ϵ the dielectric constant of the solvent. $C_{Stern}^{\square}$ is the Stern capacitance per unit area. The first term denotes the contribution of the diffuse layer and the second term the contribution of the Stern layer. For medium and higher electrolyte concentrations, the potential drops mainly over the Stern capacitance. In this regime, $\sinh^{-1}$ can be linearized which allows defining the double layer capacitance C_{dl} or $C_{dl}^{\square}$ as

$$-\Psi_0 = \frac{\sigma_d}{C_{dl}^{\square}} = \sigma_d \cdot 2\frac{kT}{e}\sqrt{8\epsilon kTc} + \frac{\sigma_d}{C_{Stern}^{\square}}. \tag{1.21}$$

In principle, the charge on the insulator σ_0 is counterbalanced by the charge in the electrolyte σ_d and charges in the silicon Q_s and all charges inside the insulator Q_{ox}. It can be shown that Q_s and Q_{ox} contribute both negligibly to the charge balance [20]. Therefore, the value of σ_0 is only defined by the chemistry at the oxide/electrolyte interface. Using $\sigma_0 = -\sigma_d$ we can finally write

$$\sigma_0 = \Psi_0 C_{dl}^{\square}. \tag{1.22}$$

This leads to the following relation between the bulk pH and the surface

potential Ψ_0:

$$a_{\mathrm{H}_{\mathrm{b}}^+} = \sqrt{K_a K_b} \exp\left(\frac{e\Psi_0}{kT}\right) \times \tag{1.23}$$

$$\frac{\frac{e\Psi_0}{kT}\frac{C_{\mathrm{dl}}^{\square}}{C_{\mathrm{s}}^{\square}}\frac{1}{2}\sqrt{\frac{K_b}{K_a}} + \sqrt{1 + \left(\frac{e\Psi_0}{kT}\frac{C_{\mathrm{dl}}^{\square}}{C_{\mathrm{s}}^{\square}}\frac{1}{2}\sqrt{\frac{K_b}{K_a}}\right)^2\left(1 - \left(2\sqrt{\frac{K_a}{K_b}}\right)^2\right)}}{1 - \frac{e\Psi_0}{kT}\frac{C_{\mathrm{dl}}^{\square}}{C_{\mathrm{s}}^{\square}}}$$

with $C_s^{\square}$ the surface buffer capacitance defined as

$$C_s^{\square} = \frac{e^2 N_s}{2.3kT}. \tag{1.24}$$

A high buffer capacitance, hence a large N_s is needed to obtain a Nernstian response, as we will see in Section 1.2.4 and 1.2.5.
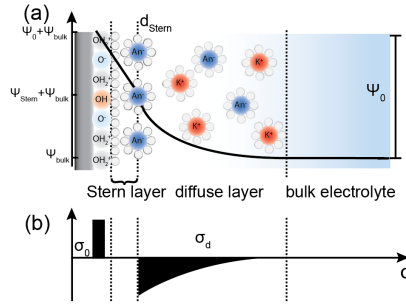
Figure 1.6: (a) Potential distribution at the oxide/electrolyte interface. The surface potential Ψ_0 denotes the potential difference between the solid surface and the bulk electrolyte solution. (b) Charge distribution at the oxide/electrolyte interface. σ_0 is the charge at the sensor surface, determined by the interface chemistry. σ_d is the total charge in the solution, screening the electric field due to σ_0.

The Limits of the Site-Binding Model

Ever since Siu et al.[36] and Bousse et al.[37,38] applied the site-binding model to explain the ISFET pH response, criticism was raised against the assumption of a purely capacitive interface (ideally polarized)[20,23,39]. It is often stated that ideally polarized interfaces - as the name implies - do not exist in

reality. This discussion leads to the question whether protons get adsorbed at the sensor surface or within the hydration layer. For SiO_2 gate dielectrics, slow hydration might occur, depending on the material quality [40]. Reports of alkali ion diffusion into the material (e.g. Na^+) support the hydration argument [41]. However, in the case of high-k oxide layers such as Al_2O_3 or HfO_2 this situation is different. These materials are excellent barriers against ionic diffusion and show negligible hydration [20]. As pointed out by Sandifer the site-binding model can be treated as limiting case of the hydration layer for an extremely small thickness of the hydration layer [30]. Figure 1.7 illustrates the qualitative comparison of the hydration layer model with the site-binding model. The thickness of the hydration layer shown in Figure 1.7a can be regarded as effectively increasing the number of sites (in the site-binding model called N_s) while making the transition from surface to volume. Therefore, even materials with a relatively low number of surface hydroxyl groups could lead to a Nernstian response if they hydrate enough to compensate the low surface density with a considerable hydration thickness d [30]. In conclusion, a detailed description of the interface could be based on a combination of the two models and might depend also on the device geometry, besides the material properties. However, for understanding the sensor response of ISFETs studied in this thesis, the site-binding model has been proven very useful. As a key advantage, the site-binding model provides a precise microscopic picture of the underlying processes and allows describing the measured responses quantitatively.

Before discussing the prediction of the site-binding model in more detail in Section 1.3.2, we introduce the ISFET platform based on silicon nanowires studied in this thesis in Section 1.2. The Nernstian response of the devices for Al_2O_3 and HfO_2 gate dielectrics is demonstrated in Section 1.2.4, in agreement with the site-binding model for large N_s. The model is further validated by pH measurements of devices with a reduced N_s as presented in Section 1.2.5.

1.1.5 The Concept of ISFETs Applied to the Nanoscale

In 2001, the ISFET concept experienced a revival at the nanoscale. Cui et al. proposed the use of arrays of highly integrated Si nanowires (SiNWs) operated as ISFETs [3]. Using a microfluidic system, single wires of the array can be functionalized individually to become specific to a certain analyte. As a result, a multifunctional platform is achieved. Using nanoscale ISFETs in combination with a microfluidic system, the sample volume was reduced
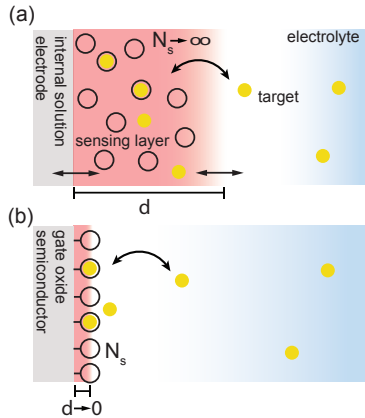
Figure 1.7: Schematic comparison of the hydration model (a) with the site-binding model (b). Considerable hydration might lead to a large effective N_s compared to the N_s originating from the surface solely.

to the microliter and nanoliter range [42,43]. The choice of SiNWs is not only motivated by the possibility of high integration. As a key aspect, SiNWs are expected to have superior sensing properties such as charge sensitivity and low detection limits due to the high surface-to-volume ratio [3,8,44–46]. The SiNWs studied in this thesis were also used to study the impact of the nanowire geometry on the sensing properties in terms of the response [47] and noise [48] in the beginning of this PhD project. For further details the reader is referred to the PhD thesis of K. Bedner [49] and M. Wipf [7]. The essentials of these studies will be repeated in this chapter for reasons of completeness. The width dependence of the pH response is briefly discussed in Section 1.2.4. The scaling of the noise with NW area is discussed in Section 1.3.3 theoretically and experimentally in Section 3.2.

1.2 Methods and Characterization

In this thesis, we focus on ISFETs based on SiNWs fabricated using a top-down approach on silicon on insulator (SOI) wafers [47]. Before my PhD project, a process based on UV lithography was developed at the *University of Basel* to fabricate the NW arrays. This process is described in detail in the PhD thesis of O. Knopfmacher [50]. The process was then adapted to

an electron-beam (e-beam) lithography based process at the *Paul Scherrer Institute (PSI, Villigen)* by K. Bedner. Details on the fabrication process can be found in a previous work[47], in the PhD thesis of K. Bedner[49] and Appendix A.

1.2.1 Device Layout

Figure 1.8 shows the device layout. It consists of 48 NWs arranged in four spatially separated arrays. All 12 NWs of each array share a common bus line for the drain contact. The design of the arrays allows using different functionalizations on a single device leading to a multifunctional platform as described in Chapter 2. All NWs share a common length of $6\,\mu$m. In an early design, the NWs on a single chip had 8 different widths between $100\,$nm and $1\,\mu$m. This design was used to study the influence of the NW dimensions on the sensing properties[47,48]. As we will see in Section 1.3.3, the signal-to-noise ratio increases with $\sqrt{\text{area}}$ of the device. Therefore, the latest design consists of NWs of only two different widths of $1\,\mu$m and $25\,\mu$m. Independent of the exact channel dimensions, the term nanowire is used for all devices studied in this thesis.

1.2.2 Device Fabrication and Liquid Handling

Device Fabrication

The samples were fabricated by a top-down approach on silicon on insulator (SOI) wafers (*Soitec*, France) with a buried oxide (BOX) layer of $145\,$nm thickness. The $85\,$nm thick p-Si(100) device layer with resistivity of $8.5 - 11.5\,\Omega$cm was first covered with a thermal oxide of $15\,$nm thick SiO_2. The NW pattern was defined with e-beam lithography. The structures were transferred to the wafer by dry etching of the SiO_2 and anisotropic wet etching of the Si device layer with tetramethylammonium hydroxide (TMAH and isopropyl alcohol 9:1 at $45\,^\circ$C). The resulting NWs with Si (111) side faces have a height of $80\,$nm, a width ranging from $100\,$nm to $25\,\mu$m and a common length of $6\,\mu$m. Ohmic contacts at the source and drain contacts were achieved by ion implantation. The corresponding areas were heavily doped by BF_2^+ ions (energy $= 33\,$keV, dose $2.3 \times 10^{15}\,$cm^{-2}), followed by a thermal annealing step in a forming gas ($6\,$min at $950\,^\circ$C) to activate the dopants. To operate the device in liquid, a thin protection layer of $20\,$nm Al_2O_3 or HfO_2 ($20\,$nm or $8\,$nm) was deposited using atomic layer deposition
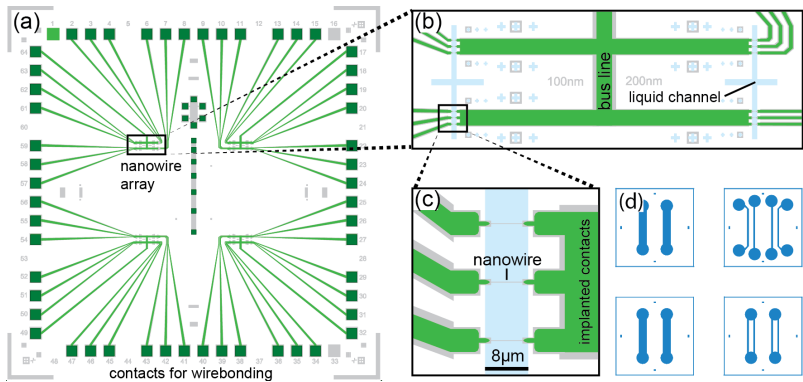
Figure 1.8: (a) Sample layout. Each chip comprises 48 individually addressable NWs arranged in four spatially separated arrays. Each array has a common bus line. Grey areas are the lithography design for the silicon, bright green for the ion implantation and dark green for contact metallization.(b) Close up of the upper left array comprising NWs with width of $100\,\text{nm}$ (left) and $200\,\text{nm}$ (right). Blue areas are the lithography design for openings in the SU-8 layer defining the liquid channel. (c) Close up of a pixel with three NWs. All NWs have the same length of $6\,\mu\text{m}$. (d) Lithography layout of the different PDMS microchannel molds. The round areas at both channel ends denote the in- and outlets. Figure adapted from [7].

(ALD) at $225\,°C$ (*Savannah S100, Cambridge NanoTech*). Opening of the contact pads with buffered hydrochloric acid allowed completing the NW contact by metallizing the contacts with Al-Si(1%) and annealing at $450\,°C$. The good quality of the ALD oxide ensures low hysteresis and low leakage currents ($I_{leak} < 0.1\,\text{nA}$). In addition, Al_2O_3 as well as HfO_2 surfaces are known to possess a high ($N_s = 1 \cdot 10^{19}\,\text{m}^{-2}$) number of hydroxyl groups leading to a Nernstian response of $59.6\,\text{mV/pH}$ towards changes in proton concentration[47,51]. This feature makes Al_2O_3 and HfO_2 ideal candidates for pH sensing. To minimize leakage currents, the sample was covered by an additional protection layer (*SU-8 2002, MicroChem*) with a thickness of $2\,\mu$m. Optical lithography was used to define openings in the SU-8 layer. Figure 1.9 shows various pictures of the sensor device and silicon NWs. The chip is wire bonded into a chip carrier shown in Figure 1.9e. To protect the
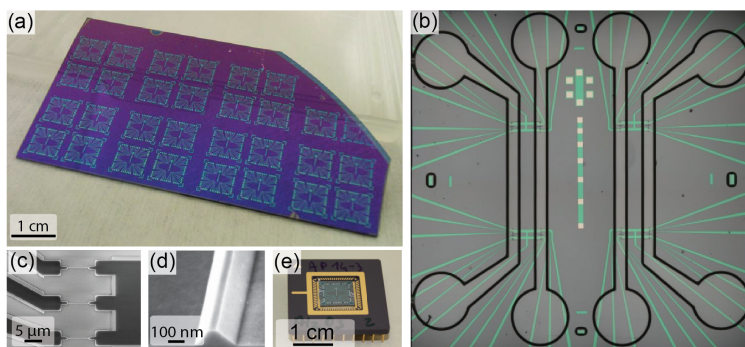
Figure 1.9: (a) Optical picture of a wafer part after lithography. Each square structure results in a sample of 48 NWs. (b) Optical picture of a sample covered with a 4 channel PDMS microfluidic cell. (c) SEM graph of a pixel with three 200 nm-wide wires. Dark areas are ion implanted. (d) SEM graph of the cross section of a $100\,\text{nm}$-wide NW. (e) Optical picture of a sample after wire-bonding. Images by K. Bedner.

electrical contacts when measuring in liquid, the bonds were finally sealed with epoxy (Epotek 353ND), shown in Figure 1.10a.

Liquid Handling

One practical aspect of ISFET sensing is the fluidic system. Ideally, it minimizes analyte consumption and time needed for exchanging the solutions. Easy de- and attachment expands the possibilities of surface functionaliza-

tions and increases the flexibility of the sensor. The liquid cell must ensure stable gating of the transistors via the external reference electrode. To meet these requirements, different fluidic systems have been designed during this PhD project. The latest development is based on a two-step polydimethyl-siloxan (PDMS) microfluidic cell. The channels were defined in $100\,\mu$m thick SU-8 (*SU-8 100 MicroChem*) Si masters by e-beam lithography. The microchannels resulted by pouring PDMS (*SYLGARD 184 Silicone Elastomer*) onto the masters and curing at $60\,^\circ$C for 2 h. Then, the PDMS was peeled off and pierced to insert the Teflon (polytetrafluorethylen, PTFE) tubes as shown in Figure 1.10b. To achieve good mechanical stability and to avoid leakage, the PDMS microchannel was further grouted into a second layer of PDMS as shown in Figure 1.10c.

A flow-through Ag/AgCl reference electrode (16-702, *Microelectrodes, Inc.*) is connected to the microchannel to ensure electrical gating via the electrolyte. An earlier version of the fluidic cell is based on polyetheretherketone (PEEK) shown in Figure 1.11a. A Ag/AgCl reference electrode (MI-401-F, *Microelectrodes, Inc.*) and a platinum wire are included in the cell to control and apply the gate voltage directly on top of the structures. For most measurements, the platinum wire was removed and the liquid-gate voltage was directly applied to the reference electrode. The flow cell is pressed on the sample and sealed by an O-ring.
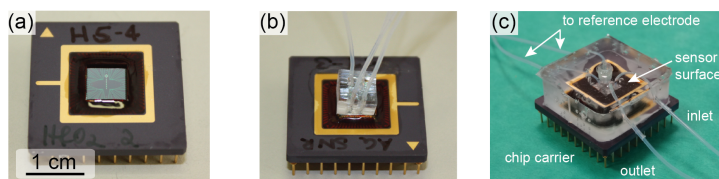
Figure 1.10: (a) Optical picture of a sample wire bonded onto a chip carrier with epoxy protected contacts. (b) Optical picture of a sample covered with a microfluidic channel with inlet and outlet tubings. (c) Final PDMS microfluidic cell for better stability.

The liquid setup is shown in Figure 1.11b. A valve selector system (*CHEMINERT VICI, Valco Instruments Co. Inc.*) was used to switch between different analyte solutions. For exchanging the solutions we used two different approaches. For most measurements presented in this thesis, a peristaltic pump was used to pull the liquid via the microchannel covering the sample through the fluidic system. Alternatively, the liquid was pushed via air pressure through the fluidic system. The latter approach turned

out to be very useful for time resolved measurements, in particular for the protein binding studies presented in Chapter 4.
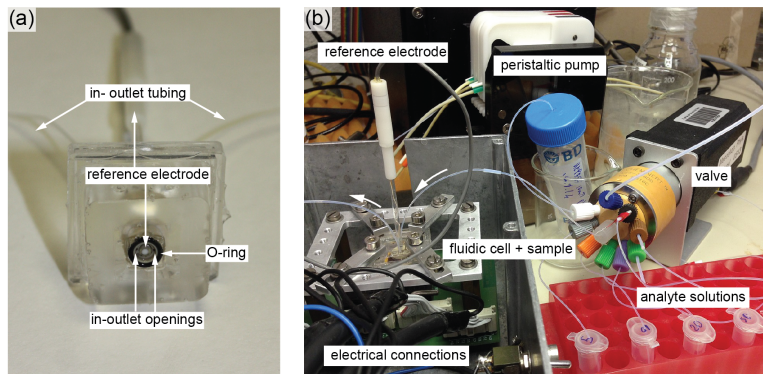
Figure 1.11: (a) Liquid cell with the reference electrode mounted in the middle of the fluidic chamber. (b) Liquid setup. A peristaltic pump is used to pull the analyte solutions through the valve to the liquid cell.

Surface Functionalization

The specific detection of target analytes is an important aspect of this thesis. The ALD oxide of the studied SiNWs intrinsically ensures the detection of protons as we will see in Section 1.2.4. For the specific detection of any other species (ions or biomolecules), the sensor surface needs to be modified. Different methods have been investigated for surface functionalization. Besides polyvinylchloride (PVC) membranes with potassium-selective ionophores incorporated[52], the covalent anchoring of functional molecules to the NW surface was found to be a valuable method. In collaboration with the group of Prof. U. Pieles at *Fachhochschule Nordwestschweiz*, the surface of Al_2O_3-covered SiNWs has been decorated with self-assembled monolayers (SAMs) of silane molecules for various applications[7,51]. For the specific detection of ionic species, we covered the gate dielectrics of SiNWs with a 20 nm gold layer with 5 nm chromium as adhesion layer. Using gold enables different surface chemistry as further discussed in this thesis. In Chapters 2 and 3, SAMs of ion-sensitive molecules for specific sodium, calcium and fluoride detection were obtained in collaboration with the group of Prof. E. C. Constable from the *Department of Chemistry* at the *University of Basel*.

In Chapter 4, FimH proteins are detected in collaboration with the group of Prof. B. Ernst from the *Department of Pharmaceutical Sciences* at the *University of Basel*.
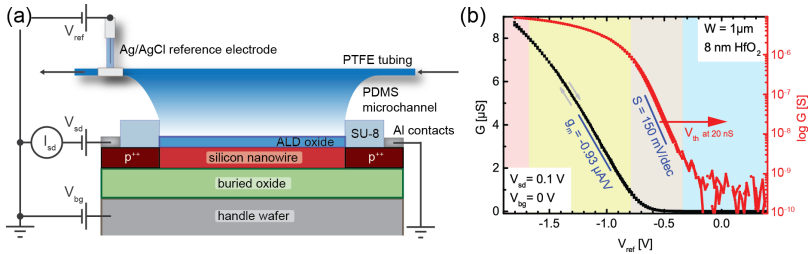
Figure 1.12: (a) Sketch of the measurement setup. A constant source-drain voltage V_{sd} is applied to the nanowire and the source-drain current I_{sd} is measured. A liquid-gate voltage V_{ref} is applied to the reference electrode and the back-gate voltage V_{bg} to the handle wafer. (b) Transfer curve of a $1\,\mu$m-wide SiNW with $8\,$nm HfO$_2$ as gate oxide measured in pH 3 buffer solution. Conductance G on linear scale (black symbols, left axis) and logarithmic scale (red, right axis) versus liquid-gate potential V_{ref}. The different background colors indicate the saturation (or contact regime), the linear, the subthreshold and the leakage (or depletion) regime of the transistor (from left to right). The normalized transconductance is $g_m^* = dG/dV_g = 9.3\,\mu$S/V.

1.2.3 Measurement Setup and Basic Characterization

Figure 1.12a depicts a schematic of the measurement setup. A *Keithley 2636A* source meter with two channels was used to apply the source-drain voltage V_{sd} and to measure the source-drain current I_{sd} through the NWs. To address all 48 NWs of the device, a *Keithley 3706* switching unit was used. The liquid-gate voltage V_{ref} was applied to the reference electrode and the back-gate voltage V_{bg} to the handle wafer. All devices, including the pump and the valve of the fluidic system, were controlled by a LabView program.

Figure 1.12b shows the transfer curve of a $1\,\mu$m-wide SiNW with $8\,$nm HfO$_2$ as gate oxide for $V_{sd} = 0.1\,$V and $V_{bg} = 0\,$V. The transistor is in depletion at high liquid-gate voltages due to the low p-type doping. Leakage currents from the electrolyte to the NW determine the conductance in the depletion regime. The high quality of the ALD gate oxide and the SU-8 protection layer ensure low leakage currents ($I_{leak} < 0.1\,$nA). The inversion regime is suppressed by the p-n junction at the highly p-doped source and

drain contacts. Decreasing V_{ref} to more negative values starts accumulating holes in the nanowire in the subthreshold regime. The subthreshold swing has typical values between 120 and 180 mV/dec. The linear regime is reached by further decreasing the liquid gating and is characterized by a linear dependence of G on V_{ref} and therefore by a constant transconductance g_m. Finally, the saturation or contact regime is reached for even more negative liquid-gate voltages. In the saturation regime, the serial resistance of the contacts starts to dominate, thereby limiting a further increase of the conductance.

The threshold voltage V_{th} is commonly defined as the value of V_{ref} where the transition from the linear to the exponential gate dependence occurs. However, as further explained in Section 1.2.4, we approximate the threshold voltage V_{th} at a constant conductance value, typically $G = 20$ nS. Sweeping the liquid-gate voltage V_{ref} introduces a small hysteresis of the transfer curves, usually < 5 mV. We assume that this value is mainly determined by the charge trap states in the gate oxide. The value of 5 mV is relatively large compared to typical signals given by a few tens of mV. However, the hysteresis can be further reduced by increasing the measurement time and by minimizing the number of trap states at the gate dielectric by an improved fabrication process.

The back-gate voltage influences the threshold voltage and the transconductance and can be used to reach the optimal operation regime. However, at high negative V_{bg} the subthreshold swing increases due to contributions from current at the back interface. Therefore, if not stated differently, $V_{bg} = 0$ V in this thesis. Studies of the back gate dependence were done prior to this PhD work. Further details on the role of the back-gate voltage for the transfer curves and pH response can be found in the PhD thesis of O. Knopfmacher [50] and in reference [4].

Measurement Procedure

Two different measurement procedures were used. A steady-state method was implemented to determine the shift of the surface potential. While sweeping the liquid-gate voltage V_{ref}, the conductance (at $V_{sd} = 100$ mV) of each NW is sequentially measured using the switching unit. This results in a transfer curve (G versus V_{ref}) for each wire which is used to read out V_{th}. Then, the analyte solution is exchanged and the sample is stabilized for a few minutes to reach equilibrium, followed by the next measurement cycle. Alternatively, time-dependent measurements were obtained by applying a

fixed liquid-gate voltage while continuously measuring I_{sd}.

Both procedures will be used in the following. As introduced in Section 1.1.4, most oxides in contact with an electrolyte undergo reactions with protons of the solution. In particular Al_2O_3 and HfO_2 as gate materials of SiNWs have been successfully used for pH sensing[5,47,50]. The pH response of our devices is studied in the following.

1.2.4 pH Sensing

Figure 1.13a shows the transfer curves of an Al_2O_3-coated NW in different pH solutions on a linear scale. The curves shift to the right with increasing pH due to the additional contribution of Ψ_0 to the total gate voltage. For $V_{ref} < 0.5\,\mathrm{V}$, the transistor is in the linear regime and the transconductance g_m is constant. Every transfer curve was measured after a short stabilization period after the exchange of the pH solutions. If the dynamics during the exchange is of interest, time-dependent measurements are needed. Thereby, I_{sd} is constantly measured while exchanging the different analyte solutions. Importantly, the gate has to be fixed to a constant potential ($V_{ref} = const$), ideally within the linear regime of the transistor.

The measured current can be related to the gate by normalizing by the transconductance. This is called the quasi-threshold voltage $V_{th}^* = (I_{sd} - I_0)/g_m$ in this thesis. The offset-current I_0 is a constant frequently used to shift the quasi-threshold voltage of individual SiNWs for the ease of comparison. For time-dependent measurements, the conversion allows relating a change in current from $I_{sd}(t_1)$ to $I_{sd}(t_2)$ directly to a change in surface potential via

$$- \Delta\Psi_0 = \Delta V_{th}^* = \frac{\Delta I_{sd}}{g_m} = \frac{I_{sd}(t_2) - I_{sd}(t_1)}{g_m} \qquad (1.25)$$

for our p-type ISFETs operated in accumulation. V_{th}^* versus time is shown in Figure 1.13b for a fixed liquid-gate voltage of $V_{ref} = 0.4\,\mathrm{V}$. Since the response of a single NW is shown, $I_0 = 0$. V_{th}^* changes approximately by $56\,\mathrm{mV/pH}$, which is close to the Nernstian limit indicated by the dashed horizontal lines. This is expected for a high quality ALD oxide surface with a large N_s. A robust and precise method for quantifying changes of the surface potential is to read out the shift of the transfer curves of the transistor. Figure 1.13c shows the same transfer curves as Figure 1.13a but on a semilog scale. The shift of the curves is best observed in the subthreshold regime. To quantify the shift of the transfer curves, we read
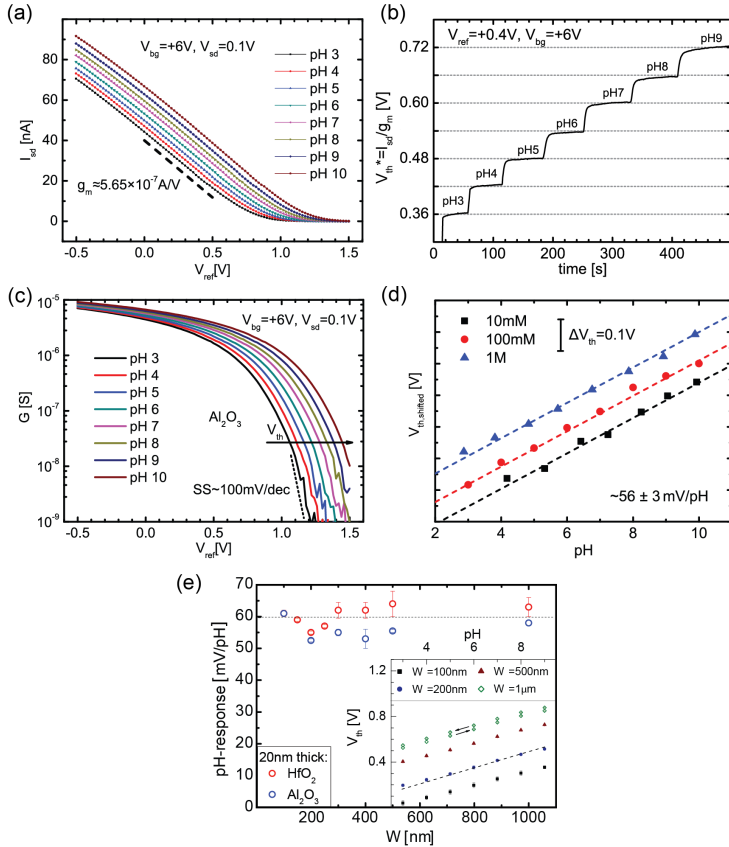
Figure 1.13: (a) Transfer curves for a SiNW with Al_2O_3 as gate oxide measured in different pH solutions. Source-drain current I_{sd} versus liquid-gate potential V_{ref}. The curves shift to the right for increasing pH values. The figure reveals a transconductance independent of the pH value of $g_m \approx 5.65 \cdot 10^{-7}$ S corresponding to $g_m^* = 5.65 \,\mu S/V$. (b) Time resolved pH measurement (V_{th}^* versus time). The measured I_{sd} was converted to V_{th}^* by the transconductance: $V_{th}^* = (I_{sd} - I_0)/g_m$ with $I_0 = 0$. (c) Conductance G versus liquid-gate potential V_{ref} on a semilog scale. The shift of the transfer curves is best observed in the subthreshold. To quantify the shift, we read out the threshold voltage V_{th} as a value of V_{ref} at a constant conductance value of $G = 20$ nS as indicated by the black arrow. (d) Shifted threshold voltage $V_{th,shifted}$ versus pH measured for three different ionic strengths of the electrolyte. (e) pH response of SiNWs with Al_2O_3 and HfO_2 gate dielectrics versus wire width W. An effect of the NW width is not observed. Inset: Threshold voltage V_{th} extracted at $G = 20$ nS versus pH shows the linear response at the Nernst limit over the full pH range. Figures taken from reference[47,53].

out the threshold voltage V_{th} as a value of V_{ref} at a constant conductance value of $G = 20\,\text{nS}$ (indicated by the black arrow). Practically, V_{th} is read out using an automized Matlab (*MathWorks*) script. As for the quasi-threshold voltage V_{th}^*, it holds that

$$- \Delta \Psi_0 = \Delta V_{th}. \qquad (1.26)$$

The threshold voltage is used to determine the response of the ISFET to changes in pH, presented in Figure 1.13d. In the graph, V_{th} has been shifted by a constant offset for the better comparison of the different measurements at ionic strengths of $10\,\text{mM}$, $100\,\text{mM}$ and $1\,\text{M}$. This results in the shifted threshold voltage $V_{th,shifted}$. The pH response is commonly defined as the slope of the V_{th} versus pH characteristics given in mV/pH. The slope ($\approx 56\,\text{mV/pH}$) is close to the Nernstian limit independent of the background ionic strength of the electrolyte.

The influence of the NW width on the pH response has also been studied for SiNWs coated with Al_2O_3 and HfO_2 and widths W ranging from $100\,\text{nm}$ to $1\,\mu\text{m}$ [47]. We find no influence of the wire width on the pH sensing properties. In other words, shrinking the dimensions to the nanoscale does not increase the response to pH for the investigated geometries.

1.2.5 Surface Passivation

In Section 1.1.4, the site-binding model was introduced to explain the pH response of ISFETs. The model predicts a Nernstian response for a large N_s which is experimentally reproduced by the Nernstian response of SiNWs with Al_2O_3 and HfO_2 gate dielectrics. Additionally, the model allows describing the intermediate case for lower N_s. In collaboration with J. Kurz from the group of Prof. U. Pieles at the *Fachhochschule Nordwestschweiz*, we studied the influence of N_s on the pH response [51]. This was realized with self-assembled monolayers (SAMs) of silanes with long alkyl chains (octadecyldimethylmethoxysilane in vapor phase at $80\,°\text{C}$) passivating the SiNW Al_2O_3 surface as depicted in Figure 1.14a. A total passivation time of 7 days was needed to fully suppress the pH response.

Figure 1.14b shows $-V_{th,shifted}$ versus pH for different functionalization times. In the original publication, the sign of the shifted threshold voltage ($-V_{th,shifted}$) was included to directly compare the data with the theoretical surface potential Ψ_0 predicted by the site-binding model. The

model agrees well with the data for the parameters $pK_a = 7.2$, $pK_b = 6.8$, $C_{dl}^{\square} = 0.16 F/m^{-2}$ and N_s as the only fitting parameter. Before functionalization (0 d), a Nernstian response is observed. With increasing functionalization times, the pH response becomes weaker and non-linear due to the saturation at low and high pH. After 7 days of passivation, no pH response is observed anymore. UV/ozone cleaning removes the SAM, restoring the Nernstian response of the Al_2O_3 surface (empty squares in Figure 1.14b). For each pH measurement at a specific passivation time, we approximate the pH response (here denoted as s_{pH}) as the total change in ΔV_{th} divided by the pH range, where the change occurs. s_{pH} (black squares, left axis) versus passivation time is shown in Figure 1.14c. Importantly, the extracted values of N_s (red circles, right axis) versus passivation time are shown in Figure 1.14c.

Reducing N_s by more than 2 orders of magnitudes over 7 days of passivation leads to a pH insensitive SiNW. An insensitive NW could be applied as an on-chip integrated reference electrode, measuring the electrical potential only [22]. A passivated NW could further be useful for the implementation of a selective sensor for a targeted species other than protons. For this task, the sensor needs to be functionalized with additional binding sites, selectively binding the target. Full selectivity is achieved when only the adsorption of the targeted species leads to a change in V_{th} of the NW. Changes in pH of the analyte solution should have no influence on V_{th}, which is possible via the proposed functionalization procedure. However, the passivation of the SiNW oxide surface with SAMs is not trivial and in particular time-consuming. A simple alternative for reducing the number of surface sites is given by an additional coating of the gate dielectric with a material with an intrinsically low N_s. We will use gold for this purpose as discussed in Chapters 2, 3 and 4. The reduction of N_s is a crucial step for specific sensing as further elaborated in Section 1.3.2.

1.3 Sensitivity and Limitations

In the first part of this chapter, the surface potential Ψ_0 was introduced using the site-binding model to explain the pH response of ISFETs theoretically. In the second part, it was shown that a change of Ψ_0 due to the adsorption of charges at the sensor surface can be experimentally addressed by reading out the corresponding change of V_{th} of the SiNW transfer curves. The role of N_s for the pH response was further demonstrated. The requirements for expanding the sensor capabilities to other biochemical species and
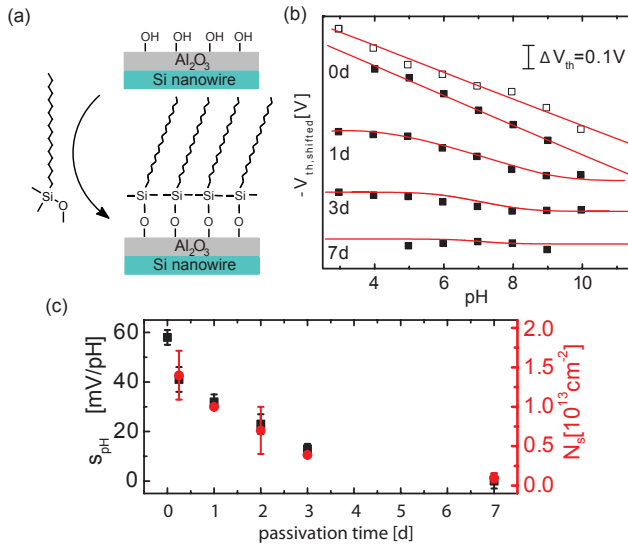
Figure 1.14: (a) Schematic of the Al_2O_3 surface modification using octade-cyldimethylmethoxysilane which replaces the surface hydroxyl groups of the oxide. (b) $-V_{th,shifted}$ versus pH for various functionalization times. Empty squares denote the measurement after 7 days with subsequent cleaning by UV/ozone. Red lines are fits using the site-binding model with $pK_a = 7.2$ and $pK_b = 6.8$, $C_{dl}^{\square} = 0.16\text{F/m}^{-2}$ and N_s used as a fitting parameter as shown in (c). (c) Approximated pH response s_{pH} (black squares, left axis) and N_s (red circles, right axis) versus passivation time. Figures adapted from reference [51].

possible limitations are elaborated in this section.

1.3.1 Response, Sensitivity and Limit of Detection

Besides the response of a sensor, the sensitivity, limit of detection, resolution and signal-to-noise ratio (SNR) are commonly used in literature to describe the sensor performance. Based on the PhD thesis of M. Wipf[7], we define these terms as follows: The input of the sensor is a change of the concentration of the targeted species in the bulk from c_1 to c_2: $\Delta c = c_2 - c_1$. The change in concentration is commonly expressed in terms of the logarithm $\Delta \log a = \log a_2 - \log a_1 = \log(c_2/c_0) - \log(c_1/c_0) = \log(c_2/c_1)$. $c_0 = 1\,\mathrm{M}$ is the concentration of the standard state as introduced in Section 1.1.4. It makes the argument of the logarithm dimensionless leading to the activities $a_1 = c_1/c_0$ and $a_2 = c_2/c_0$. The response is then given by the change of surface potential $\Delta \Psi_0$ upon a change in target concentration

$$response(\Delta \log a) = \frac{\Delta \Psi_0}{\Delta \log a}, \tag{1.27}$$

where $\Delta \Psi_0$ is determined by $-\Delta V_{th}$. The resolution is defined by the smallest change in surface potential $\Delta \Psi_{0,min}$ which can still be observed in the measurement and is determined via the noise measurements as discussed in Section 1.3.3. The resulting signal-to-noise ratio is defined as $SNR = \Delta \Psi_0 / \Delta \Psi_{0,min}$. Note, this definition of the SNR depends on $\Delta \log a$, i.e. the change of the concentration.

The limit of detection (LOD) is given by the minimum detectable concentration $c_{2,min}$ at a certain background concentration c_1:

$$LOD : \log a_{2,min} = \frac{\Delta \Psi_{0,min}}{response(\Delta \log a)} + \log a_1. \tag{1.28}$$

This definition calculates the activity $a_{2,min} = c_{2,min}/c_0$ which leads to the minimum detectable change in surface potential $\Delta \Psi_0 = \Delta \Psi_{0,min}$. This means that $a_{2,min}$ can be detected at background activity a_1 with $SNR = 1$. The LOD increases with analyte activity a_1. The best (i.e. smallest) LOD is detected at the lower end of the concentration range of the sensor. Finally, the sensitivity is the detectable relative change in analyte concentration $\Delta c_{min}/c_1 = (c_{2,min} - c_1)/c_1$. In the following, the sensor response to a target analyte is discussed theoretically and the noise of the transistor is introduced.

1.3.2 The Role of Competing Surface Reactions

The intrinsic pH sensitivity of Al_2O_3 or HfO_2 gate dielectrics as demonstrated in Section 1.2.4 has important consequences for the specific detection of proteins or ions other than protons [54–56]. For such sensing experiments, the oxide surface needs to be modified to specifically detect the targeted species. Besides ion-selective membranes [57,58], self-assembled monolayers (SAMs) of functional molecules have been used for this purpose. In the case of oxide surfaces, the self-assembly of silane monolayers has become a widely used method for functionalization [3,59–61] in which surface hydroxyl groups are replaced by new functional groups. However, a certain number of hydroxyl groups will still remain on the surface and full passivation is very difficult to achieve as discussed in Section 1.2.5.

To understand the measured response of the sensor to changes in analyte concentration, the influence of the remaining hydroxyl groups after functionalization has to be included. Wunderlich and co-workers demonstrated by an analytical description, that the sensitivity to protons can decrease or even suppress the measured signal for protein adsorption [62].

In the following, we start with a simple general site-binding model explaining the influence of a competing reaction on the detection of a targeted species at the ISFET surface. The model assumes perfect selectivity of the surface sites and no competitive binding. It is, however, important to emphasize, that the reactions are still coupled via the surface potential. We show here that this coupling can lead to a full suppression of the response to the targeted species, in agreement with the results of Wunderlich et al. [62] In Chapter 3 we further demonstrate the key features of the model with a real physical sensing example implemented using gold-coated NW FETs functionalized by a SAM of calcium (Ca^{2+}) selective molecules. Thereby we show that in typical ISFET sensing experiments, pH acts as the competing reaction influencing the response to the targeted species. These results have been published elsewhere [63].

The Model

We consider the simplest general case of two competing surface reactions, illustrated in Figure 1.15a. The system consists of a sensor exhibiting two different surface groups L_1 and L_2. The surface is in contact with the liquid containing only two singly-charged species, A_1^+ and A_2^+. Both species can interact with the surface. We assume that A_1^+ specifically binds to L_1 and

A_2^+ specifically to L_2, i.e. the system is orthogonal and we exclude any cross sensitivity. The resulting surface groups are either neutral ($L_1()$ and $L_2()$) or positively charged upon analyte binding ($L_1(A_1^+)$ and $L_2(A_2^+)$). At chemical equilibrium the system can be described by

$$L_1(A_1^+) \rightleftharpoons L_1() + A_1^+, \; K_1$$
$$L_2(A_2^+) \; \rightleftharpoons L_2() + A_2^+, \; K_2.$$
(1.29)
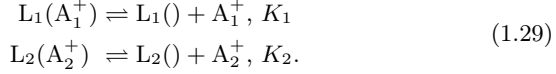
K_1 and K_2 are the dissociation constants defined as

$$K_1 = \nu_{L_1()} a_{1s} / \nu_{L_1(A_1^+)}$$
$$K_2 = \nu_{L_2()} a_{2s} / \nu_{L_2(A_2^+)}$$
(1.30)

with ν being the number of corresponding surface sites per unit area (m^2). a_{1s} (a_{2s}) is the activity of A_1^+ (A_2^+) at the surface. In this model we identify one component, e.g. L_2, as the intrinsic surface reactivity such as the reaction of protons with hydroxyl groups. In the following, we show that, although no cross sensitivity is assumed, the two reactions compete via the surface potential. For each type of surface groups L_1 and L_2, the sum of the number of neutral and positively charged groups per unit area remains constant. For the surface groups L_1, this constant is N_1 whereas for L_2 this constant is given by N_2. We will refer to N_1 and N_2 as total number of surface groups (per unit area):

$$N_1 = \nu_{L_1()} + \nu_{L_1(A_1^+)}$$
$$N_2 = \nu_{L_2()} + \nu_{L_2(A_2^+)}.$$
(1.31)

The reactions with A_1^+ and A_2^+ lead to a surface charge density σ_0 given by the sum of the charged groups

$$\sigma_0 = e(\nu_{L_1(A_1^+)} + \nu_{L_2(A_2^+)})$$
(1.32)

with e the elementary charge. The charged surface builds up a surface potential Ψ_0 which drops over the double layer capacitance $C_{dl}^{\square}$ per unit area:

$$\sigma_0 = C_{dl}^{\square} \Psi_0.$$
(1.33)

We approximate the double layer as a series connection of the Stern layer C_{Stern} and the diffuse layer capacitance C_{dif} to $C_{dl} = C_{dif}C_{Stern}/(C_{dif} + C_{Stern})$. An accepted value for the Stern layer capacitance is given by $C_{Stern}^{\square} = 0.2 \, \mathrm{Fm}^{-2}$ [5,38]. The diffuse double layer capacitance C_{dif} is estimated using the model of a simple parallel plate capacitor depending on
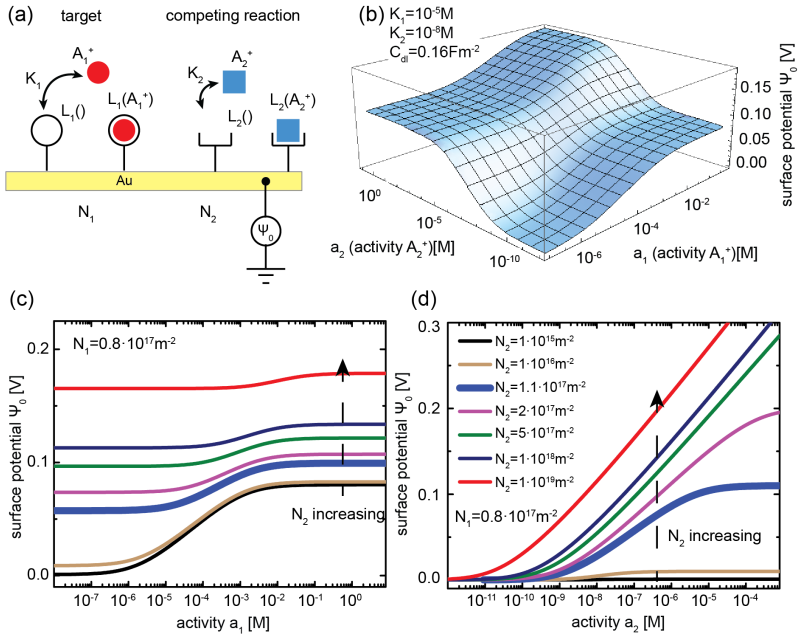
Figure 1.15: (a) General model of two competing surface reactions coupled only via the surface potential Ψ_0. The measurement of the target analyte A_1^+ suffers from the competing reaction involving analyte A_2^+. The parameters describing this system are the dissociation constants K_1, K_2 and the number of surface sites N_1 and N_2. (b) Surface potential Ψ_0 versus the bulk activities a_1 and a_2 calculated using the general model with $K_1 = 10^{-5}$ M, $K_2 = 10^{-8}$ M, $N_1 = 0.8 \cdot 10^{17}$ m^{-2} and $N_2 = 1.1 \cdot 10^{17}$ m^{-2}. (c) Surface potential Ψ_0 versus activity a_1 of target A_1^+ for different N_2 $(N_2 = 1.1 \cdot 10^{17}$ m^{-2} is highlighted by the thick line). The activity $a_2 = 1 \cdot 10^{-7}$M is set constant. Increasing N_2 decreases the response of the sensor towards the targeted analyte A_1^+. Furthermore, the range of activity, where the analyte can be detected, shifts towards higher a_1 for more positive surface potential. (d) Surface potential Ψ_0 versus activity a_2 of the competing species A_2^+ for different N_2 $(N_2 = 1.1 \cdot 10^{17}$ m^{-2} is highlighted by the thick line). The activity $a_1 = 10^{-15}$M is set constant. Figure from reference[63].

the ionic strength of the analyte[51]. To keep the model as simple as possible, we assume a constant value of $C_{dif}^{\square} = 0.7\,\mathrm{Fm}^{-2}$, corresponding to an ionic strength of 100 mM. This results in a double layer capacitance of $C_{dl}^{\square} = 0.16\,\mathrm{Fm}^{-2}$. A constant double layer is a good approximation for detection experiments in physiological solutions where high background salt concentrations are present because C_{Stern} dominates in this case. Furthermore, taking the ionic dependence on the double layer into account does not change the mechanism of competing surface reactions[63]. The potential Ψ_0 established by the surface charge leads to a redistribution of the charged species A_1^+ and A_2^+. The resulting surface activities of A_1^+ and A_2^+ can be related to the bulk activities a_1 for A_1^+ and a_2 for A_2^+ (we skip the index b of the bulk concentration) via the Boltzmann equation:

$$a_{1s} = a_1 e^{-e\Psi_0/kT} \quad \text{and} \quad a_{2s} = a_2 e^{-e\Psi_0/kT}. \tag{1.34}$$

Since the sensor signal is given by the surface potential Ψ_0, we are interested in solving the presented set of equations to obtain an expression for the surface potential as a function of the bulk activities a_1, a_2, the number of the surface sites N_1, N_2 and the dissociation constants K_1 and K_2. Inserting Equation 1.33 in Equation 1.32 yields $\Psi_0 = e(\nu_{\mathrm{L_1(A_1^+)}} + \nu_{\mathrm{L_2(A_2^+)}})/C_{dl}^{\square}$. Both charged surface groups $\nu_{\mathrm{L_1(A_1^+)}}$ and $\nu_{\mathrm{L_2(A_2^+)}}$ can be calculated by inserting the two rate equations 1.30 in the corresponding equations for the total number of surface groups (Equation 1.31) leading to $\nu_{\mathrm{L_1(A_1^+)}} = a_1 N_1/(K_1 + a_1)$ and $\nu_{\mathrm{L_2(A_2^+)}} = a_2 N_2/(K_2 + a_2)$. If we further include our assumption that both A_1^+ and A_2^+ follow a Boltzmann distribution, we obtain the following transcendental equation for Ψ_0

$$\Psi_0 = \frac{eN_1}{C_{dl}^{\square}} \frac{a_1}{K_1 e^{e\Psi_0/kT} + a_1} + \frac{eN_2}{C_{dl}^{\square}} \frac{a_2}{K_2 e^{e\Psi_0/kT} + a_2}, \tag{1.35}$$

where the first term of the sum is determined by the reaction between A_1^+ and L_1 and the second by the reaction between A_2^+ and L_2. Although no analytical solution exists for Ψ_0, Equation 1.35 can be used to determine analytical expressions for $a_1(\Psi_0, a_2)$ and $a_2(\Psi_0, a_1)$. In the following, we will use the latter expressions to calculate the activities a_1 and/or a_2 for a given Ψ_0. For illustrative reasons, we will plot the surface potential Ψ_0 always on the vertical and the activities a_1 and/or a_2 on the horizontal axis, suggesting that $\Psi_0(a_1, a_2)$ is the dependent variable, being a function of the bulk activities a_1 and a_2.

Figure 1.15b shows the surface potential Ψ_0 versus activities a_1 and a_2 calculated for $K_1 = 10^{-5}\,\mathrm{M}$, $K_2 = 10^{-8}\,\mathrm{M}$, $N_1 = 0.8 \cdot 10^{17}\,\mathrm{m}^{-2}$, $N_2 =$

$1.1 \cdot 10^{17} \, \text{m}^{-2}$ and $C_{dl}^{\square} = 0.16 \, \text{Fm}^{-2}$. The values of K_1 and K_2 were chosen such to correspond to typical values of binding constants with the reaction involving L_2 having a higher affinity compared to the other reaction. The densities of surface sites N_1 and N_2 are set to values corresponding to typical gold surfaces as we will see in the results section. The value of $C_{dl}^{\square}$ was motivated above. We observe a sigmoidal (or S-shape) response of the surface potential Ψ_0 upon changing the activity a_1 or a_2. In the four corners of the plot, a change in activity of A_1^+ or A_2^+ does not change the surface potential and hence detection is no longer possible. This is because the activities are either too small or the response is saturated, i.e. all the surface sites are already occupied. In between these boundaries, the surface potential is highly sensitive to changes in concentration of species A_1^+ and A_2^+, which we will therefore call the region of maximum response, in mV/dec.

To better understand the relation between the surface potential and the two bulk activities we emphasize specific limits of the given system. We first focus on the targeted reaction involving species A_1^+ and neglect the influence of the competing reaction by setting $N_2 = 0$. The total potential shift due to the binding of the targeted species A_1^+ is then given by $\Delta_{total,a_1}\Psi_0 = \Psi_0(a_1 \to \infty) - \Psi_0(a_1 \to 0) = eN_1/C_{dl}^{\square}$. The region of maximum response depends on the dissociation constant K_1 for ligand L_1. However, since we assume a Boltzmann distribution of the target analyte, the surface potential also strongly influences the binding. This is expressed by the term $K_1^{effective} = K_1 e^{e\Psi_0/kT}$ which is often called the effective binding constant[64]. For a particular value of a_1 and Ψ_0 such that the condition $a_1 = K_1 e^{e\Psi_0/kT}$ is fulfilled, half of the sites are bound to the analyte and half of the total potential shift is observed. Thus, the region of maximum response greatly depends on the surface potential.

If a competing reaction is present in the system ($N_2 \neq 0$), it will affect the surface potential in a similar way, which results in a nonlinear coupling between the two reactions. The strength of this coupling is given by the ratio N_2/N_1. This is shown in Figure 1.15c for $N_1 = 0.8 \cdot 10^{17} \, \text{m}^{-2}$ and a constant concentration of the competing species $a_2 = 1 \cdot 10^{-7} \, \text{M}$. The detection of a_1 strongly suffers from the competing surface reaction if N_2 is two orders of magnitude larger than N_1. Suppressing the response to a_2 by reducing the number of surface sites N_2 leads to a continuous increase of the response to a_1 until the total potential shift of $80mV$ is achieved for $N_2 = 1 \cdot 10^{15} \, \text{m}^{-2}$. For increasing N_2, the response to a change in target analyte activity a_1 not only decreases, but also shifts towards higher a_1. This is expected, due to the dependence of the effective binding constant on the surface potential.

The higher the surface potential, the more the response region shifts to higher activities. Any charge at the sensor surface will change the region of maximum response of the sensor. Finally, Figure 1.15d shows the response to a_2 for the same set of parameters at $a_1 = 10^{-15}$ M. As expected, the response increases with $\frac{N_2}{N_1}$ and the slope approaches the Nernst limit of ≈ 60 mV/dec for $N_2 = 1 \cdot 10^{19}$ m^{-2}, showing in other words that if one ligand dominates, e.g. L$_2$ ($N_2 \gg N_1$) the surface responds strongly to A$_2^+$ but almost no response is possible for A$_1^+$ (see red curves in Figure 1.15c,d).

In conclusion, we propose a simple, general model to describe the influence of a competing surface reaction for specific detection experiments based on ISFETs. Although the model assumes perfect selectivity of the functionalization and excludes cross sensitivity in binding, up to full suppression to the targeted species can occur. This indirect interference of the competing reaction occurs via the surface potential: The liquid acts as a nonlinear feedback to the sensor response. The model describes the fundamental limits of the sensor response. Since most surfaces have some pH sensitivity, pH is expected to generally compete with the target reaction. N_s is therefore a critical parameter for successful specific sensing, as we will demonstrate in Section 3.1.

1.3.3 Noise

The performance of the ISFET sensor depends not exclusively on the response but also on the electronic noise of the underlying FET. This reflects the fact that a change in surface potential $\Delta\Psi_0$ needs to be resolved, e.g. measured with the transistor. Noise is the random fluctuation of the signal over time and therefore determines the resolution of the smallest change of the sensor signal which can still be observed: $\Delta\Psi_{0,min}$. In electronic devices, different types of noise are present: Thermal noise, shot noise and $1/f$ or flicker noise [65]. The major contribution to the noise in sensing devices is the $1/f$ or Flicker noise. It is characterized by a power spectral density inversely proportional to the frequency f and therefore dominant at low frequencies ($f < 100$ Hz). Since typical detection experiments take about $1-60$ min due to typical binding kinetics [8], the noise at low frequencies strongly limits the performance of the sensor. We will focus on the $1/f$ noise in the following.

$1/f$ noise

In the following we will discuss $1/f$ noise caused by resistance fluctuations. This type of noise is described by the empirical Hooge's law:

$$\frac{S_V}{V_{sd}^2} = \frac{S_{Isd}}{I_{sd}^2} = \frac{\alpha}{N \cdot f} \tag{1.36}$$

with α the dimensionless Hooge's constant, N the number of fluctuators and f the frequency. S_V and S_{Isd} are the noise power spectral densities of the source-drain voltage and source-drain current, respectively. S_V is abbreviated as the voltage noise and S_{Isd} as the current noise in the following. Hooge's law only states that the $1/f$ noise is due to resistance fluctuations[66,67]. Therefore it can be measured as voltage fluctuations corresponding to S_V if the resistor is current biased or as current fluctuations corresponding to S_{Isd} if the resistor is voltage biased.

α-Noise Model

One successful model that expands on Hooge's law assumes that N is given by the number of charge carriers of the sample (in the case of a p-type SiNW, the number of holes) and equals to $N = pWLd$ with p the homogenous hole density, W and L the width and length of the channel and d the thickness. Included in Hooge's law, this yields

$$\frac{S_{Isd}}{I_{sd}^2} = \frac{\alpha}{fpWLd} = \frac{\alpha e \mu V_{sd}}{f I_{sd} L^2} \tag{1.37}$$

with e the elementary charge and μ the hole mobility[68,69]. The right term has been obtained using Ohm's law and the expression for the conductivity $\sigma = p\mu e$. We will refer to this model as the α-noise model[66]. Importantly, it describes noise as a bulk phenomena and scales inversely with sample volume WLd. Although the α-noise model has been widely applied to homogenous samples[66,67,69], it fails to explain the noise observed in MOSFETs, in which charge transport is usually located at the semiconductor/oxide interface. As shown in a previous work[48], the α-noise model also lacks to describe the noise of our SiNW ISFETs. Alternatively, the McWorther model has been successfully applied to MOSFETs. Adapting this model to ISFETs leads to the trap state noise model as discussed next.

Trap State Noise Model

The McWorther model [68] assumes fluctuations in the number of charge carriers due to trapping/ de-trapping at the semiconductor/oxide interface as the major source of the noise. The trapping/de-trapping process leads to a charge noise power spectral density $S_{Q_{ox}}$, abbreviated charge noise in the following. The effect of the charge noise can be expressed as fluctuations of the gate voltage, given by the gate referred voltage noise $S_{V_g} = S_{Q_{ox}}/C_{ox}^2$. S_{V_g} is a theoretical concept and can be regarded as the noise power of the gate voltage if the transistor channel itself was ideal and noise-free. The gate referred noise is observed as current noise in the transistor through the transconductance g_m [48,68,70]:

$$S_{Isd} = g_m^2 \cdot S_{Vg}. \tag{1.38}$$

The model is based on the fact that a large number of Lorentzian spectra $(S(f) \propto f_c/(f_c^2 + f^2))$ with a corresponding wide distribution of the corner frequencies f_c leads to a $1/f$ spectrum as illustrated in Figure 1.16. f_c corresponds to a process with a certain timescale. Physically, generation and recombination noise of the trap states could lead to the observed $1/f$ spectra. Trapping/De-trapping is explained by quantum tunneling from the bulk semiconductor to the traps. The total contribution of the traps results in the following charge noise:

$$S_{Q_{ox}} = \frac{e^2 kT\lambda N_t}{WLf}. \tag{1.39}$$

For further details see [68]. k is the Boltzmann constant, T the absolute temperature and N_t the density of trap states. The tunneling length λ is not observed directly in the noise measurement. Its value is assumed to be in the range of $\approx 10^{-10}$ m which might vary for different materials and devices. It is therefore reasonable to combine λ together with kT and N_t in a single fitting parameter N_{ot} and name the resulting model trap state noise model [48]. Note that both N_{ot} and N_t are named density of trap states and are used in literature.

Using N_{ot}, the gate referred voltage noise S_{Vg} is given in the trap state noise model as

$$S_{Vg} = \frac{S_{Q_{ox}}}{C_{ox}^2} = \frac{e^2 N_{ot}}{WLfC_{ox}^{\square 2}}. \tag{1.40}$$

Recently, noise of nanoscale ISFETs has gained more and more attention [47,70–73]. As shown in a previous work [48], the trap state noise model
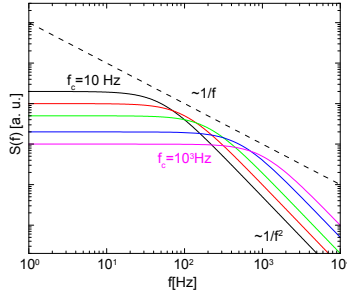
Figure 1.16: Noise power spectral density $S(f)$ versus frequency f of Lorentzian spectra with different corner frequencies $f_c = 10, 100, 200, 500, 1000\,\mathrm{Hz}$.

is in good agreement with the measured data for our SiNWs covered with Al_2O_3 and widths ranging from $W = 100\,\mathrm{nm}$ to $W = 1\,\mu\mathrm{m}$. Most importantly, we observe that the gate referred voltage noise scales with $1/(W \cdot L)$ as predicted by the trap state noise model. The gate referred voltage noise S_{Vg} allows comparing a change in the surface potential $\Delta\Psi_0$ directly with the noise at the gate. As shown in a previous work [47] and briefly mentioned in Section 1.2, this signal is not effected by the transistor dimensions. As a result, the signal-to-noise ratio given by

$$SNR = \frac{\Delta\Psi_0}{\Delta\Psi_{0,min}} = \frac{\Delta\Psi_0}{\sqrt{S_{Vg}}} = \frac{\Delta\Psi_0\sqrt{WLf}C_{ox}^{\square}}{e\sqrt{N_{ot}}} \qquad (1.41)$$

scales with $\sqrt{WL}$.

Interestingly, aggressive scaling is not beneficial to increase the SNR of our NWs. N_{ot} should be minimized by an optimized Si/oxide interface and $C_{ox}^{\square}$ should be maximized. The SNR for smaller structures has not been investigated. For nanoscale ISFETs (50 nm x 50 nm or smaller), the total number of trap states is small and therefore the Lorentzian dependence $S(f) \propto 1/f^2$ becomes visible [72]. For such small structures, the dominant noise source and therefore the scaling with device geometry can be different [73].

Although the trap state noise model agrees well with our noise data, the actual location of the trap states is still unclear [70]. We will address this issue in more detail in Chapter 3 where we extend our noise studies to gold-coated NWs and discuss the influence of N_s and surface functionalization.

1.3.4 Further Limiting Factors

Debye Screening One major limitation of ISFETs has been neglected so far. Detecting charges in an electrolyte always suffers from electrostatic screening due to the rearrangement of counter ions and solvent molecules. Screening has been discussed in various studies[54,74–76]. It is mainly determined by the buffer composition and background electrolyte concentration. The characteristic length over which the potential decreased $1/e$ is given by the Debye length λ_D[54]

$$\lambda_D = \sqrt{\frac{\epsilon\epsilon_0 kT}{2N_A e^2 I_c}}.$$ (1.42)

N_A is the Avogadro constant, $I_c = 1/2 \sum c_i z_i^2$ the ionic strength, c_i the ion concentration in M of ion i and z_i the charge number of the ion. At $1\,\mathrm{mM}$ buffer concentration, $\lambda_D \approx 10\,\mathrm{nm}$. Already at $100\,\mathrm{mM}$ the Debye length has dropped to less than $1\,\mathrm{nm}$. Electrical field screening is a limiting factor for biosensing measurements under physiological conditions where the high electrolyte concentration ($c \approx 150\,\mathrm{mM}$) leads to $\lambda_D < 1\,\mathrm{nm}$. In combination with the large size of proteins, the screening highly complicates the successful protein detection. Proteins are large biomolecules comprising long chains of amino acids and easily exceed one nm. Even worse, linker molecules needed to specifically bind the targeted protein at the sensor surface further increase the distance from the surface where charges get adsorbed. The detection of proteins is therefore a very challenging task[55]. Only recently, several methods have been proposed to overcome the limitations of Debye screening, including readout at high frequencies[77], modification of the NW surface with polymers[78] and even geometrical shaping of the NW to increase the Debye length[76]. However, to minimize the effect of screening, diluted buffers are mostly used[8,45,79]. Additionally, the investigated protein systems are often based on the interaction between biotin and streptavidin, which is one of the strongest non-covalent bindings, leading to relatively high signals. One exception is the detection of cancer markers using SiNWs in undiluted serum samples[80]. The detection of proteins is further discussed in Chapter 4 where a specific, physiologically relevant protein system is studied.

Signal Stability and Drift The fluidic system is another part of the ISFET setup which can limit the sensing performance. In particular, the liquid setup must enable stable gating of SiNW FETs. Furthermore, fast exchange of the analyte solutions should be implemented, minimizing drift in

the measurement. During this PhD project, short and long term stability measurements were performed. Details can be found in the PhD thesis of M. Wipf[7]. The long term stability (drift) measurements were obtained for Al_2O_3 and gold-coated nanowires measured in pH 7 buffered solution. After an initial stabilization time of a few hours, the drift of the threshold voltage reduces to 0.02 mV/h for the gold-coated SiNWs and 0.45 mV/h for the bare Al_2O_3 SiNWs (linear fit over 52 h). Drift between different nanowires with the same surface material was very similar. Therefore, a differential measurement setup as presented in Chapter 2 could compensate long term drifts.

1.4 Summary

This chapter introduced the concept of the ion-sensitive field-effect transistor and discussed the key aspects of this device. Two important models describing the sensor response were presented. Due to its simplicity, the microscopic site-binding model, assuming an ideally-polarized interface, is preferred. By realizing that all reactions at the sensor surface are coupled via the surface potential, we find that the resulting competing effect can lead up to a full suppression of the sensor response to the targeted species. The SiNW ISFETs studied in this thesis show a Nernstian response to pH due to their gate dielectrics of Al_2O_3 and HfO_2. An enhanced response of narrow nanowires compared to wider structures was not found. In fact, even reducing the width of the NWs down to 100 nm did not increase the pH response because the response is limited by the Nernstian equation. It might be argued that the shift in surface potential for a given change in surface charge is larger for small channels, according to $\Delta\Psi_0 = \Delta Q_0/C_{dl}$ since $C_{dl} \propto area$. However, this statement ignores the fact that ΔQ_0 depends on the surface activity and therefore on the surface potential as long as a Boltzmann distribution of the target is assumed. It is again the coupling of the surface activities with the surface potential that ensures that the Nernst equation is not exceeded. The situation might change if large biomolecules are targeted because their surface activity equals approximately the bulk activity and a Boltzmann distribution is not a priori given. Even in this case, charge adsorption should be assumed to be a uniform process, depending only on the binding reactions. Therefore $\Delta\Psi_0 = \Delta Q_0/C_{dl}$ remains independent of the nanowire area because both ΔQ_0 and C_{dl} scale with area. In conclusion, the response cannot be increased using smaller transistor channels under the given assumptions. This means, that the SNR is expected

to increase with area as given by Equation 1.41 stating $SNR \propto \sqrt{WL}$. As third and last idea we assume that the detection of a single species is targeted. In this case, a small capacitance increases the observed shift in surface potential: $\Delta\Psi_0 \propto 1/WL$. If the noise follows the trap state noise model, the SNR scales with $1/\sqrt{WL}$. Therefore, for the detection of single species, nanoscale transistors are expected to be useful. Importantly, while the above argumentation holds for the dimensions studied in thesis, true nanoscale ISFETs could reveal additional effects due to their size. For very small objects, discrete binding sites rather than densities as used in the site-binding model should be assumed. The same holds for the noise which has been found to deviate from the trap state noise model for SOI nano-MOSFETs[72]. Practically, the use of nanostructures is limited by the reaction kinetics and the accumulation time and therefore high stability and low drift are needed to achieve single entity detection. This can be achieved by further downscaling of the fluidic system[43].

2

Beyond pH Sensing: Specific Detection of Ions

After the first successful demonstrations of pH sensing, the ISFET generated great expectations. It was commonly assumed that the same principle could be easily adapted to any other targeted species, provided that the target is captured in the vicinity of the transistor. However, the limitations presented in the previous chapter complicate the specific detection of species other than protons. To use the ISFET for this task, the surface needs to be modified. The use of ion-sensitive membranes is difficult due to the limited stability of the oxide/membrane interface[21,57]. Better stability is achieved when the sensitive layer is covalently bound to the sensor surface[59,81]. In particular self-assembled monolayers (SAMs) of selective linker groups are an interesting approach. As pointed out in Section 1.3.2, a key aspect of the performance of the sensor is the influence of competing surface reactions. Two parameters have to be taken into account: First, a large number of specific groups binding the targeted species has to be achieved. Secondly, any other reaction taking place at the sensor surface should be suppressed to minimize the influence of competing surface reactions.

In this chapter a first attempt towards the proposed system is presented. Using an additional layer of gold reduces the pH response considerably and provides a platform for further surface functionalizations based on SAMs of ion-selective molecules. The monolayers are anchored to the gold layer via the covalent sulfur-gold bond. Besides a residual pH response, the gold layer also exhibits a response to changes in the electrolyte concentration possibly due to unspecific adsorption of anions. To take this contribution into account, a differential measurement setup is proposed. Comparing function-

alized, active nanowires with unfunctionalized, control nanowires yields the response of the ion-selective molecules. In combination with our microfluidic setup the specific detection of sodium (Na^+) and fluoride ions (F^-) is achieved. The differential approach proposed in this chapter is a straightforward method to approximate the specific response, which assumes that all reactions contribute linearly to the surface potential. Although this is a severe simplification as discussed in Section 1.3.2, it compensates for drift [82] and linear background contributions independent of the surface potential as further explained in this chapter.

2.1 Selective Sodium Sensing Using Gold-Coated Nanowires in a Differential Setup

In this section, we modify individual nanowires with thin gold films as a novel approach to surface functionalization for the detection of specific analytes. We functionalize one half of a sample with SAMs of sodium-selective crown ethers whereas the other half remains untreated. Thereby, we obtain two groups of NWs with different surfaces: Gold-coated NWs functionalized by the SAM (active NWs) and non-functionalized NWs with just a bare gold surface (control NWs). We find that the functional SAM does not affect the unspecific response of gold to pH and background ionic species. This property makes gold a possible candidate for differential measurements comparing the response of the active NWs with the control NWs. Using the differential setup, the specific detection of sodium was demonstrated. These results are published elsewhere [83].

2.1.1 Methods

Sample Fabrication   The samples were fabricated using p-doped silicon on insulator (SOI) wafers and a top-down fabrication process as described in Section 1.2. The array used for this study consists of nanowires with widths ranging from 100 nm to 1 μm. For the gold-coated NWs a 5 nm chromium adhesion layer and a 20 nm gold film was evaporated onto the Al_2O_3 dielectric layer. The SEM micrograph in Figure 2.1a shows the lateral dimensions of the gold film, highlighted by the dashed line, with respect to a NW. The gold area was lithographically defined and overlaps the NWs in length and width. Figure 2.1b shows the schematics of the cross section of a device and Figure 2.1c the measurement setup. In this setup, the liquid-gate voltage V_{lg} is applied by a platinum wire immersed in the liquid and the actual

liquid potential V_{ref} is measured by a calomel reference electrode using the liquid cell shown in Figure 1.11.

Surface Functionalization   For immobilization of thiol terminated 15-crown-5, half of the NWs on a sensor chip were covered with 5 nm chromium as adhesion layer and 20 nm gold by e-beam evaporation. The samples were cleaned in O_2 plasma (*Oxford Plasmalab 80 plus*, 30 W, 45 s) and covered with a PDMS microchannel. The 15-crown-5 molecule was synthesized by I. A. Wright from the group of Prof. E. C. Constable from the department of chemistry at the *University of Basel*. A detailed description of the synthesis can be found in the supporting information of reference [83]. The molecules were dissolved in ethanol ($\approx$ 2 mM) and pumped through the (active) microchannels with long stabilization intervals for 16 h. After the functionalization, the channels were rinsed with ethanol and deionized (DI) water.

Analyte Solutions   Standard pH buffer solutions were used for the pH measurement (Titrisol, Merck). KCl (ACS $99.0 - 100.5\%$, Alfa Aesar) and NaCl ($\geq 99.5\%$, Fluka) were dissolved in deionized water (resistivity $= 17\,M\Omega cm$), resulting in a pH value around 6. The concentration range was set from 1 mM to 1 M.

2.1.2 Results and Discussion

Figure 2.1d shows the conductance G versus the liquid potential V_{ref} of a nanowire with a 20 nm thick bare gold film on top. With increasing pH the transfer curve shifts to the right. To quantify the shift we define the threshold voltage V_{th} at a fixed conductance value of 20 nS (indicated by the arrow) as explained in Section 1.2.4. The inset shows the pH response of nanowires with different surface materials. Atomic layer deposited Al_2O_3 shows the expected linear response of $\approx 59\,mV/pH$, due to protonation and deprotonation of surface hydroxyl groups. This response close to the Nernst limit requires a high density of surface hydroxyl groups. Compared to such oxide surfaces, gold also shows a linear response but with a significantly smaller slope of $\approx 38\,mV/pH$. Furthermore, gold-coated NWs show a response to the ionic strength when measuring in NaCl, KCl and NaF solutions, similar to Al_2O_3 and HfO_2. As described in an earlier work [53], we attribute this effect to the unspecific adsorption of anions of the electrolyte at the nanowire surface. Even though the exact mechanism of the anion ad-
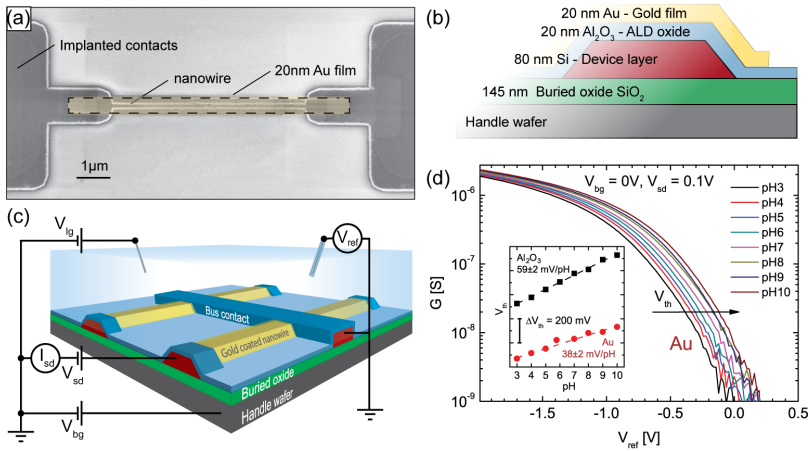
Figure 2.1: Device structure and measurement setup. (a) SEM micrograph of a 150 nm-wide silicon nanowire coated with a 20 nm thick Al_2O_3 dielectric (by atomic layer deposition, ALD). NWs are lithographically defined in silicon on insulator wafers. 5 nm chromium as adhesion layer and 20 nm gold are deposited on top of the nanowire by electron-beam evaporation. Contact regions are highly p-doped. (b) Schematics of a nanowire cross section with the gold film covering the NWs. (c) Schematics of the measurement setup. In this experiment, the liquid-gate voltage V_{lg} is applied by a platinum wire immersed into the electrolyte. The liquid potential V_{ref} is measured by a calomel reference electrode. (d) Conductance curves G versus V_{ref} of a 250 nm-wide gold-coated SiNW in different pH buffer solutions. The transfer curves shift to the right with increasing pH. The threshold voltage V_{th} is defined in the subthreshold regime at a constant conductance value of 20 nS (arrow). Inset: V_{th} at different pH for Al_2O_3 (59.5 mV/pH) and Au (38 mV/pH). Figure adapted from reference [83].

sorption remains unclear, we find that the background electrolyte response is independent of pH and therefore independent of the surface potential [53]. It is therefore a linear contribution which can be compensated in a differential setup [83]. Further details can be found in Appendix B. Even though gold is not expected to be corroded, the moderate response to protons indicates the formation of a gold-oxide layer [84–86]. With the site-binding model [51] we estimate the number of hydroxylated gold surface atoms to be only $\approx 1\%$.

Sodium Sensing

Preparing SAMs of organic molecules at surfaces is an effective functional-ization process for chemical sensing. Functional groups designed for trapping specific analytes can be immobilized close to the surface in this way. Crown ethers, consisting of a ring containing several ether groups, strongly bind cations due to the negatively polarized oxygen atoms. The selectivity to the type of ion can be controlled by varying the number of ether groups and the cavity diameter[87]. Here we used a Na^+-selective 15-crown-5 func-tionalized with a dithiolane anchoring moiety (Figure 2.2d). The samples were cleaned in oxygen plasma and closed with a PDMS microchannel. The samples were divided in two (active and control) parts by individual chan-nels in the PDMS. The wires in the active channel were then functionalized with the 15-crown-5. This results in a differential setup having both, NWs with functionalized gold surface (active NWs) and bare gold-coated NWs (control NWs), on the same chip.

Figure 2.2a shows the response of an active and a control NW to NaCl. For the control NW, we find a positive shift in V_{th} with increasing salt concentration probably due to nonspecific adsorption of electrolyte anions on the gold surface, in this case, Cl^-. The immobilization of the 15-crown-5 changes this response: Instead of the positive shift, a slightly negative shift is observed for the active NW, indicating adsorption of positive charges on the surface. The differential signal ($\Delta V_{th} = V_{th, active} - V_{th, control}$) shown in Figure 2.2e shows a response to NaCl of $\approx -44\,\mathrm{mV/dec}$. Control measurements with KCl in Figure 2.2b show no difference between bare and functionalized gold, suggesting a high selectivity of the 15-crown-5 towards Na^+ and none for K^+. In the case of pH response (Figure 2.2c) the two different surfaces behave the same way. The differential signal (ΔV_{th}) in Figure 2.2e emphasizes that only a change in Na^+ concentration induces a different response of the two surfaces. Thus a good Na^+ sensor with high response and specificity was realized.

The presented measurements indicate that protonation and deprotona-tion of surface hydroxyl groups, as well as the unspecific adsorption of Cl^- are unaffected by the self-assembly of the crown ethers. This experimental fact leads to the conclusion that the SAM does not fully cover the gold sur-face which is further confirmed by the sub-Nernstian response to sodium. In Figure 2.2d we propose a functionalization scheme where the sulfur-gold binding only happens at non-oxidized gold atoms ($\approx 99\%$ of the surface), leaving the number of hydroxyl groups unchanged[85]. The crown ether func-tionalization adds another type of surface reaction to the system, without

affecting the number of hydroxyl groups and the interaction of the gold surface with the electrolyte. The resulting surface consists of small fractions of oxidized gold atoms ($\approx 1\%$) and 15-crown-5 molecules and a large fraction of bare gold atoms. It was assumed that the adsorption of chloride ions takes place at the positively charged OH_2^+ groups as shown in Figure 2.2d [53,83]. However, the shift could also be explained by adsorption at other sites and further studies are needed to understand the exact process of anion adsorption on gold. Although the microscopic picture of the anion adsorption is not complete yet, the shift is experimentally found to be independent of pH and the surface potential. It can therefore be treated as a linear background contribution using the proposed differential response.

2.1.3 Conclusion

In conclusion we demonstrate a selective cation sensing by the self-assembly of Na^+-selective crown ethers on gold-coated NWs. In a differential measurement with active and control NWs on the same chip, a response of $\approx -44\,\mathrm{mV/dec}$ in the concentration range of $1\,\mathrm{mM}$ up to $1\,\mathrm{M}$ was achieved. The response to NaCl is more than an order of magnitude larger than for KCl, indicating good selectivity. We showed that gold surfaces are slightly sensitive to changes in pH which indicates a small density of hydroxyl groups at the gold surface. Furthermore, a response to changes in electrolyte background concentration is observed. We infer from our measurements that the thiol-gold binding during the SAM formation happens only at non-oxidized gold atoms, leaving the number of hydroxyl groups unchanged. As a consequence, the thiol functionalization of gold does not affect the pH sensitivity. Similarly the response to background electrolyte concentration caused by adsorption of Cl^- is also not affected by the functionalization.

2.2 Multiple Ion Detection

A key advantage of silicon based chemical devices is the possibility of large integration. Using a sensor array rather than a single sensor allows implementing different functionalities on a single sample. Applying this concept to chemical sensors leads to a multiplexing platform converting various chemical signals into electrical ones.

In this section, we make a first step towards such a system by demonstrating the simultaneous detection of sodium and fluoride ions with an array of gold-coated SiNW FETs. This is achieved with self-assembled monolayers
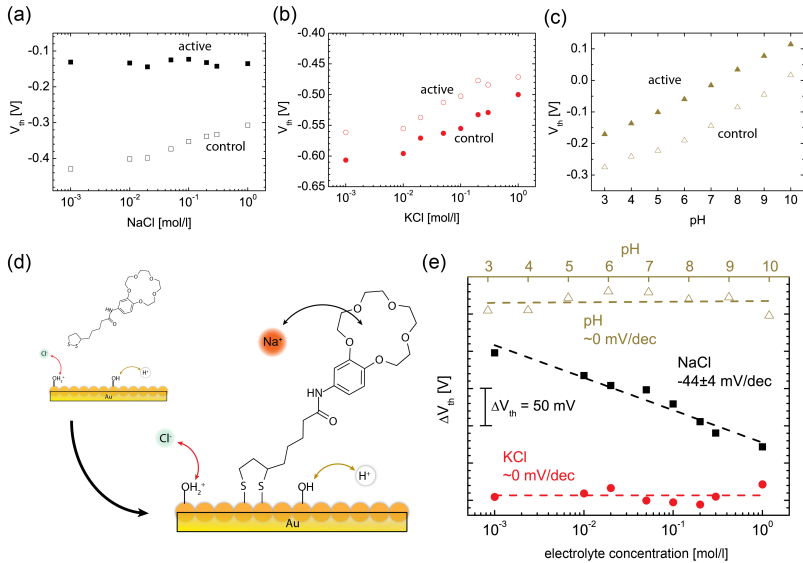
Figure 2.2: Surface functionalization with 15-crown-5 for Na$^+$ sensing.
(a-c) V_{th} for a $1\,\mu$m-wide functionalized (active) and 400 nm-wide bare gold (control) NWs against c[NaCl] (a), c[KCl] (b) and pH (c). The response to NaCl changes with crown ether functionalization, whereas no difference between active and control NWs is seen when measuring in KCl and pH buffer solutions. (d) Immobilization reaction scheme of the sodium-selective crown ether on gold. We propose that the thiol only reacts with (reduced) gold atoms, leaving the number of hydroxyl groups unchanged. Adsorption of chloride ions on positively charged surface groups is a possible explanation of the observed response of gold to changes in electrolyte concentration. (e) Differential threshold voltage (ΔV_{th}) of gold-coated NWs (active 15-crown-5 - control gold) versus the electrolyte concentration and pH. The crown ether shows high selectivity towards Na$^+$. Figure adapted from reference [83].
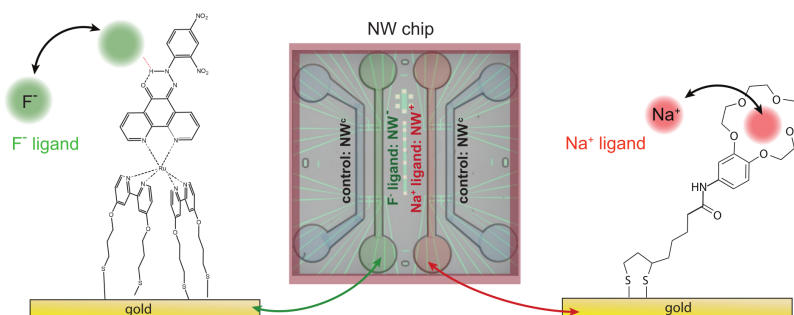
Figure 2.3: Schematics of the functionalization setup and molecular structure of the F^- ligand (left) and the Na^+ ligand (right) immobilized on the gold surface. Middle: Schematics of the NW chip covered by microfluidic cell. Four channels are incorporated in our design, each containing 12 NWs.

of functional molecules anchored on the gold surface. A PDMS microfluidic cell with four individual channels allows functionalizing the device with SAMs of different functional molecules, implementing multi-functionality. Our results demonstrate the usage of SiNW sensor arrays as a promising method to achieve a multifunctional sensing platform.

2.2.1 Methods

Surface Functionalization   To achieve the parallel detection of multiple species with a single chip the functionalization procedure must result in different surfaces, each specific to a certain target. We functionalize the gold surface of the SiNW FETs with self-assembled monolayers (SAMs) of two different ion receptors as illustrated in Figure 2.3. The first molecule (F^- ligand) comprises a metal complex and a fluoride receptive phenathroline ligand which binds fluoride ions (F^-). The second molecule (Na^+ ligand) consists of the 15-crown-5 crown ether structure presented in the last section. The F^- ligands and Na^+ ligands have been synthesized by S. Müller and I. A. Wight from the group of Prof. E. C. Constable at the department of chemistry at the *University of Basel*.

To functionalize the chip, we use PDMS microchannels. The channels were produced by pouring PDMS (Sylgard 184 Silicone elastomer) onto SU-8 patterned Si wafers and curing at $60\,^\circ$C for 2h. Four channels are incorporated in our design, each containing 12 NWs as depicted in Figure
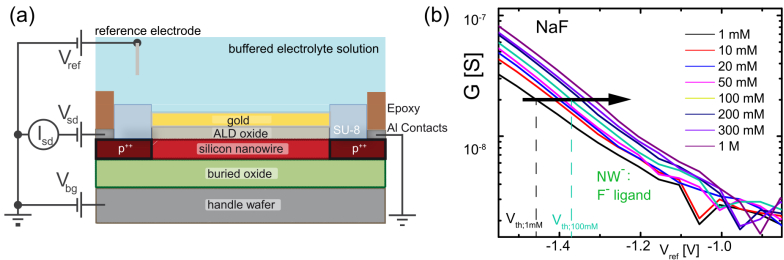
Figure 2.4: (a) Measurement setup as presented in Section 1.2. (b) Conductance G versus liquid-gate potential V_{ref} of a $1\,\mu$m-wide nanowire functionalized with the F^- ligand measured in buffered solutions with increasing NaF concentrations. The curves shift to the right with increasing concentration indicating adsorption of negatively charged species at the surface. The threshold voltage is determined as the value of V_{ref} at a constant conductance value in the subthreshold as indicated by the black arrow.

2.3. The ion receptors were dissolved in methanol ($\approx 1\,$mM). The sample was cleaned by UV/ozone and closed with the PDMS microchannel. PTFE tubes were used to connect the two active microchannels to a peristaltic pump and the two solutions containing the ion receptors. SAMs were obtained by pumping the solutions through the channels with long stabilization times for 12h. We functionalized the NWs in one channel with F^- ligands (resulting in NW^-) and the NWs in another channel with Na^+ ligands (resulting in NW^+). The nanowires in the two remaining channels were used as a control (NW^c) to monitor any changes in background electrolyte concentration and pH. This results in a differential setup having both active NW^- and NW^+ and NW^c on the same chip. After the functionalization, the active channels were flushed with methanol for $10\,$min. Finally, the PDMS cell was removed and the samples were flushed with DI-water. For the measurements, the liquid cell shown in Figure 1.11a was used.

2.2.2 Results and Discussion

Figure 2.4a shows the measurement setup as introduced in Section 1.2.3 where the liquid-gate voltage V_{ref} is directly applied to the reference electrode. In Figure 2.4b we plot the transfer curves (conductance G versus liquid-gate potential V_{ref}) for a gold-coated nanowire functionalized with
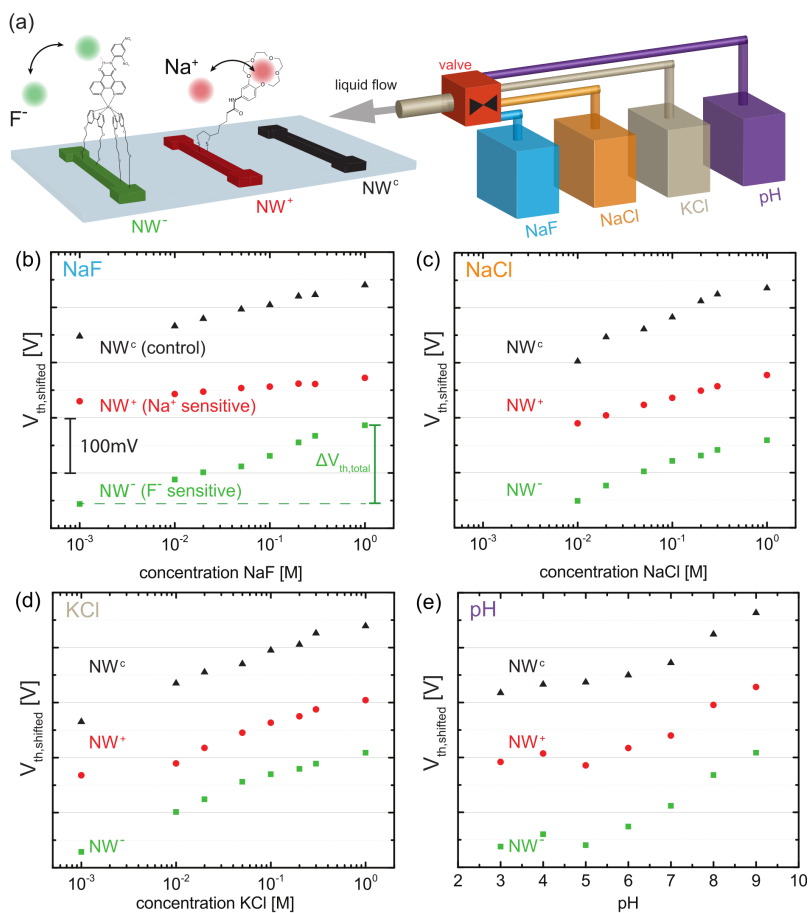
Figure 2.5: (a) Schematics of the ion detection experiment. The response of a specific triplet of NWs consisting of a NW functionalized with SAMs of F^- ligands (NW^-, green), a NW functionalized with SAMs of Na^+ ligands (NW^+, red) and a NW with bare gold surface (NW^c, black) is measured in presence of NaF (blue), NaCl (orange), KCl (brown) and pH (violet). (b-e) Experimental data (threshold voltage V_{th} versus concentration) for (b) NaF, (c) NaCl, (d) KCl and (e) pH. Note that the experimental points of each NW was shifted along the vertical axis leading to $V_{th,shifted}$.

a SAM of F^- ligands (NW$^-$) measured in buffered solutions with varying
NaF concentration from 1 mM to 1 M. The curves shift to the right indicat-
ing the adsorption of negatively charged F^- ions. To quantify the shift, we
extract the threshold voltage V_{th} at a constant conductance value of 20 nS
in the subthreshold, indicated by the black arrow in Figure 2.4b. In the
following, we use V_{th} to quantify the response of the different nanowires
to changes in electrolyte concentration. In total, the response of a subset
consisting of 14 out of 48 nanowires (4 NW$^-$, 4 NW$^+$ and 6 NW^c) was
measured in order to minimize the measurement time. For the sake of clar-
ity, we discuss here the results for a specific NW triplet consisting of one
NW$^-$, one NW$^+$ and one NW^c as depicted in Figure 2.5a. The wires were
chosen such to represent functioning devices, showing a similar behavior in
the control measurements in KCl and pH solutions as observed in previous
measurements[83].

In the following, we compare the response of these three devices mea-
sured for increasing salt concentration (1 mM to 1 M) of NaF, NaCl and
KCl and changing pH from pH 3 to pH 9 (Figure 2.5b-e). In particular,
we investigate whether we can discriminate between sodium and fluoride
ions by comparing the response of NW$^-$ and NW$^+$ with the control NW^c.
Figure 2.5b shows the threshold voltages for the selected NW triplet in NaF
solution. Green squares correspond to V_{th} for NW$^-$ shown in Figure 2.4b.
The threshold voltage V_{th} increases with salt concentration. We define the
total change of the threshold voltage as $\Delta V_{th,total} = V_{th}(1\,\text{M}) - V_{th}(1\,\text{mM})$.
For NW$^-$, $\Delta V_{th,total} \approx 150$ mV as indicated in Figure 2.5b. Additionally,
the threshold voltage of NW^c (black triangles) and NW$^+$ (red circles) are
shown. Note that NW^c exhibits a response to changes in NaF concentration
with $\Delta V_{th,total} \approx 100$ mV. We attribute this response to the non-specific
adsorption of fluoride ions at the bare gold surface, similarly to what we
observed in our previous work for chloride ions.[53,83] Interestingly, NW$^+$
shows even a smaller $\Delta V_{th,total} \approx 50$ mV over the investigated concentra-
tion range. The observed behavior of the three different surfaces agrees well
with the following picture: The largest response is observed for NW$^-$ due
to the adsorption of fluoride ions at the SAM. The smaller response of NW^c
corresponds to the non-specific adsorption of fluoride ions. Therefore, we
conclude that the response measured for NW$^-$ partially includes contribu-
tions from non-specific adsorption of fluoride ions at the gold surface. The
smallest response is observed for NW$^+$ due to the additional adsorption
of Na$^+$ ions in the crown ether, partially compensating the effect of non-
specific fluoride adsorption. We repeated the measurement for the same set
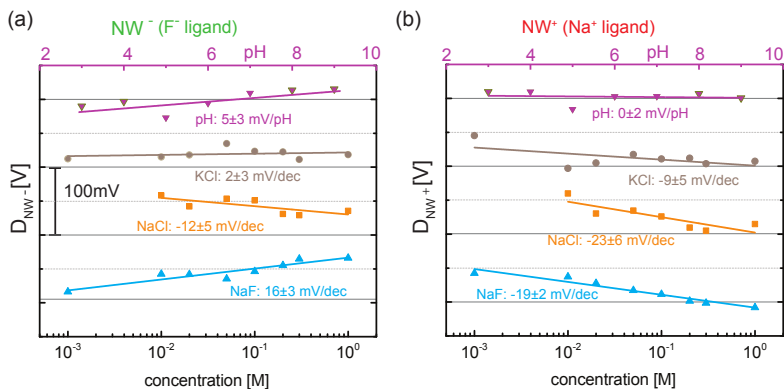of NWs for increasing NaCl (Figure 2.5c) and KCl (Figure 2.5d) concen-

Figure 2.6: (a) Differential response ($D_{NW^-} = V_{th;NW^-} - V_{th;NW^c}$) for NW^- (F^- ligand) and (b) differential response ($D_{NW^+} = V_{th;NW^+} - V_{th;NW^c}$) for NW^+ (Na^+ ligand). In case of NaF, the simultaneous detection of fluoride and sodium ions is achieved.

tration. For both salts, NW^c shows a response to changes in concentration due to the non-specific adsorption of chloride ions, in agreement with our previous work[63,83]. Furthermore, all three NWs exhibit a similar response to pH, as shown in Figure 2.5e, which is attributed to the presence of a low density of oxidized gold surface atoms[83].

To account for the non-specific anion adsorption at the gold surface, we follow the differential approach as introduced in our previous work[63,83]. Thereby, we subtract the threshold voltage of NW^c (V_{th,NW^c}) from the two active NWs (V_{th,NW^+} and V_{th,NW^-}) leading to the differential signal $D_{NW^-} = V_{th,NW^-} - V_{th,NW^c}$ for NW^- and $D_{NW^+} = V_{th,NW^+} - V_{th,NW^c}$ for NW^+ as shown in Figure 2.6. It reveals the response of the two ligands (Figure 2.6a: F^- ligand, Figure 2.6b: Na^+ ligand) and allows a quantitative comparison of the different surfaces. Negligible or weak responses to pH and changes in KCl concentration are observed for both ligands. This indicates that the functionalization does not influence the pH response and that neither potassium nor chloride ions bind to the two ligands. When changing NaCl and NaF concentration, however, a clearer differential response of $\approx -20\,\mathrm{mV}$ per decade (mV/dec) in salt concentration is observed for NW^+, which is due to the sensitivity of the Na^+ ligand to sodium. Note that the sign of the differential response indicates the adsorption of posi-

tively charge sodium ions. While NW^+ shows only a differential response when sodium ions are present, a similar behavior is expected from NW^- for fluoride ions. However, due to the negatively charged fluoride ions, a positive differential response is predicted in this case. Indeed, we find for NW^- a differential response of $+16\,mV/dec$ in NaF due to the adsorption of F^- at the SAM. Therefore the simultaneous detection of sodium and fluoride ions in NaF is achieved. Finally, we also observe a differential response for NW^- of $-12\,mV/dec$ in NaCl which points towards some non-specific adsorption of sodium ions at the SAM. However, cation adsorption is not expected from the structure of the F^- ligand and further measurements are needed to verify this finding.

The response of the NW^+ to changes in NaCl concentration is $\approx -26\,mV/dec$ which is lower than the value of $\approx -40\,mV/dec$ given in the previous section of this chapter. We attribute this decreased response to a decreased density of binding sites resulting from the surface functionalization with the Na^+ ligand. The lower density of the SAM is possibly due to the shorter functionalization time ($12\,h$ compared to $16\,h$) or the change of the solvent from ethanol to methanol. Generally, the quality of the self-assembled monolayer depends critically on the functionalization conditions. The reproducibility of the quality of the SAM is therefore a key element for the further success of sensing platforms based on monolayers of functional molecules. The response of the NW^- is slightly higher when measuring in NaCl solutions compared to NaF but lies within the error of our differential approach.

2.2.3 Conclusion

In conclusion, we have demonstrated the simultaneous detection of sodium and fluoride ions measured in NaF solutions with an array of SiNWs operated as ISFETs. Thanks to microfluidic channels incorporated in a piece of PDMS, we were able to functionalize individual parts of the sample with two different molecules selective for sodium and fluoride ions, while having control nanowires to monitor any changes in electrolyte concentration or pH. Our functionalization procedure results in a differential measurement setup having the functionalized active NWs and the bare gold control on the same sample. After background subtraction, the differential response reveals the signal from the functional molecules. Using this differential setup, responses $\approx 16\,mV/dec$ for F^- and $\approx -20\,mV/dec$ for Na^+ have been demonstrated.

2.3 Summary

In this chapter, gold-coated Si nanowires were introduced as an approach for the specific detection of ionic species. In combination with a microfluidic system, a differential setup is achieved having both functionalized, active NWs and bare gold-coated control NWs on the same chip. To determine the response of different functional molecules to various ionic species, the differential response $\Delta V_{th} = V_{th,active} - V_{th,control}$ is calculated. The additional gold layer drastically decreases the influence of pH and exhibits a platform for anchoring ion-sensitive molecules on the sensor surface using the sulfur-gold bond. Besides the residual pH response, a response to changes in background electrolyte concentration is observed, similar to oxide surfaces [53,83].

The differential approach is a very simple method to take this additional contributions into account, by assuming that all reactions add linearly. It is also expected to compensate for drift [82,83]. Thanks to the reduced pH sensitivity of the gold surface, the competing effect of pH does not prevent the detection of the targeted species. However, the situation might be different when repeating these measurements at different pH values. Due to the difference in surface potential, the effective binding constant $K_1^{effective} = K_1 e^{e\Psi_0/kT}$ of the targeted species changes. Even the moderate pH response of the gold surface of $30 - 40\,\mathrm{mV/pH}$ could thereby change the effective binding constant by more than 3 orders of magnitudes for a singly charged ion. As a consequence, the response is highly affected by the pH which could lead to a decreased response to the targeted species. We expand our discussion of the influence of the surface potential on the specific detection of ions in the first section of the next chapter.

3

Understanding the Limiting Factors for Specific Chemical Sensing

In the previous chapter, successful ion detection was demonstrated using gold-coated SiNWs functionalized with ion-selective molecules. The question appears how applicable this approach is to other detection experiments and under which conditions a good sensor performance is expected. Therefore, possible limiting factors need to be discussed and strategies for improving the sensor performance have to be formulated and validated experimentally. As a key parameter, we introduced the signal-to-noise ratio (SNR) in Section 1.3. Both contributions of the SNR are investigated in detail in the case of gold-coated nanowires in the following. The use of gold as sensor material was motivated by its low number of surface hydroxyl groups N_s and the possibility of using thiol-based chemistry for surface functionalization. Although a passivated Al_2O_3 surface as demonstrated in Section 1.2.5 might be favored due to its even lower N_s, we prefer the gold-coating due to its simple fabrication and functionalization.

The sensor/electrolyte interface determines the response of the sensor. The reduced pH response of the gold layer enables the specific detection of species other than protons. However, the residual pH response still influences the effective binding constant of the targeted species via the surface potential. This effect of pH on the specific detection is studied experimentally in the first part of this chapter. Besides the response, the noise of the transistor determines the SNR. As briefly discussed in Section 1.3 and demonstrated in an earlier work[48], the noise in our devices is well described by the trap state noise model assuming charge trap states as the major source of noise. However, the actual location of the trap states remains an

open question and noise contributions from the sensor/electrolyte interface should not be excluded a priori. To validate our gold-based approach, the effect of the surface modifications on the noise properties has to be further studied as presented in the second part of this chapter.

3.1 Competing Surface Reactions Limiting the Response to Calcium Ions

In this section, we adapt the theoretical model described in Section 1.3.2 to a real sensing example based on gold-coated SiNWs functionalized with a SAM of calcium-sensitive molecules. These results have been published elsewhere[63].

3.1.1 Material and Methods

Gold-coated SiNW ISFETs were functionalized with calcium-sensitive molecules and the response to calcium ions in buffered solutions at different pH is investigated.
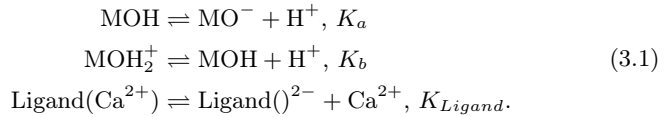
Surface Functionalization   The samples were cleaned in UV/ozone (20 min) and closed with a PDMS microchannel. The sample is divided in two parts by the microchannel: One control channel and one for surface functionalization (active). The Ca^{2+}-sensitive ligand was synthesized by I. A. Wright from the group of Prof. E. C. Constable at the department of chemistry at the *University of Basel* and dissolved in methanol ($\approx 2\,mM$). The active channel was then functionalized with the ligand by pumping the solution through the active microchannel with long stabilization intervals for 8 h. After functionalization the channels were rinsed with methanol. Then, the active channel was flushed with aqueous ammonia (10%) to remove the methyl esters for another 8 h. Finally the active channel was rinsed with deionized water. As a result, we achieve a differential setup having both functionalized and control NWs on the same device. Figure 3.1a shows the schematic of a cross section of a gold-coated NW after functionalization with the ligand.

Electrical Measurements in Liquid $CaCl_2$ ($\geq 93.0\%$, anhydrous, Sigma-Aldrich), KCl (ACS $99.0 - 100.5\%$, Alfa Aesar) and NaF (ACS $\geq 99\%$, Sigma-Aldrich) were dissolved in deionized water (resistivity $= 18\,M\Omega cm$)

and buffered around pH 7 with HEPES ($\approx 4\,$mM, AppliChem) and solution of KOH ($\approx 1.5\,$mM, Merck). For CaCl$_2$-solutions around pH 3, HCl ($\approx 1.5\,$mM, Sigma-Aldrich) was added to the buffered solution. For CaCl$_2$-solutions around pH 10, KOH ($\approx 2\,$mM) was added to the unbuffered solutions. For the pH measurement from pH 3 to pH 10, standard pH buffer solutions (Titrisol, Merck) were used. The exchange of the analyte solutions and electrical measurements were obtained as described in Section 1.2.2.

3.1.2 Results and Discussion

Figure 3.1a shows the schematic of an active nanowire ISFET after surface functionalization. The SAM of calcium-sensitive molecules leads to a new surface group ('Ligand'). The deprotonated carboxylic acid groups of the ligands have a high affinity towards calcium ions. Unlike in the general case, the groups resulting from the functionalization are negatively charged (Ligand()$^{2-}$) in the unbound state and become neutral upon Ca^{2+} binding (Ligand(Ca^{2+})). Besides the groups resulting from the functionalization, additional hydroxyl groups (MOH) have to be assumed due to the residual pH response of gold. These hydroxyl groups can protonate or deprotonate leading to positively charged MOH$_2^+$ and negatively charged MO$^-$ besides the neutral MOH groups. Following the general model, the system can be described by three equilibrations:

$$\mathrm{MOH} \rightleftharpoons \mathrm{MO}^- + \mathrm{H}^+,\ K_a$$
$$\mathrm{MOH}_2^+ \rightleftharpoons \mathrm{MOH} + \mathrm{H}^+,\ K_b \qquad (3.1)$$
$$\mathrm{Ligand}(\mathrm{Ca}^{2+}) \rightleftharpoons \mathrm{Ligand}()^{2-} + \mathrm{Ca}^{2+},\ K_{Ligand}.$$

K_a, K_b and K_{Ligand} are the dissociation constants and the total number of surface sites per unit area is $N_s = \nu_{\mathrm{MOH}_2^+} + \nu_{\mathrm{MO}^-} + \nu_{\mathrm{OH}}$ for the hydroxyl groups and $N_{\mathrm{Ligand}} = \nu_{\mathrm{Ligand}()^{2-}} + \nu_{\mathrm{Ligand}(\mathrm{Ca}^{2+})}$ for the ligand. We assume that the charged ligands are located directly at the surface plane, which is a severe simplification of the electrostatic problem. In reality, the groups of the ligand will be distributed within a certain distance from the surface and additional electrostatic effects such as screening will be present. To keep the model as simple as possible, we neglect these effects. The qualitative influence of the competing reaction is independent thereof. The surface charge density is finally given by

$$\sigma_0 = e(\nu_{\mathrm{MOH}_2^+} - \nu_{\mathrm{MO}^-} - 2\nu_{\mathrm{Ligand}()^{2-}}) = C_{dl}^{\square}\Psi_0. \qquad (3.2)$$
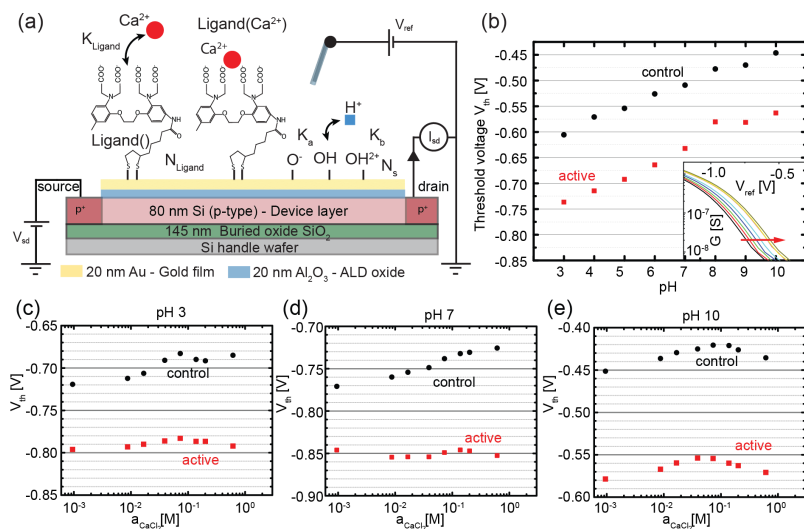
Figure 3.1: (a) Schematics of a specific realization of the sensing model with pH as competing surface reaction. The gold surface of the sensor is functionalized using calcium-sensitive molecules ('Ligand'). The total number of molecules is given by N_{Ligand}. The functionalization results in two surface groups, namely Ligand(Ca^{2+}) and Ligand() for the molecule bound/unbound to the target. Besides these two groups due to the functionalization, additional hydroxyl groups are present, being subject to protonation and deprotonation. The total number of hydroxyl groups is given by N_s consisting of negatively charged O^-, positively charged OH_2^+ as well as neutral OH groups. The reaction of these surface groups with protons and calcium ions of the solution builds up a surface potential Ψ_0. In this setup, a liquid-gate voltage V_{ref} is applied to the reference electrode. A constant source-drain voltage of $V_{sd} = 100$ mM is applied and the source-drain current I_{sd} through the nanowire is measured. (b) Threshold voltage V_{th} versus pH of a functionalized NW (active) and a bare gold NW (control). The threshold voltage V_{th} has been extracted from the transfer characteristics of the NW ISFET as exemplified in the inset. The inset shows the conductance G versus liquid-gate potential V_{ref} for the active NW measured in different pH solutions. To quantify the pH response, we read out the threshold voltage V_{th} as a value of V_{ref} at a constant conductance value $G = 20$ nS as indicated by the red arrow. (c-e) Threshold voltage V_{th} versus activity of $CaCl_2$ of the same pair of active and control NW as shown in (b), measured at different pH values. Figures adapted from reference [63].

Including the Boltzmann distribution for both protons $(a_{H_s^+} = a_{H^+}e^{-e\Psi_0/kT})$ and calcium ions $(a_{Ca_s^{2+}} = a_{Ca^{2+}}e^{-2e\Psi_0/kT})$ leads to

$$
\begin{aligned}
\Psi_0 =&\, 2e\frac{N_{Ligand}}{C_{dl}^{\square}}(\frac{a_{Ca^{2+}}}{a_{Ca^{2+}} + K_{Ligand}e^{2e\Psi_0/kT}} - 1) \\
&+ e\frac{N_s}{C_{dl}^{\square}}\frac{a_{H^+}^2 - K_aK_be^{-2e\Psi_0/kT}}{a_{H^+}^2 + a_{H^+}K_be^{e\Psi_0/kT} + K_aK_be^{2e\Psi_0/kT}},
\end{aligned}
\tag{3.3}
$$

where the first term is due to the functionalized groups, the second term the intrinsic sensitivity to protons. Similar to the general case, Equation 3.3 can be solved analytically for the bulk activities of protons a_{H^+} and calcium ions $a_{Ca^{2+}}$.

After adapting the general model to the specific implementation with functionalized gold-coated NWs, let us now turn to the experimental data. Figure 3.1b shows the threshold voltage V_{th} of a functionalized (active) NW and a bare gold-coated (control) NW to changes in pH. Both surfaces show a nearly linear response with a slope of $\approx 30\,\text{mV/dec}$. V_{th} changes towards more positive values for increasing pH, meaning that the surface becomes more negatively charged. The moderate sensitivity of the bare gold surface to pH has been explained by the formation of gold oxide[83]. Figure 3.1b also shows that the functionalization does not change the response to pH, in agreement with previous work[83]. Moreover, the deprotonated carboxylic acid of the ligand seems not to change the pH response either, due to its low pKa value (< 3)[1]. Both observations indicate that the number of surface hydroxyl groups responsible for the moderate pH response is not affected by the functionalization.

Figure 3.1c,d,e show the V_{th} of the same pair of active and control devices for changing concentration of CaCl$_2$, from $1\,\text{mM}$ to $1\,\text{M}$ at pH 3, pH 7 and pH 10. Instead of the electrolyte concentration, we will now use the activity of the calcium ions $a_{Ca^{2+}}$ on the horizontal axis. This allows the direct comparison of the measured data with the model. Here, the activity is estimated using the standard Debye-Hückel approximation[28].

The control NWs show a response to changes in CaCl$_2$ concentration due to some unspecific adsorption of species of the electrolyte. To remove this background signal, we calculate the differential response, which is our sensor signal, given by $\Delta V_{th} = V_{th;active} - V_{th;control}$ and fit the data to the model. Note, the model describes the potential of the active NW. Fitting

---

[1]Similar functional groups show pKa values < 3, see database compiled by R. Williams[88].

the data of the differential response with this model is therefore a priori not correct. However, we find that the background response due to unspecific adsorption of charged species in the electrolyte is a linear effect, independent of the surface potential as discussed in Chapter 2 and Appendix B. As a consequence, the intrinsic pH sensitivity of the control NW is only slightly affecting the unspecific background response. We can thus approximate the background contribution due to unspecific adsorption using the response measured with the control NW. Since we assume a Boltzmann distribution of the calcium ions, the influence of the pH on the specific adsorption of Ca^{2+} via the surface potential is much more pronounced. In fact, as shown in this work, the influence of pH cannot be eliminated in a differential setup, because of the coupling with the surface potential.

We use the pH measurement of three typical control nanowires as shown in Figure 3.2a to estimate the unknown parameters for the proton reactions N_s, K_a, K_b. In Figure 3.2a, the measured threshold voltage V_{th} of each NW has been converted to the surface potential via $\Psi_0 = V_{th}(PZC) - V_{th}$, where $V_{th}(PZC)$ is the threshold voltage at the assumed point of zero charge (PZC). This conversion is similar to previous work[51,53]. We find that a PZC between 6 and 7 gives a good fit with the data. We choose the set of parameters $K_a = 10^{-8}$ M, $K_b = 10^{-6}$ M (leading to a PZC=7) and $N_s = 1.1 \cdot 10^{17}\,\mathrm{m}^{-2}$ (black solid curves in Figure 3.2a) which agrees well with the measured data. The dashed curves in Figure 3.2a show curves plotted for different values of K_a and K_b.

Figure 3.2b shows the sensor response to $CaCl_2$ (solid symbols) for three different pH values. Because calcium ions carry two charges (Ca^{2+}), the maximum possible (Nernstian) response to calcium is given by 29.8 mV/dec. On the vertical axis of Figure 3.2b, the measured differential threshold voltage for each pH value ΔV_{th} is converted to the surface potential using $\Psi_0 = V_{const} - \Delta V_{th}$ where V_{const} is a constant offset chosen such that the measurement points level with the theoretical surface potential. We find that at pH 10, the response to calcium ions is already saturated at $a_{Ca^{2+}} = 1\,\mathrm{mM}$ and the targeted ion cannot be detected. At pH 7 and pH 3, we find a clear response of $\approx 20\,\mathrm{mV/dec}$, which is two-thirds of the Nernstian response. $K_{Ligand} = 50\,\mathrm{mM}$ and $N_{Ligand} = 0.6 \cdot 10^{17}\,\mathrm{m}^{-2}$ yields good agreement with the data for all pH values (solid curves). The dissociation constant is much higher than expected[89]. This can be attributed to additional electrostatic effects due to the charged ligand and the consequent distribution of the ions within the double layer. Furthermore, binding affinities may change after immobilization of the ligand on the surface[90]. Generally, the observed or effective dissociation constant
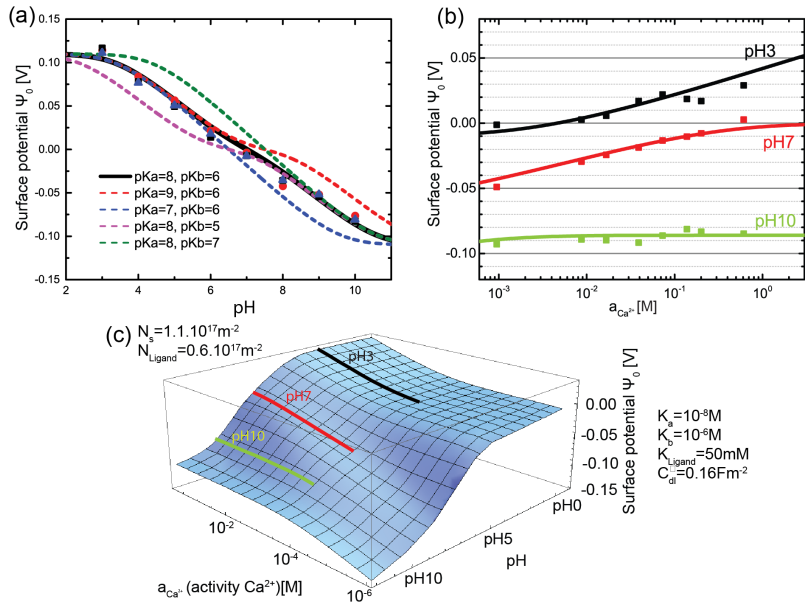
Figure 3.2: (a) Surface potential Ψ_0 versus pH with theoretical lines for different parameters (dashed lines) and the actual pH measurement of three control NWs (solid symbols). The measured threshold voltage V_{th} of each NW is converted to the surface potential as explained in the text. We find that a $pK_a = 8$ and $pK_b = 6$ and $N_s = 1.1 \cdot 10^{17}\,\text{m}^{-2}$ (solid line) gives good agreement with the data. (b) Surface potential Ψ_0 versus the activity of calcium ions of the electrolyte with theoretical fits (solid lines) and the sensor response (solid dots). The sensor response ΔV_{th} has been converted to the surface potential as explained in the text. From the fits we find $K_{Ligand} = 50\,\text{mM}$ and $N_{Ligand} = 0.6 \cdot 10^{17}\,\text{m}^{-2}$. (c) Theoretical plots of the surface potential Ψ_0 versus activity $a_{Ca^{2+}}$ and pH with $K_{a,b}$ and N_s obtained from the pH measurement. N_{Ligand}, K_{Ligand} were then determined from the actual measurements performed at pH 3, pH 7 and pH 10 (solid lines in the graph). Figures adapted from reference [63].

$K_{Ligand}^{effective} = K_{Ligande} e^{2e\Psi_0/kT}$ is highly dependent on the surface potential Ψ_0 as discussed in Section 1.3.2. To obtain the value of K_{Ligand} from a measurement, the absolute potential has to be known exactly. Using the model, we estimate the surface charge and therefore the surface potential by the well-known site-binding model for hydroxyl groups and the additional groups originating from the surface functionalization leading to the reported value of $K_{Ligand} = 50\,\mathrm{mM}$. Any additional charges at the surface originating from further surface reactions or other adsorption events will therefore drastically influence this value leading to a discrepancy of the extracted value and literature values.

We conclude this discussion with Figure 3.2c, showing the calculated surface potential versus the activity of calcium ions $a_{Ca^{2+}}$ and pH for the parameters obtained above. Clearly, the pH value determines both the total shift $\Delta\Psi_{total,a_{Ca^{2+}}}$ and the region of maximum response. At high pH, the surface potential is rather negatively charged which increases the activity of the calcium ions as given by the Boltzmann distribution. Hence, the response to Ca^{2+} saturates at lower concentrations compared to responses at lower pH. It is important to note that any additional surface charge is directly changing the range in which the species can be detected. This can be used to tune the region of maximum response of the sensor.

3.1.3 Conclusions

Using Ca^{2+}-sensitive receptor molecules on gold-coated nanowires, we demonstrate the influence of pH on the sensor response to calcium ions. The measured data is in good agreement with the model and a response of $20\,\mathrm{mV/dec}$ in the concentration range of $1\,\mathrm{mM}$ up to $1\,\mathrm{M}$ is achieved. We further demonstrate that the choice of material and functionalization is highly critical for the specific detection of species other than protons. Gold is a possible candidate in this case because of its moderate pH response and the well-established protocols for the self-assembly of monolayers of functional molecules.

3.2 1/f Noise in Gold-Coated Nanowire ISFETs

In the previous section we have discussed the parameters which have to be optimized to obtain a maximum response for the specific detection of ions other than protons. In particular the role of the top sensor layer was highlighted. However, the question of the resulting minimum detectable

change in analyte concentration remains open. As briefly discussed in Section 1.3, the answer requires the concept of noise. For a transistor, the noise determines the smallest detectable change in surface potential. To calculate the corresponding smallest detectable change in analyte concentration, the response has to be compared with the intrinsic noise of the transistor, expressed by the signal-to-noise ratio (SNR). We have shown in an earlier work that the noise of liquid-gated SiNWs is well-described by the trap state noise model, assuming trap states at the gate as the major source of noise[48]. Importantly, the model suggests that the SNR, given by Equation 1.41, scales with $\sqrt{WL}$ with W, L the width and length of the NW respectively. This relation was experimentally confirmed for NWs of widths ranging from $100\,\mathrm{nm}$ to $1\,\mu\mathrm{m}$. However, the influence of the interface between the sensing surface and the electrolyte has not been studied systematically. Specially the relation between the number of surface sites and the noise has not been investigated.

In the following, we address this issue by measuring the low-frequency $1/f$ noise for SiNWs with gate dielectrics of Al_2O_3 and HfO_2 with and without an additional gold coating in a pH 7 solution. Noise measurements with and without the gold film allow comparing the noise of the transistor for different N_s. Interestingly, we find no difference in the gate referred noise of the gold-coated NWs compared to their counterparts with bare oxide surfaces. Our results suggest that reducing N_s at the sensing surface does not increase the SNR. This finding is in agreement with the trap state noise model which assumes that the noise origins from trap states at the silicon/oxide interface expressed by the density of trap states N_{ot}. The parameter N_{ot} does not depend on the surface functionalization at the electrolyte/sensor interface. This finding is further supported by noise measurements of gold-coated NWs functionalized with a monolayer of sodium-sensitive molecules. Also in the presence of these additional surface groups, the noise does not change significantly. Our measurements suggest that changing the functionality of the ISFET does not change the noise of the sensor. Therefor, our proposed gold-based functionalization scheme is a valid method to achieve selectivity and to increase the response to a targeted species. Interestingly, our findings are in contrast to a recent work by Rajan et al.[70] where changing N_s of a SiO_2 surface of similar structures decreased the noise significantly. We will address this point in more detail in the conclusion.

3.2.1 Materials and Methods

Noise Measurements   Figure 3.3a shows the schematic of three NWs together with the measurement setup. In this section, we consider two different device chips either with 20 nm-thick Al_2O_3 or 20 nm-thick HfO_2 as gate oxide. For both samples, 24 of the 48 NWs are covered by the additional gold layer. This results in four different types of NW surfaces: Bare Al_2O_3, gold-coated Al_2O_3, bare HfO_2 and gold-coated HfO_2. The layout of the two samples consists of both 1 μm and 25 μm-wide NWs and therefore each gate oxide, with and without the gold layer, is available on 1 μm as well as 25 μm-wide wires.

To measure the noise, we apply a constant source-drain voltage $V_{sd} = 100$ mV to the drain contact. The fluctuations of the source-drain current $I_{sd}(t)$ are amplified by an I-V converter (in-house produced) connected to a DAQ board (*National Instruments*) resulting in $V_{out}(t)$. $I_{sd}(t)$ can be related to the measured voltage at the output of the I-V converter $V_{out}(t)$ via $I_{sd}(t) = V_{out}(t)/Gain$. The liquid-gate voltage V_{ref} is applied to a Ag/AgCl reference electrode. The potential of the handle wafer has been set to ground for all measurements of this work ($V_{bg} = 0$ V). The time-dependent source-drain current $I_{sd}(t)$ was transformed to a noise spectrum $S_{Isd}(f)$ via fast Fourier transform. For the noise measurements, the liquid cell shown in Figure 1.11a was used to minimize potential fluctuations from air bubbles. The SiNWs were gated in a buffered solution of pH 7.

3.2.2 Results and Discussion

Figure 3.3b shows the conductance G and the transconductance g_m versus the liquid-gate potential V_{ref} for a 1 μm-wide NW with bare Al_2O_3 surface. Since the silicon channel is p-type, the conductance increases for decreasing voltages starting at the subthreshold regime, increasing over the linear regime and starts to saturate in the contact dominated regime for even higher negative gate voltages. To achieve the specific detection of ions other than protons, the surface needs to be functionalized such that only the targeted species get adsorbed. We use the molecule schematized in Figure 3.3c consisting of a 15-crown-5 ether receptor and a dithiol anchoring moiety to immobilize the molecule on a gold surface. The crown ether is known to have high affinity to sodium ions as presented in Section 2.1. Repeating the procedure of Section 2.1, we use individual channels in a microfluidic liquid cell to functionalize only one half of the sample with the molecules, while leaving the rest untreated. This results in a differential setup, having
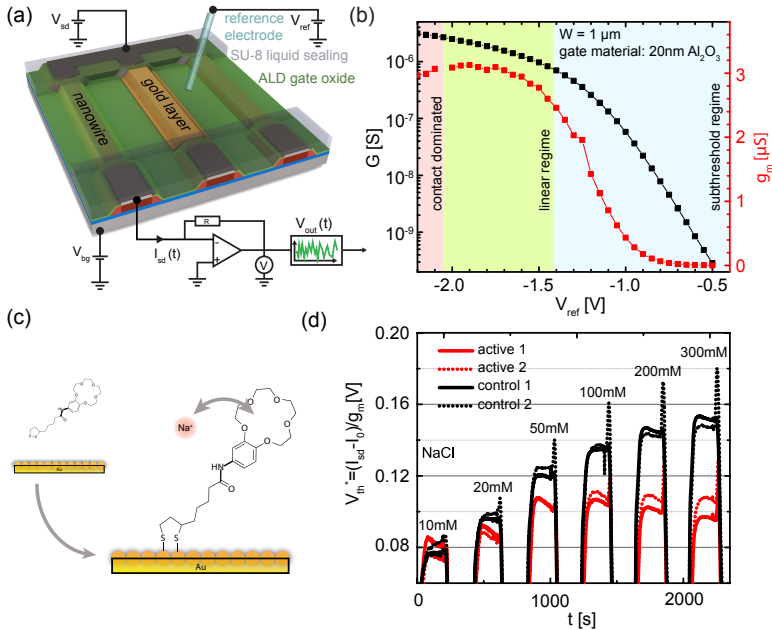
Figure 3.3: (a) Device schematic and measurement setup exemplified for three NWs. (b) Conductance G (black, left axis) and transconductance g_m (red, right axis) versus liquid-gate potential V_{ref} for a $1\,\mu$m-wide NW with Al_2O_3 surface. (c) Surface modification for the detection of sodium ions (Na^+). First, the gate oxide of the NW is covered by a thin gold layer ($20\,$nm). Then, the gold surface acts as platform for the functionalization with self-assembled monolayers of sodium-sensitive molecules (15-crown-5). (d) Time-dependent measurement showing V_{th}^* versus time t for two functionalized NWs (active) and two NWs with bare gold surface (control). The crown ether binds sodium ions Na^+ which decreases V_{th}^*. Switching the valve introduces additional noise, observed as spikes in the time-dependent measurement.

both functionalized NWs (active) and NWs with bare gold surface (control) on the same sample.

Figure 3.3d shows the time-dependent measurement of the quasi-threshold voltage V_{th}^* as introduced in Section 1.2.4 versus time t for increasing concentration of NaCl from 10 mM to 300 mM. To individually address several NWs, I_{sd} is switched between measurement points which introduces noise. Additional noise contributions are introduced when switching the valve, indicated by the spikes in Figure 3.3d. However, these noise sources do not exist in the noise setup, because for the noise, only an individual nanowire is measured at once and no liquid exchange is present. The clear difference between active and control NWs is attributed to the adsorption of sodium ions by the 15-crown-5 molecule. To better compare the different NWs, the quasi-threshold voltage is shifted for each wire by an offset I_0 as introduced in Section 1.2.4. Whereas the control NWs show a total shift in the threshold voltage of 70 mV due to unspecific response to changes in the electrolyte concentration, the active NWs show only a weak total shift of 20 mV. Taking the differential response $\Delta V_{th}^* = V_{th;active}^* - V_{th;control}^*$ reveals a total shift of 50 mV which results in a response of ≈ 35 mV/dec close to the value reported in Chapter 2.

Figure 3.4 shows the noise measurement of two 1 μm-wide NWs with HfO$_2$ as gate oxide. For Figure 3.4a and b, the oxide surface is in direct contact with the electrolyte, whereas in Figure 3.4c and d, the HfO$_2$ is covered with an additional gold layer. Figure 3.4a shows the conductance G (black, left axis) and transconductance g_m (red, right axis) versus liquid-gate potential V_{ref} measured with the I-V converter. Thereby, the time-dependent source-drain current $I_{sd}(t)$ was measured for 1 s with a sampling rate of 100 kHz and averaged over 100 samples. We calculate the average of $I_{sd}(t)$ resulting in $\overline{I_{sd}}$ and the conductance $G = \overline{I_{sd}}/V_{sd}$. The jump in conductance at a liquid-gate voltage of $V_{ref} = -1.0$ V is attributed to drift. The measurement was paused over night at $V_{ref} = -1.0$ V and continued the next day. The transconductance is calculated as the numerical derivative $d\overline{I_{sd}}/dV_{ref}$. The maximum transconductance is around 1 μS (at $V_{sd} = 100$ mV).

The measured current noise $S_{Isd}(f)$ can be related to the NW via the input referred voltage noise calculated by

$$S_V(f) = S_{Isd}(f)R^2 \qquad (3.4)$$

with $R = 1/G$ the resistance. Figure 3.4b shows the voltage noise S_V versus frequency f for different conductance values of the NW. Clearly, the noise decays with $1/f$, indicated by the black dashed line.
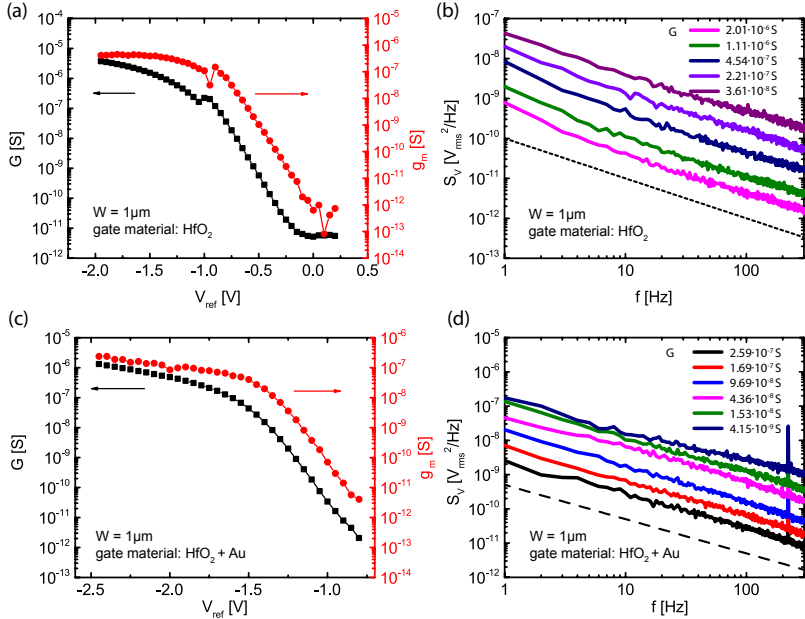
Figure 3.4: (a) Conductance G versus liquid-gate potential V_{ref} for a $1\,\mu$m-wide NW with HfO$_2$ surface. (b) Voltage noise S_V versus frequency f at different conductance values of the NW shown in (a). The noise of the NW shows clear $1/f$ characteristic (black dashed line). (c) G versus V_{ref} for a $1\,\mu$m-wide NW with HfO$_2$ as gate oxide covered with the additional gold layer. (d) S_V versus f at different conductance values of the NW shown in (c).

Figure 3.4c shows the conductance G (black squares, left axis) and transconductance g_m (red circles, right axis) versus liquid-gate potential V_{ref} for a $1\,\mu$m-wide NW with HfO_2 coated with the additional gold layer. As demonstrated previously, the transfer characteristic is very similar compared to NWs with bare oxide. However, the threshold voltage is shifted towards more negative values. Figure 3.4d shows the voltage noise S_V corresponding to the gold-coated NW. The measured noise is still of $1/f$ type.

To relate the measured noise to the minimum detectable change in surface potential we calculate the gate referred voltage noise

$$S_{Vg}(f = 10\,\text{Hz}) = \frac{S_{Isd}(f = 10\,\text{Hz})}{g_m^2} \qquad (3.5)$$

at $f = 10\,\text{Hz}$, as introduced in Section 1.3.3. In a recent work[48], we demon-
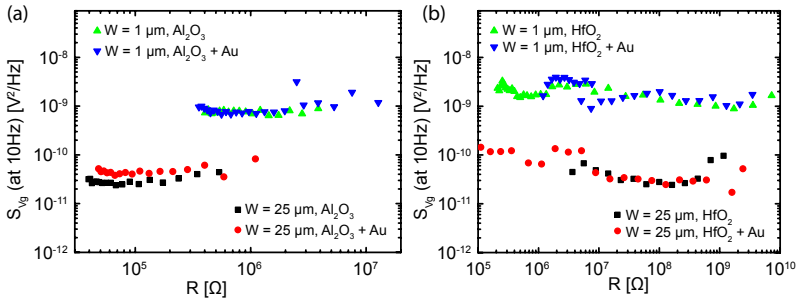

Figure 3.5: (a) Gate referred voltage noise S_{Vg} versus resistance R for $1\,\mu$m and $25\,\mu$m-wide NWs with gold and Al_2O_3 surfaces measured in pH 7 solution. In agreement with the trap state noise model, the noise decreases for the $25\,\mu$m NWs according to $S_{Vg} \propto 1/(W \cdot L)$. No significant influence of the additional gold layer is observed in the gate referred noise. (b) Gate referred voltage noise S_{Vg} versus resistance R for $1\,\mu$m-wide and $25\,\mu$m-wide NWs with gold and HfO_2 surfaces measured in pH 7 solution. Again, no significant difference is observed with the additional gold coating.

strate that in our devices, the gate referred voltage noise follows the trap state noise model briefly introduced in Section 1.3.3. Figure 3.5 shows S_{Vg} at 10 Hz for samples with bare and gold-coated NWs with Al_2O_3 (Figure 3.5a) and HfO_2 (Figure 3.5b) for both $1\,\mu$m and $25\,\mu$m-wide NWs. The figure shows three major findings: First, the gate referred voltage noise and therefore the SNR does not depend on the operation regime over a large range of resistance values suggesting that the noise is mainly generated at the gate. Second, as stated in Section 1.3.3, the noise is higher for the

$1\,\mu$m wires and scales with $1/(W \cdot L)$, in agreement with the trap state noise model [48]. This is also concluded by Rajan et al. [70] for nanowires of similar dimensions. Since the response and therefore the signal does not depend on the sensor area, to improve the SNR, one strategy is to enlarge the channel size. We find $S_{Vg} = 4 \cdot 10^{-11}\,\mathrm{V}^2/\mathrm{Hz}$ for the $25\,\mu$m-wide and $S_{Vg} = 1 \cdot 10^{-9}\,\mathrm{V}^2/\mathrm{Hz}$ for $1\,\mu$m-wide NW. In our previous work [48], we found $S_{Vg} = 1 \cdot 10^{-10}\,\mathrm{V}^2/\mathrm{Hz}$ for a $1\,\mu$m-wide NW with Al_2O_3, which is one order of magnitude lower. Batch-to-batch variations due to different production runs could explain this. Note that the value of $S_{Vg} = 1 \cdot 10^{-10}\,\mathrm{V}^2/\mathrm{Hz}$ leading to a trap state density of $N_{ot} = 2.5 \cdot 10^8\,\mathrm{cm}^{-2}$ is low compared to similar structures presented in literature [70]. Third, for both oxide surfaces, no systematic influence of the additional gold layer is visible in the gate referred noise. As shown in Chapter 2, the pH response of gold-coated NWs is substantially reduced to $30\,\mathrm{mV/pH}$ in contrast to the Nernstian response ($59.6\,\mathrm{mV/pH}$) observed for both underlying oxide surfaces (Al_2O_3 and HfO_2). Therefore, reducing N_s does not change the gate referred noise. This is in agreement with our assumption that trap states at the oxide/semiconductor interface act as major source of the noise [48]. Due to the difference in relative permittivity ($\epsilon_r \approx 5.5 - 10$ for Al_2O_3 [48] and $\epsilon_r \approx 14 - 18$ for HfO_2 [91]) a decreased S_{Vg} is expected for the nanowires with HfO_2 as gate oxide (Equation 1.40 with $C_{ox}^{\square} \propto \epsilon_r$). However, we find no clear difference in S_{Vg} when comparing the noise measured with the two oxide materials. This could be explained by an increased density of trap states for NWs with HfO_2 as gate material.
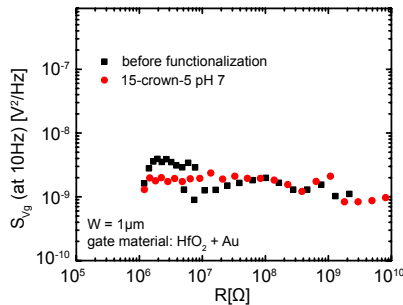

Figure 3.6: Gate referred voltage noise S_{Vg} versus resistance R for a gold-coated, $1\,\mu$m-wide NW before and after functionalization with sodium-sensitive 15-crown-5 molecules.

To further investigate the influence of surface modifications, we analyze the $1/f$ noise of nanowires covered with self-assembled monolayers of the 15-crown-5 molecules. In Figure 3.6 we compare the gate referred voltage noise of a $1\,\mu$m-wide gold-coated NW with a HfO_2 gate oxide before and after functionalization in pH 7. No substantial change in noise level is observed after the functionalization. Although the buffered solution of pH 7 contains approximately $30\,mM$ of NaCl, no noise contribution from the additional surface groups is observed. This is in agreement with our previous measurements comparing the noise of SiNWs gated in electrolytes of different composition[48].

Finally, the signal-to-noise ratio of gold-coated nanowires functionalized with ion-selective molecules can be calculated. For the 15-crown-5 molecule, a response of up to $\approx 40\,mV/dec$ in a NaCl solution in the range from $1\,mM$ to $1\,M$ has been demonstrated as discussed in Section 2.1. Therefore the SNR of a 1-order increase in concentration (e.g. from $c_1 = 1\,mM$ to $c_2 = 10\,mM$) is given by

$$SNR = \frac{\Delta\Psi_0}{\Delta\Psi_{0,min}} = \frac{\Delta\Psi_0}{\sqrt{S_{Vg}}} \approx 6300/\sqrt{Hz} \tag{3.6}$$

using $\Delta\Psi_0 = 40\,mV$ and $S_{Vg} = 4\cdot10^{-11}\,V^2/Hz$ for a $25\,\mu$m-wide NW. The equation of the SNR was introduced in Section 1.3. The corresponding limit of detection (LOD) is given by Equation 1.28. As discussed in Section 1.3, the LOD gets better at lower background concentration. In this example of the 15-crown-5 molecules, the lowest concentration investigated is at $c_1 = 1\,mM$ corresponding to $\log(c_1/c_0) = \log a_1 = -3$.[1] The corresponding LOD is given by $\log a_{2,min} = \Delta\Psi_{0,min}/response(\Delta\log a) + \log a_1 = -2.9998$ with $response(\Delta\log a) = 40\,mV/dec$. This results in $c_{2,min} \approx 1.00046\,mM$. In conclusion, an increase $\Delta c_{min} = c_{2,min} - c_1 = 460\,nM$ measured at $10\,Hz$ with bandwidth of $1\,Hz$ can theoretically be detected at $1\,mM$ background concentration with a $SNR = 1$.

3.2.3 Conclusion

In conclusion, we have studied the low-frequency $1/f$ noise of SiNWs with two different widths ($1\,\mu$m and $25\,\mu$m) with five different top layers (Al_2O_3, Al_2O_3 + Au, HfO_2, HfO_2 + Au, HfO_2 + Au + 15-crown-5). We found no indication that the properties of the sensing surface/electrolyte interface

---

[1]remember $c_0 = 1\,M$, Section 1.1.4

play a role for the noise: Neither the additional gold layer, nor the mono-layer functionalization change the gate referred voltage noise substantially. This is in agreement with the trap state noise model under the assumption that the noise is mainly caused by the trap states at the silicon/oxide interface. The additional surface binding groups, introduced by the functionalization, do not contribute to the noise. However, this is in contrast to a recent work by Rajan et al.[70] where a decreased gate referred noise is found in similar devices with SiO_2 as gate oxide after surface functionalization with (3-Aminopropyl)triethoxysilane (APTES). The exact influence of APTES on N_s is unclear, since no comparison of the pH response before and after functionalization is presented in reference[70]. However, the silanization process is expected to increase the number of surface hydroxyl groups N_s[3,5]. Interestingly, Rajan and co-workers find that the functionalization significantly decreases the gate referred voltage noise. This finding is explained by the suppression of charge trap states at the sensor/electrolyte interface. In fact, SiO_2 surfaces might hydrate substantially, leading to a certain permeability for small alkali ions such as sodium[20,41,73]. Their interaction with the gate oxide could lead to an additional noise contribution. APTES passivation might suppress these fluctuations, leading to a decreased noise. Since the hydration process is relatively slow, the process is possibly contributing to the low-frequency $1/f$ noise. Within the trap state noise model, the effect of surface passivation is observed as a decreased number of trap states N_{ot}. The described noise component is expected to be less pronounced for Al_2O_3 or HfO_2 gate dielectrics where no substantial hydration is expected[20].

To check this possibility, noise measurements at different ionic strengths are needed. Although we observe no influence of the analyte composition on the measured noise for Al_2O_3[48], the effect might be visible in the case of SiO_2. However, noise studies by Clément et al.[73] with SiNWs covered with high quality SiO_2 do not support this hypothesis and the origin of this discrepancy remains unclear. It is reasonable to assume that every interface within the ISFET gate structure (including the gate electrode) contributes to the gate referred noise. The dominant contribution could be dependent on the specific geometry and materials of the ISFET. For the nanowires studied in this thesis, the dominant noise source is identified as trap states at the silicon/oxide interface. Surface functionalization is a valid method to achieve selectivity and to increase the response to a targeted species without increasing the noise of the transistor.

3.3 Summary

The ideal sensor described in the introduction of this thesis does not exist in reality due to several limitations discussed in this chapter. Importantly, the specific responses to sodium, fluoride and calcium ions presented in this chapter and in Chapter 2 are still below the Nernstian limit. Compared to conventional membrane-based ISEs, this is a major drawback of the platform. We identify the material of the top layer of the sensor as a crucial component since it must suppress the pH response due to its competing effect. Gold might be a valuable step towards such a material but further efforts are needed to find an ideally inert material. Furthermore, the top material must allow different surface functionalizations to exhibit a flexible platform for the specific detection of the target analyte. Again, gold allows using well-established thiol-chemistry for the formation of stable SAMs of functional molecules. Improving the functionalization procedure should lead to a further increase of the density of the binding sites resulting in an enhanced response.

The transistor intrinsically sets an additional limit to the sensing performance due to the finite resolution of measuring changes in surface potential. As discussed in this chapter, the noise is not affected by the top material in our devices but is mainly determined by the trap state density at the Si/oxide interface. The noise figures might be improved by further process optimization to minimize the trap state density, e. g. by optimized cleaning procedures prior to the gate oxide deposition. Lastly, the limit of detection (with $SNR = 1$ at $f = 10\,\text{Hz}$ and $1\,\text{Hz}$ bandwidth) was calculated as $460\,\text{nM}$ at $1\,\text{mM}$ background concentration for $25\,\mu\text{m}$-wide gold-coated NWs functionalized with 15-crown-5 molecules for sodium detection. The promising results of ion detection with gold-coated SiNWs finally motivates expanding the sensing capabilities to biological species. This is discussed in the next chapter.

4

Label-Free FimH Protein Interaction Analysis

Detection and quantification of biological and chemical species are central to many areas of research in life sciences and healthcare, ranging from diagnosing diseases to discovery and screening of new drug molecules. Monitoring the binding affinities and kinetics of protein-ligand interactions is crucial in drug research. A real-time measurement of molecular interactions by a sensing device reveals the valuable information on binding affinities [92] and offers a useful tool for disease diagnosis [93], genetic screening [13] and drug discovery [8]. The search for new therapeutic candidates often requires screening of compound libraries. At present, the state of the art is surface plasmon resonance (SPR) [94]. However, the high throughput screening application of this technique is rather limited and cost-intensive.

The SiNW FETs studied in this thesis are an alternative method to measure protein-ligand interactions [79,95]. The direct transduction of the analyte-surface interaction into an electrical signal allows real-time and high-throughput detection of biomolecules. Immobilizing the ligand directly on the sensor surface allows highly specific, label-free detection [96,97]. In the past, it has been demonstrated that FET based biosensors (BioFETs) allow the detection of biomolecular interactions down to picomolar concentrations [3,45,97]. However, most of this research has been focused on reducing the limit of detection (LOD). So far, studies on quantifying the signals - specifically binding affinities and kinetic data - have primarily focused on DNA interaction [98] and biotin-streptavidin interactions [8]. However, the biotin-streptavidin binding is one of the strongest non-covalent interactions known in nature (its dissociation constant K_D is on the order

of $\approx 10^{-14}\,\mathrm{M}$)[99] and therefore its significance for interaction studies and benchmark for minimum LOD is questionable.

In this chapter, we demonstrate the real-time detection of a therapeutically relevant protein with gold-coated SiNWs. Clear concentration dependent signals were obtained upon protein injection. The simultaneous measurement of several SiNWs in active and control arrays increased the amount of data and allowed the comparison of different sensor dimensions. Our results are a proof of concept for the use of BioFETs for kinetic studies of protein-ligand binding. As analyte we have chosen the therapeutically relevant FimH lectin. Lectins are highly specific carbohydrate-binding proteins, that are involved in numerous physiological and pathophysiological processes, including cell-cell recognition, inflammation, immune response, cancer and pathogen tropism[100,101]. FimH is a bacterial lectin. Its expression is highly correlated with urinary tract infections (UTIs), for which *E. coli* expressing the FimH protein at the tip of their pili are the main causative agent. In the human urinary tract, FimH enables bacterial adhesion to the urothelium, which is the first step of the infection[102,103]. The molecular pharmacy group of Prof. B. Ernst at the *Pharmacenter* at the *University of Basel* has synthesized and evaluated high affinity FimH antagonists, demonstrating their therapeutic potential for the treatment of UTIs[104–107]. Since a crucial factor for the efficacy of a therapeutic agent is the half-life of the drug-receptor complex, kinetics of the binding process and equilibrium dissociation constants are of special interest. We show that BioFETs are potential candidates to compete with SPR, the state of the art method to study these parameters. The possibility for high integration, up-scaling and the low cost of the BioFET technology[108] are very attractive features from which diagnostics and drug discovery could benefit in the near future. This chapter has been prepared as a manuscript for submission.

4.1 Material and Methods

Surface Functionalization   Gold-coated SiNW samples with $1\,\mu\mathrm{m}$- and $25\,\mu\mathrm{m}$-wide NWs were rinsed with DI, cleaned in UV/ozone for $20\,\mathrm{min}$ and enclosed by the PDMS microchannel, separating the chip in active and control channels. The channels were then rinsed with ethanol for $\approx 30\,\mathrm{min}$.

1-step functionalization: The mannose ligand synthesized by G. Navarra from the group of Prof. B. Ernst was dissolved in ethanol ($2\,\mathrm{mM}$). The control channel was treated with lipoic acid dissolved in ethanol ($2\,\mathrm{mM}$).

The microchannels were flushed with $200\,\mu l$ of the respective solution, then $200\,\mu l$ were slowly injected over $\approx 15\,\text{h}$ using a syringe pump. After the functionalization, the channels were washed with ethanol before the PDMS microchannel was removed for the measurement.

2-step functionalization: SAM formation of 16-mercaptohexadecanoic acid (MHDA) ($2\,\text{mM}$ in ethanol) for $16\,\text{h}$ at 4°C and afterwards rinsed with ethanol. After surface activation with EDC and N-hydroxysuccinimide (NHS) for $\approx 30\,\text{min}$ the ligands were injected to the microchannels.

Protein and Buffer solution FimH carbohydrate recognition domain (FimH-CRD) with a thrombin cleavage site (Th) linked to a 6His tag (FimH-CRD-Th-6His, $18.6\,\text{kDa}$) was expressed in *E. coli* strain HM125 and purified by affinity chromatography as described previously [109,110]. The purified protein was dialyzed against $10\,\text{mM}$ HEPES (4-(2-hydroxyethyl)-1-piperazine ethanesulfonic acid) buffer pH 8. Protein concentrations ranging from $1 - 100\,\mu\text{g/ml}$ ($54\,\text{nM}$ - $2.7\,\mu\text{M}$) were used. An intermediate ionic strength was chosen to have a well buffered solution and a Debye length of $\geq 3\,\text{nm}$. The theoretical isoelectric point of the FimH protein is at pH 6.7, so the protein is negatively charged in pH 8 buffer solution. For the pH measurements in Figure 4.3 standard pH buffer solutions (*Titrisol, Merck*) were used.

Surface Regeneration Surface regeneration was accomplished by denaturing the structure of the analyte. Usually strong bases or acids as well as detergents are used to denature proteins. However, since pH also affects the surface potential of the gold-coated NWs, we chose concentrated urea ($6\,\text{M}$) as regeneration solution, since pH was similar to the running buffer.

Electric Measurements and Fluidic Setup PDMS microfluidic channels, with a flow through Ag/AgCl reference electrode embedded in the tubing, were used for well controlled liquid transport as introduced in Section 1.2.2 and shown in Figure 1.10. However, potential fluctuations from air bubbles limit the signal-to-noise ratio (SNR). Therefore the liquid cell shown in Figure 1.11a with $\approx 15\,\mu l$ volume and embedded Ag/AgCl reference electrode was used as an alternative to study the SNR. Measurements were performed at constant liquid flow and at a fixed working point, i.e. source-drain voltage $V_{sd} = 0.1\,\text{V}$, back-gate voltage $V_{bg} = 0\,\text{V}$ and constant liquid-gate voltage (V_{ref}) to operate the SiNWs in the linear regime.

Changes in surface potential (Ψ_0) upon analyte binding shift the threshold voltage (V_{th}) which changes I_{sd}. To study the time-dependent signals, we use the quasi-threshold voltage $V_{th}^* = (I_{sd} - I_0)/g_m$ introduced in Section 1.2.4, Equation 1.25. I_0 is used to shift the baseline of each concentration trace to zero and to compensate drift, as explained in the results section. Upon injection of analyte bulk concentration $[A]$ to the buffer solution, the total shift in surface potential is ideally given by

$$\Delta\Psi_0 = -\Delta V_{th}^* = -\frac{\Delta I_{sd}}{g_m} = \frac{q_A}{C_0^{\square}}[B]_0 \times \frac{[A]}{K_D + [A]}. \tag{4.1}$$

Here q_A is the electric charge given by an adsorbed analyte and $C_0^{\square}$ is the capacitive coupling (in $[F/m^2]$) between the charge of the analyte molecule within the double layer and the bulk solution. It is influenced by the double layer capacitance and hence dependent on the ionic strength of the buffer solution [35,54]. $[B]_0$ is the total number of surface bound ligands per unit area. The last term describes the ratio of surface bound analytes at equilibrium, given by the site-binding model [51,63]. K_D is the equilibrium dissociation constant, which describes the protein-ligand affinity. g_m can be determined by $I_{sd} - V_{ref}$ measurements of each SiNW or by applying gate steps in the time resolved measurement. Using this conversion introduced by Duan *et. al* [8] the signal is no longer a function of the FET performance and only depends on $\Delta\Psi_0$ induced by the analyte.

In Figure 4.1 a schematic cross section of the SiNW biosensor setup is shown. Proteins injected to the liquid system adsorb to the functional layer and change Ψ_0. Figure 4.1b shows the transfer curve $I_{sd}(V_{ref})$ of a $1\,\mu$m-wide gold-coated SiNW in pH 8 buffer solution. As discussed in Section 1.2.2, the p-type transistor is operated in accumulation mode. The transconductance is extracted from the linear regime.

The ligands used for the sensor surface functionalization for specific (active) and unspecific (control) protein adsorption are shown in Figure 4.2 and Figure 4.3. Two different methods were used. In a 2-step method the gold surface was first coated with a monolayer of 16-mercaptohexadecanoic acid (MHDA) and afterwards a high affinity mannoside was attached by amine coupling. Ethanolamine, which is uncharged at pH 8 was used as control. Additionally a 1-step method with disulfide bonds (Figure 4.3) for direct ligand immobilization on gold was used. We did not observe a difference in binding kinetics for the mannoside ligand using the two different functionalization methods. To exclude signals from background salt concentration the proteins were dialyzed.
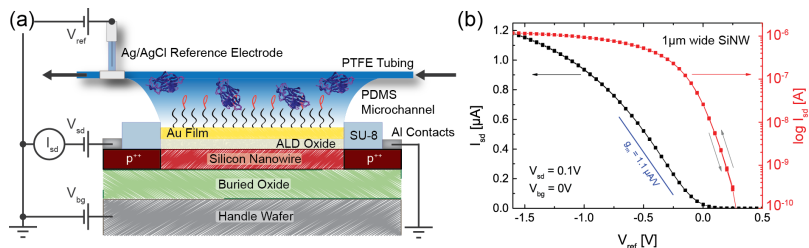
Figure 4.1: (a) Cross section of the fabricated device and a schematic of the silicon nanowire biosensor setup. The gold film, deposited on top of the HfO$_2$ gate oxide, is covered by a SAM of MHDA to which the ligands are attached by amine coupling. PDMS microchannels and PTFE tubings are used as fluidic system. A constant voltage $V_{sd} = 0.1$ V is applied across source and drain. The back-gate voltage V_{bg} is applied to the handle wafer (generally set to 0 V) and the liquid-gate voltage V_{ref} is applied to the reference electrode. FimH proteins in the solution bind to the ligands and thereby change the surface potential Ψ_0, which leads to a change in source-drain current I_{sd}. (b) Source-drain current (I_{sd}) versus liquid-gate potential (V_{ref}) for a 1 μm-wide gold-coated SiNW in pH 8 buffer solution. For the time resolved measurements the SiNWs are operated in the linear region where the transconductance g_m is constant as indicated by the blue line.

4.2 Results and Discussion

4.2.1 FimH Protein Detection

In Figure 4.2a the real-time sensor response of a SiNW with active mannose ligand for five different FimH concentrations in 10 mM HEPES buffer ranging from 5 μg/ml up to 100 μg/ml (1 μg/ml≈ 54 nM) is shown. Since the aim of affinity interaction studies is not to detect the analyte at physiological concentration, but to obtain and compare the affinity of antagonists, the concentration range was chosen to obtain kinetic data within acceptable measurement times. After each cycle, the surface was regenerated by flushing the system with 6 M urea for 10 min. At pH 8 FimH is negatively charged, leading to an increase in I_{sd} upon protein adsorption. Using a p-type semiconductor, $-\Delta\Psi_0 = V_{th}^*$ is plotted as a function of time. The straight line, obtained for the first 400 s prior to the binding event, was subtracted to avoid drift and to set the baseline to zero, corresponding to a time-dependent $I_0 = I_0(Time)$. Time= 0 s is defined as the onset of FimH adsorption. The response to FimH is clearly concentration dependent, but does not follow 1:1 Langmuir kinetics perfectly. In particular because the

slope of the association saturates at high protein concentration and no equilibrium is observed even after 15 min. The variation in dissociation for the $5\,\mu$g/ml signals (active and control) can be associated with a change in baseline drift.

Figure 4.2b shows the response of a control SiNW. A weaker signal is observed, which we attribute to nonspecific adsorption of FimH to the lipophilic layer of the MHDA functionalization.

Control experiments were performed with a commercial SPR-based biosensor (Biacore T200, *GE Healthcare, Uppsala, Sweden*). The response of a functionalized Au chip (active mannose ligand) is shown in Figure 4.2c. Although the same functionalization scheme was used, the signal in the Biacore shows different kinetics as compared to the BioFET. In particular, saturation starts at lower concentration and dissociation is less pronounced. A K_D of ≈ 5 nM is extracted by 1:1 Langmuir kinetic fits, indicated by the dashed lines.

The surface of the two different sensors is expected to be identical since the same surface functionalization was applied. Therefore, the dissociation constant K_D is expected to be the same. However, there is a clear difference in association and dissociation rates (k_a, k_d) using the two different systems. External factors such as flow speed can influence these rates. Mechanical force studies have shown that FimH-mediated bacterial adhesion depends on the flow rate[111,112]. Although, in our work FimH is dissolved in buffer and is not membrane bound, the flow speed at the sensor surface could be a cause of the difference in signal. Here we would like to mention that the outcome of affinity assays performed in commercial SPR systems vary for different users and strongly depend on equipment maintenance and operation[113,114]. However, at the same total flow rate ($26\,\mu$l/min), which was adjusted to be comparable to the SPR measurement ($20\,\mu$l/min), we did observe very similar binding kinetics using different flow geometries (microchannel Figure 4.2 and liquid cell Figure 4.3). On the contrary, at slow speed the transport of the analyte to the reaction site is becoming a limiting factor which strongly affects the binding kinetics. We have tested commonly used kinetic models, such as the two-compartment model for transport limited kinetics[8,115,116] to fit the BioFET data. However, they cannot explain the signals satisfactorily. As we generally expect similar kinetics and affinity of the protein-ligand interaction for both detection systems, different effects which could be the origin of the discrepancy in kinetics are discussed in the following.
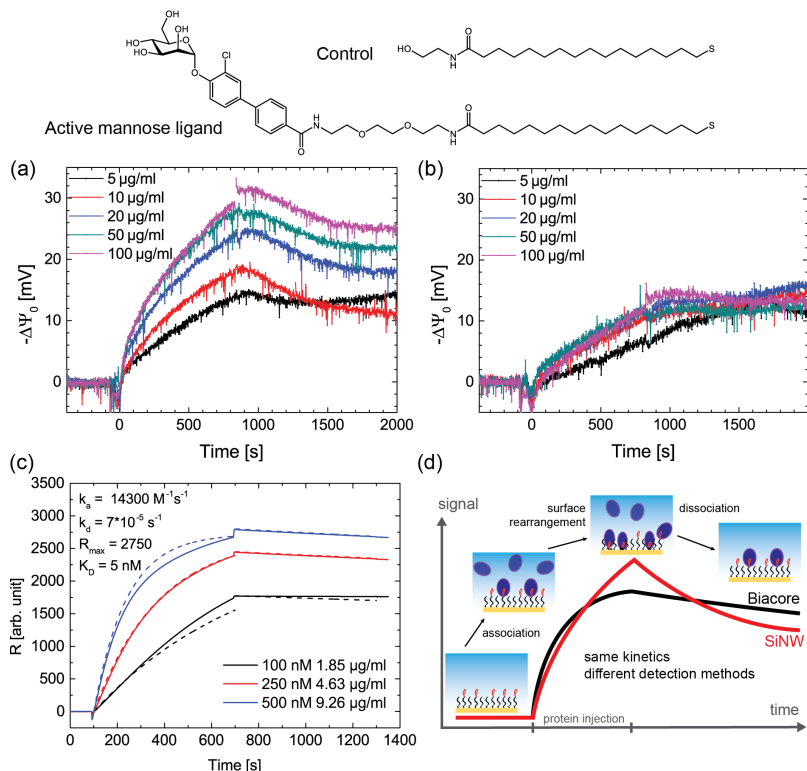
Figure 4.2: Real-time sensor response upon injection of FimH proteins at different concentrations. The microfluidic cell shown in Figure 1.10 was used. (a) Active SiNW shows pronounced concentration dependent protein adsorption and initial desorption upon rinsing with buffer after $900\,\mathrm{s}$. (b) Control SiNW shows nonspecific adsorption of FimH proteins, which we associate with the lipophilic character of the MHDA monolayer. (c) Reference experiment measured in the SPR system (Biacore T200) on a Au chip functionalized with the active mannose ligand. The signal starts to saturate already at smaller FimH concentrations and dissociation is less pronounced. 1:1 Langmuir kinetic fits are indicated by the dashed lines. An equilibrium dissociation constant of $K_D \approx 5\,\mathrm{nM}$ is obtained. (d) Schematic of a binding cycle comparing typical sensor responses of SiNWs and Biacore. Association of proteins to the surface ligands occurs upon FimH injection and dissociation upon switching to running buffer. Since a very similar surface on the SiNWs and the Biacore chip is expected, the binding kinetics should be similar. The difference in signal can be explained by the two different detection methods. Whereas the surface plasmon resonance detects larger molecules within $\geq 100\,\mathrm{nm}$ from the surface, the BioFET detects charges within $\leq 3\,\mathrm{nm}$ from the surface (at the used buffer concentration). We expect the adsorbed proteins to interact with the hydrophobic MHDA layer and move closer to the sensor surface. This surface rearrangement is a slow process and only affects the SiNW signal.

(I) The effective protein surface concentration   is considerably lower as initially injected. Using a flow rate of $26\,\mu l/min$ it takes $\approx 50\,s$ for the liquid to pass the liquid system and reach the SiNW surface. Proteins accumulate at the side walls and thereby the bulk concentration gets depleted. The materials in contact with the solution, PTFE, PDMS, SU-8 and HfO_2, are known to adsorb proteins [117–119]. With increasing side wall coverage this interaction diminishes and hence, bulk concentration increases with time. This would explain why no saturation is observed after $900\,s$. However, this effect can not explain the increased dissociation rate in the BioFET. Even if the concentration is taken as a free fitting parameter, an apparent affinity constant of $K_D \approx 300\,nM$ is found, which is two orders of magnitude higher than reported values of this particular protein-ligand interaction [110].

(II) Different sensing mechanisms   are used for the two systems. While the BioFETs sense charges localized within a few nm from the surface (characterized by the Debye length as introduced in Section 1.3.4), the SPR system measures the change in plasmon resonance frequency upon mass adsorption to the surface (change in refractive index). The depth of the evanescent wave is roughly two orders of magnitude larger as the Debye length [120], which results in a different sensitivity on analyte distance to the surface. Surface rearrangement [121] and surface induced conformational changes of adsorbed proteins [122] within a few Ångstroms affect the BioFET signal, whereas the influence on the SPR signal is marginal.

Figure 4.2d shows a scheme of a protein binding cycle and a qualitative picture of the difference in signal. As proteins bind to the surface the signal increases for both sensors until surface coverage has reached equilibrium. While the total amount of bound proteins stays constant, the SPR signal saturates. However, the BioFET is extremely sensitive to surface rearrangements, i.e. proteins approaching the SiNW at high surface coverage by a conformation change or interaction with the MHDA monolayer. We expect this process to be much slower than the protein-ligand association, which is why the signal does not saturate even if the numbers of proteins bound to the surface does not change. In addition the slope of the BioFET response saturates at very high protein concentrations. This indicates that the available binding sites are already occupied and the change in Ψ_0 has to have a different origin than the binding of additional proteins. The difference in dissociation can also be explained by this qualitative model, when proteins again undergo a rearrangement at the surface upon flushing with buffer.

We expect that both proposed effects influence the BioFET signals. How-

ever, an established model including microscopic surface rearrangement effects, which only become visible by using BioFETs, is still lacking.

4.2.2 Signal-to-Noise Ratio

For biosensors the limit of detection (LOD) is an important figure of merit. It is directly related to the SNR and ultimately limited by the protein-ligand affinity. As the electrical noise is intrinsic to the device quality and geometry [48,71], the signal strongly depends on the surface properties. As shown in Section 3.1 competing surface reactions of other species than the analyte can limit the sensitivity of the sensor. The competing adsorption reactions of the individual species are coupled via the surface potential. In the case of gold-coated BioFETs, the response to pH variations affects the signal of the FimH proteins. Only due to the very low pH response of the gold film we were able to detect clear signals from FimH adsorption.

In Figure 4.3a the pH response for gold-coated BioFETs functionalized with the active mannose ligand (1-step disulfide bond) is demonstrated. The threshold voltage is extracted from $I_{sd} - V_{ref}$ sweeps. Due to harsh surface treatments (cleaning and functionalization) between different measurements, the gold film on the SiNW surface was altered. We observed a gradual increase in pH response. We assume by using UV/ozone, organic solvents and a wide range of pH buffers the gold surface gets oxidized, leading to a variation in surface hydroxyl groups [63,83]. Since the FimH measurements were performed at pH 8, the pH range from pH 5 to 9 was of interest. The pH response (linear fit from pH 5 to pH 10) varies from ≈ 19 to $29\,\mathrm{mV/pH}$. Using the extended site-binding model introduced in Section 1.3.2 and 3.1 where the density of proton sensitive hydroxyl groups and FimH ligands are included (FimH concentration is set to $\approx 0\,\mathrm{M}$) the pH response of the functionalized gold surface can be fitted to extract the density of hydroxyl groups (N_s). We find that N_s changed by roughly a factor of two.

In Figure 4.3b the FimH response of the respective measurements are compared. For the increased N_s the FimH response was clearly reduced. The data supports the model of pH as competing surface reactions, which is exemplified in Figure 4.3c. It shows the theoretical response to a protein at a ligand density of $[\mathrm{B}]_0 = 3 \cdot 10^{16}\,\mathrm{m}^{-2}$ for two different N_s as a function of protein concentration. The curves denote the change in surface potential at equilibrium, calculated with the site-binding model including competing surface reactions as described in Appendix C, Equation C.2. The
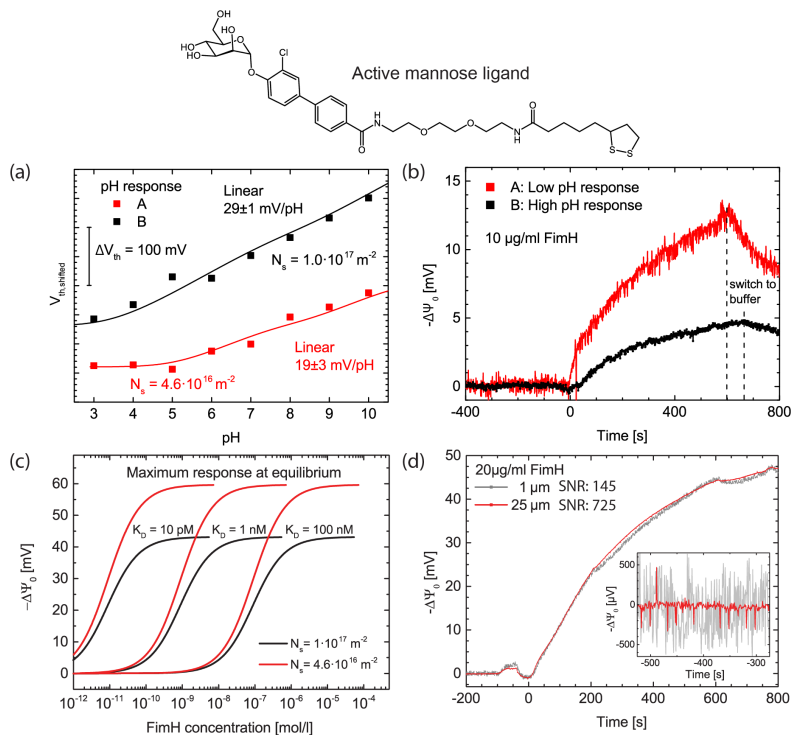
Figure 4.3: Competing surface reactions limit the signal. Measurements were obtained using the liquid cell shown in Figure 1.11a. (a) pH response (ΔV_{th} versus pH) for gold-coated SiNWs functionalized with the active mannose ligand shown on top. V_{th} is extracted from $I_{sd} - V_{ref}$ sweeps. The two different datasets show the same sample measured after different FimH measurement series. The lines correspond to the site-binding model (Equation C.2) at different hydroxyl group density N_s ($pK_a = 9$, $pK_b = 7$). Depending on N_s the linear response around pH 8 varies from $\approx 19\,\mathrm{mV/pH}$ to $29\,\mathrm{mV/pH}$. (b) Real-time sensor response for $10\,\mu g/ml$ FimH. The curves correspond to the same functionalized SiNWs as shown in (a). The response to FimH is clearly increased by roughly a factor of two when N_s is low. Increased noise is visible coming from voltage fluctuations induced by air bubbles. (c) Theoretical FimH response at equilibrium as a function of FimH concentration based on the site-binding model (eq. C.2) at two different hydroxyl group densities (N_s) for different protein-ligand interaction affinities (K_D). Based on pH and FimH measurements the following parameters were chosen: $[B]_0 = 3 \cdot 10^{16}\,\mathrm{m^{-2}}$, $N_s = 1 \cdot 10^{17}\,\mathrm{m^{-2}}$, $4.6 \cdot 10^{16}\,\mathrm{m^{-2}}$, $C_{dl} = 0.1\,\mathrm{Fm^{-2}}$, pH$= 8$ and $pK_a = 9$, $pK_b = 7$ and the visible net charge per protein $q_A = 2\,e$. (d) Signal-to-noise ratio for different wire widths. Surface potential in a real-time measurement for two different wires of $1\,\mu m$ and $25\,\mu m$ width the active mannose ligand. Both wires show the same signal upon injection of $20\,\mu g/ml$ FimH. The inset shows the RMS noise for the baseline which is equivalent to the standard deviation of the measurement points ($\sigma = \sqrt{\mathrm{variance}}$). $\sigma_{1\,\mu m} = 325\,\mu V$, $\sigma_{25\,\mu m} = 65\,\mu V$. The SNR is clearly increased for the larger sensor area (scales with $\sqrt{\mathrm{area}}$).

detectable concentration range predominantly depends on K_D, the affinity of the protein-ligand interaction (indicated by three example values). However, with increasing N_s the response to the protein decreases. Simultaneously the sensitive concentration range becomes narrower. In summary the FimH signal increases for a low pH response, where Figure 4.3b and c agree qualitatively. This holds for any ISFET system, where decreasing the number of surface sites of a competing reaction enhances the response to the targeted analyte. We assume both gold surfaces used for the SPR and SiNW measurements are comparable. However, the parameter N_s primarily affects the surface potential and only secondarily affects the binding kinetics. Though, as for SPR systems where the surface potential is not measured, the parameter N_s becomes negligible.

Using PDMS microchannels and remote liquid gating by placing the reference electrode in the tubing increases current fluctuations, caused by unstable gating due to moving air bubbles. To analyze the signal-to-noise ratio we reduced external noise, by using the larger liquid cell with the reference electrode included in the immediate vicinity of the wires, as shown in Figure 1.11. Figure 4.3d shows the response of two active SiNWs of two different areas ($6 \times 1\,\mu\text{m}^2$ and $6 \times 25\,\mu\text{m}^2$) upon injection of $20\,\mu\text{g/ml}$ FimH. The signal ($\Delta\Psi_0$) is the same for both sensor dimensions. However, the noise decreases with larger sensor area. The inset in Figure 4.3d shows the noise in the baseline of the two SiNWs. Instead of the gate referred noise, we use here the root mean square (RMS) noise, which is equivalent to the standard deviation of the measurement points ($\sigma = \sqrt{\text{variance}}$). The RMS noise is $325\,\mu\text{V}$ for the $1\,\mu\text{m}$ SiNW and $65\,\mu\text{V}$ for the $25\,\mu\text{m}$ SiNW. As shown in Section 3.2, the gate-referred voltage noise S_{VG} scales with $1/(W \cdot L)$, where W and L represent the silicon channel width and length. Further we showed that the sensor width has no influence on pH response [47]. For the SiNW dimensions presented here, the change in surface potential is independent of the sensor width since the total charge from adsorbed proteins is proportional to the area. Hence, the signal-to-noise ratio ($\frac{\Delta\Psi_0}{\sqrt{S_{VG}}}$) scales with $\sqrt{\text{area}}$, which is shown here as it increases from 145 for the $1\,\mu\text{m}$-wide SiNW to 725 for the $25\,\mu\text{m}$-wide SiNW.

4.3 Conclusion and Summary

We have successfully demonstrated the use of gold-coated SiNWs as biosensors by the detection of FimH, a therapeutically relevant protein with an important role in UTI. Real-time detection without labelling was achieved

at a very high signal-to-noise ratio of ≥ 700. The SNR is shown to increase
with $\sqrt{\text{area}}$ which is an important aspect for the design of a biosensor with
high device density. The use of gold as surface material has two tremen-
dous advantages as compared to oxides. First, the pH response is strongly
reduced which enables the detection of other species than protons. Second,
surface functionalization of gold has been extensively investigated which
simplifies the development of protocols for ligand immobilization on the
sensor and allows the direct comparison with SPR measurements. Being
able to observe association and dissociation is a first step towards the use
of BioFETs as affinity sensors. However, the accurate determination of the
protein binding affinity and kinetics remains challenging when comparing
the data with SPR measurements. This might be due to the enhanced sen-
sitivity of BioFETs to surface rearrangements which is potentially advan-
tageous for very local measurements of biochemical species. For successful
detection of proteins the screening limitations of the ionic environment, the
binding affinity of the targeted analyte, the intrinsic electrical noise, as well
as competing surface reactions have to be considered and finally the sen-
sor needs to be engineered accordingly. Our results propose that SiNW
BioFETs have a great potential to be used in disease diagnosis and drug
discovery. Based on the large scale integration of SiNW arrays at low cost
biosensing based on silicon nanowires offers a promising alternative to the
currently used methodologies.

Part II

Organic Electrochemical Transistors Based on PEDOT:PSS

5

Introduction

In Part I of this thesis, arrays of SiNW ISFETs have been studied as possible candidates for highly integrated solid-state biochemical sensors. This choice is motivated by a potentially low-cost fabrication in a CMOS-compatible process, high integration and easy electrical read-out. Besides the efforts of enabling Si-technology for biochemical sensing, the search for novel materials possibly succeeding silicon is pursued by research groups all over the world. Apart from graphene and carbon nanotubes[123], conductive polymers have gained a lot of interest[124]. When interfacing biology in typical biosensing applications, the material properties determine the bio-compatibility, a critical parameter for in vivo measurements. After the first demonstration of conducting polymers in the 1970's[125], the field of organic electronics has seen spectacular advances in the last decades, with the main driver being the organic light-emitting diodes, which are now produced on industrial scale[126]. Besides organic solar cells and organic field-effect transistors (OFETs) the development of biosensors and bioelectronics devices based on conducting polymers is constantly progressing[15,127]. Conducting polymers offer the advantage of low temperature solution-processing, the possibility to coat large and even flexible substrates and a unique mixed electronic-ionic conductivity[128]. The latter property is of particular interest for biochemical and electrophysiological sensing. Ion-exchange with the liquid environment lowers the impedance of the electrolyte/polymer interface, enhancing the signal transduction[3] compared to standard microelectrode arrays used in electrophysiology[129,130].

A device type which has been intensively studied for applications in aqueous media is the organic electrochemical transistor (OECT)[131]. OECTs make use of hydrated conducting polymers which can change their conduc-

tivity by reversibly exchanging ions with an electrolyte. The devices typically exhibit a high transconductance[132–134]. OECTs have been applied to enzymatic[135–137] and ion sensors[16], as well as used both in vitro[14,138] and in vivo[132,139] to monitor biological[140] and electrophysiological[141] processes. In particular their high bio-compatibility makes them very interesting candidates for biosensors.

During this PhD project, OECTs based on poly(3,4-ethylenedioxythiophene):polystyrene sulfonate (PEDOT:PSS) have been studied in a project in collaboration with Dr. M. Sessolo and Dr. H. J. Bolink from the *Instituto de Ciencia Molecular* of the *University of Valencia*. In particular the low-frequency $1/f$ noise has been studied and compared to the noise of our SiNW platform, as discussed in Chapter 6. First, the working principle of OECTs is discussed. Then, two different OECT fabrication processes are presented. The first approach developed at the *Department of Bioelectronics* at the *École Nationale Supérieur des Mines de Saint-Étienne* results in transistor channels of dimensions $5\,\mu$m x $5\,\mu$m (width x length) or larger. Most of the noise data presented in Chapter 6 is based on these devices. The second process was developed during the collaboration with the *University of Valencia* and allows reducing the size of the channel down to $400\,$nm x $1\,\mu$m. However, the resulting device performance suffers from material degradation during processing and leakage currents, as further discussed in Section 5.2.2.

5.1 Working Principle

The electrical conductivity of PEDOT:PSS is based on the "π-conjugated" PEDOT polymer shown in Figure 5.1a. The polymer backbone consists of alternating single and double carbon-carbon bonds. In a very simple picture, this configuration leads to delocalized electrons along the polymer chain facilitating electrical transport[142]. At room temperature, the PEDOT is a semiconductor (with a band gap $E_g \approx 1.6 - 1.7\,$eV)[143] and only few electrons have high enough energies to contribute to the current. Although the intrinsic electrical conductivity of PEDOT is low, it can be significantly increased by chemical doping. This is achieved by adding anions, in the system studied here PSS, which oxidizes PEDOT as described by

$$\text{PEDOT} + \text{PSS} \rightarrow \text{PEDOT}^+\text{PSS}^- \qquad (5.1)$$
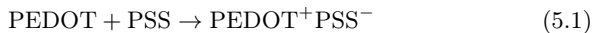
with PEDOT$^+$ the oxidized PEDOT and PSS$^-$ the reduced PSS[144]. Although PSS is a bad electrical conductor, it increases the conductivity of the

PEDOT:PSS complex drastically by creating holes in the PEDOT via the oxidation process suggested in Equation 5.1. In other words, the PSS acts as a doping agent (electron acceptor) creating a highly p-type doped semi-conductor with conductivities up to $4000\,\mathrm{S/cm}$[145]. Note that the proposed oxidation reaction does not occur for every PEDOT and PSS molecule. One hole generated every 3-4 molecules is commonly assumed[146]. In contrast to solid-state theory, the term doping in the context of conductive polymers refers to a chemical reaction (oxidation or reduction). The : used for the name of PEDOT:PSS refers to the fact that PEDOT is chemically doped with PSS and therefore refers to the righthand side of Equation 5.1. Importantly, the oxidized PEDOT^+ is only stable due to the PSS^- anion.

PEDOT:PSS forms a macroscopic salt where ionic bonds lead to the attachment of PEDOT strands to the PSS polymer as illustrated in Figure 5.1b. Besides the oxidation of the PEDOT, PSS also makes the complex water soluble which allows the deposition of thin films by spin-casting the solution on a substrate[147]. For the transistor operation, the possibility of modulating the charge carrier density is needed. White et al.[131] showed in the 1980's that reversible oxidation and reduction is possible with PE-DOT:PSS in contact with an electrolyte. This is achieved by adjusting the potential applied to a gate electrode immersed in the electrolyte solution.

In the following, small source-drain voltages ($V_{sd} < 0.2\,\mathrm{V}$) are assumed. For negative liquid-gate voltages $V_{ref} \leq 0\,\mathrm{V}$, the number of cations in the PEDOT is small, approximately given by the background electrolyte concentration. Under this assumption, the PEDOT remains mainly in its oxidized form, leading to a highly conductive channel (with a large conductivity σ) as depicted in Figure 5.1c. In other words, the transistor is a normally-on device. If a positive gate voltage is applied, metallic cations M^+ are forced into the polymer. Thereby the cations compensate the negatively charged sulfonate moieties on the PSS backbone. The additional cation M^+ stabilizes the PSS^- anion expressed by $\mathrm{M}^+\mathrm{PSS}^-$. If so, the oxidized PEDOT^+ is not stable anymore and is reduced via an electron e^- delivered from the source or drain contact and transported within the polymer. This is described phenomenologically by the following reaction:

$$\mathrm{PEDOT}^+\mathrm{PSS}^- + \mathrm{M}^+ + e^- \rightarrow \mathrm{PEDOT} + \mathrm{M}^+\mathrm{PSS}^- \tag{5.2}$$
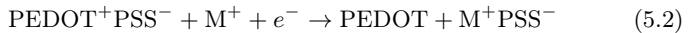
The process of de-doping is illustrated in Figure 5.1d. The reduced hole density results in a reduced conductivity. Thanks to the reversibility of this process, the conductive state can be controlled by injection of cations from the electrolyte into the polymer film using the reference electrode. Al-

though the configuration is similar to the setup of classical inorganic ISFETs presented in Part I of this thesis, the mechanisms responsible for the modulation of the charge carrier densities are very different. In literature, only a few reports describing the I-V and transfer characteristics of OECTs exist. Bernards et al.[148] divided the OECT into an electrical circuit consisting of a p-type organic semiconductor film and an ionic circuit which accounts for transport of ions between the electrolyte and the semiconductor. The resulting simple model is commonly used to describe the OECT behavior. For more information, the reader is referred to the original publication[148].
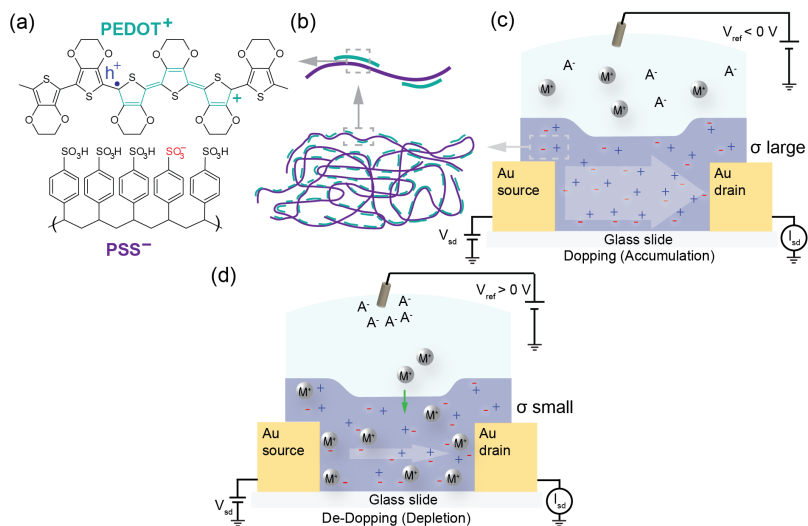

Figure 5.1: (a) Structural formula of PEDOT$^+$ and PSS$^-$ forming a macroscopic salt complex PEDOT:PSS. The oxidation of PEDOT via the PSS molecules stabilizes a hole h$^+$ in the PEDOT polymer backbone. (b) Schematic of the polymer structure with PEDOT segments ionically bound to long PSS chains. (c) Illustration of the PEDOT:PSS OECT gated in an electrolyte. Intrinsically, PSS-doped PEDOT has a high conductivity. (d) Illustration of the electrochemical de-doping process controlled by the gate voltage V_{ref} of the reference electrode. A$^-$ are the anions of the electrolyte.

5.2 Fabrication Processes and Characterization of OECTs

In collaboration with the *University of Valencia*, the $1/f$ noise of OECTs
was investigated. The results of this study are discussed in Chapter 6. The
measured devices were fabricated according to the process developed by M.
Sessolo and D. Khodagholy et al.[149] of the group of Prof. G. Malliaras at the
Department of Bioelectronics at the *École Nationale Supérieur des Mines
de Saint-Étienne.* The process allows the fabrication of PEDOT:PSS/Au
electrode and OECT arrays with channel dimensions from $5\,\mu$m to $250\,\mu$m.
A short description of the fabrication process is given in Section 5.2.1 for
reasons of completeness. For further details on the fabrication and device
characterization, the reader is referred to the literature[149]. Using these de-
vices the scaling of the noise with channel area from $25\,\mu$m^2 to $10000\,\mu$m^2
was investigated. To extend the noise study to even smaller channel geome-
tries, a new fabrication process based on e-beam lithography was established
in collaboration with M. Sessolo. The area of the channel was reduced to
$1\,\mu$m^2. A description of the process and the basic characterization of the
resulting devices are given in Section 5.2.2.

5.2.1 Fabrication Process of OECTs with Dimensions $\geq 5\,\mu$m

The fabrication process of state of the art PEDOT:PSS OECTs was re-
ported previously [7, 36]. The process results in an array of 36 OECTs with
channel width and length of 5, 10, 25, 50, 100 and $250\,\mu$m respectively. Fig-
ure 5.2a shows a cross section of a single OECT. The substrate is a simple
glass slide. The process begins by patterning source and drain contacts sep-
arated by a certain distance from each other. The distance between source
and drain contact defines the length of the PEDOT:PSS channel. The
width is defined by a two-step process using a sacrificial Parylene C (PaC)
layer. Thereby the contact structure is covered by a first, permanent PaC
layer and a second, sacrificial PaC layer on top. Lithographically defined
openings in the two layers determine the final dimensions of the channel.
The PaC layers act as a mask for the subsequent PEDOT:PSS spin coat-
ing. After spin coating, the sacrificial layer is peeled off which removes
all excess PEDOT:PSS material. The remaining PEDOT:PSS is located
only between the source and drain contacts. The remaining PaC layer is
used as a protection layer to prevent leakage from the electrolyte solution
to the gold leads. A more detailed description of the fabrication process
is given below. Figure 5.2b shows an optical micrograph of a part of the
array containing 6 OECTs with widths of $25\,\mu$m and $50\,\mu$m and lengths of

$25\,\mu m$, $50\,\mu m$ and $125\,\mu m$ after the fabrication. Figure 5.2c shows a zoomed micrograph of the $25\,\mu m$ by $50\,\mu m$ device. It shows the source and drain contact covered by the Parylene C layer with openings for the PEDOT:PSS transistor channel. While the openings define the width of the channel, the length is given by the spacing of the gold contacts.

In more detail, glass slides were cleaned using chemical and plasma methods and used as a substrate. To define the source and drain contact pattern, *Shipley 1813* photoresist was spin coated on the glass slide and exposed to UV light using a *SUSS MBJ4* contact aligner, and then developed using MF-26 developer. The contact layout defines the final length of the channel. A thin film composed by $5\,nm$ of Cr and $100\,nm$ of Au was thermally evaporated. After a lift-off in Acetone, the contact structures remain on the glass substrate. In the following, PEDOT:PSS transistor channels have to be defined exactly between the source and drain contact. Since the material can not be patterned directly by lithography, due to its incompatibility with many solvents and bases, a two-step process is used instead. First, a $2\,\mu m$ thick PaC layer was deposited using a *SCS Labcoater 2*. To ensure high mechanical stability of the first PaC layer, 3-(Trimethoxysilyl)propyl methacrylate was added into the chamber and used as an adhesion promoter for the first PaC coating. In the final device, the first PaC layer prevents leakage from the electrolyte to the gold contacts and acts thereby as a protection layer. Then, a second, sacrificial PaC layer is deposited on top of the first layer. However, prior to the deposition of the sacrificial layer, the protection layer is first spin coated with a dilute solution of industrial cleaner (Micro-90), acting as an antiadhesive for the second, sacrificial PaC film. The antiadhesive coating allows the removal of the sacrificial layer at the end of the process. Having the two PaC layers on top of the gold contacts, the layout of the transistor channel is aligned to the contact structures and transferred to AZ9260 photoresist by optical lithography. After developing in AZ developer (*AZ Electronic Materials*), the openings of the OECT channels were obtained by reactive ion etching with an O_2 plasma using an *Oxford 80 Plasmalab plus*.

The resulting structure consists of the gold contact pattern covered by the two PaC layers with openings. The openings define the width of the channels. For the preparation of the PEDOT:PSS films, $20\,ml$ of aqueous dispersion (*Clevios TM PH 1000 from Heraeus Holding GmbH*) were mixed with $1\,ml$ of ethylene glycol, $50\,\mu l$ of dodecyl benzene sulfonic acid, and $200\,\mu l$ of (3-glycidyloxypropyl)- trimethoxysilane, and the resulting dispersion was spin coated on the substrate. Thereby, the PEDOT:PSS solution flows into the openings of the PaC layers, but also covers the top, sacrificial

PaC layer. To remove this excess material, the sacrificial PaC layer was peeled off leaving behind the OECT array structure. Devices were subsequently annealed at $140\,^{\circ}$C for 1 h and then immersed in deionized water to remove any excess of low molecular weight compounds.
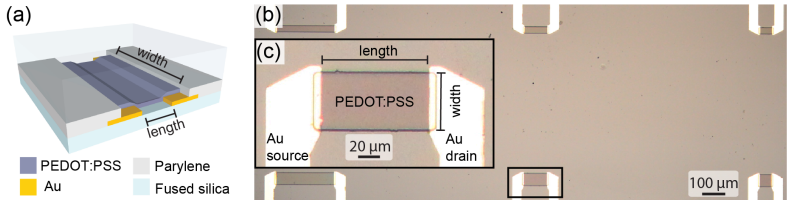

Figure 5.2: (a) Schematic of the cross section of the PEDOT:PSS OECT. (b) Optical micrograph of a part of the OECT array with 6 devices. The lower three devices have a width of $50\,\mu$m and upper devices a width of $25\,\mu$m. The length for both widths is given by $250\,\mu$m, $100\,\mu$m and $50\,\mu$m from left to right. (c) Zoom of the $50\,\mu$m × $100\,\mu$m device.

5.2.2 Fabrication and Characterization of OECTs with Dimensions $\leq 1\,\mu$m

Fabrication

To reach sub-μm dimensions, a novel process based on e-beam lithography was developed. As mentioned in the previous section, the fabrication process must minimize the exposure of the polymer to solvents or bases. Therefore, we use Si/SiO$_2$ wafers coated with PEDOT:PSS and evaporate a gold layer as etching mask for the PEDOT:PSS patterning. The device layout was adapted from the SiNW layout presented in Figure 1.8 and consists of 48 nanowires with widths of $2\,\mu$m. The width of the nanowire structure was further reduced to achieve structures with sub-μm dimension. After the patterning of the gold etching mask, the structure is transferred to the PEDOT:PSS by plasma etching. At the region of the final OECT devices, the top gold layer has to be removed in the final step. The fabrication process of OECTs with dimensions below $1\,\mu$m is illustrated in Figure 5.3a and is explained in detail in the following.

Si/SiO$_2$ (thickness SiO$_2$ $\approx$ $410\,$nm) wafers were cleaned in Acetone, Isopropanol (IPA) and rinsed with DI-water. For the preparation of PEDOT:PSS films, $20\,$ml of aqueous dispersion (*PH-1000 from Her-*
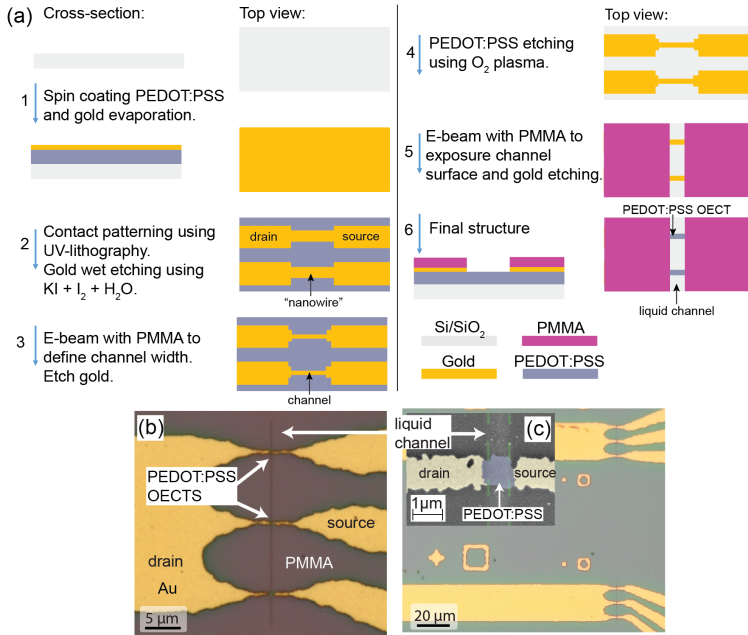
Figure 5.3: Fabrication process of PEDOT:PSS OECTs with dimensions $\leq 1\,\mu$m. (a) OECTS were fabricated on Si/SiO$_2$ wafers by spin coating of PEDOT:PSS and subsequent gold evaporation (1). Gold contacts were patterned using UV-lithography and etched via wet chemical etching in iodine/potassium iodide solution (2). E-beam lithography was used to define the channel width (3) and the PEDOT:PSS was etched using reactive ion etching in O$_2$ plasma (4). Finally, a liquid channel was defined via e-beam lithography to PMMA (5 and 6). (b) Optical micrograph of three OECTs. (c) SEM graph of a single device with dimensions of $1\,\mu$m $\times$ $1\,\mu$m. The liquid channel is aligned on top of the PEDOT channel.

aeous Clevios GmbH), 5 ml ethylene glycol, 250 µl (3-Glycidyloxypropyl) trimethoxysilane and dodecyl benzene sulphonic acid (*Sigma Aldrich*) were mixed and sonicated. Following the schematic of Figure 5.3a, PEDOT:PSS material was spin coated on the wafers at 4000 rpm for 40 s followed by a 30 min annealing step at 140 °C on the hotplate in step 1. The wafer was then covered by 50 nm of gold, deposited using e-beam evaporation. The gold layer acts as an etching mask and defines the source and drain contacts of the final device. To define the contact pattern, a former optical mask of the SiNW project was chosen for reasons of simplicity. In fact, we used the mask of the Si etching step, which results in the source and drain contacts connected by the nanowire. The layout was written in a negative photoresist (maN-415) by UV lithography and developed in maD332S developer and was transferred to the gold layer via wet chemical etching in aqueous solution of iodine/potassium iodide (concentration ≈ 1 mM). This results in the SiNW array structure with 4 arrays each consisting of 12 nanowires, similar to one presented in Section 1.2. Each array shares a common bus line, as introduced in Figure 1.8. Note that after the first gold etching of step 2, the Si/SiO_2 substrate is still covered by PEDOT:PSS including the part under the gold structure.

The final PEDOT:PSS transistors are located under the gold area which is structured as the nanowire (labeled by "nanowire" in Figure 5.3, step 2). At the nanowire region, the gold layer has to be finally removed to expose the PEDOT:PSS material to the electrolyte. Before, the nanowire width of $\approx 2 \, \mu m$ has to be further reduced. Therefore, a small constriction (width from 400 nm to $1 \, \mu m$) was defined using e-beam lithography in PMMA resist and developed in a 1:3 mixture of Methyl isobutyl ketone (MIBK) and IPA. The constrictions were applied to the structure by gold etching as described in step 2. This results in narrow constrictions as depicted in step 3 of Figure 5.3a. The narrow structures are named channels in the following. To transfer the channel structure to the PEDOT:PSS, the polymer is etched using O_2 plasma reactive ion etching (*Oxford Plasmalab 80*) at 160 W for 7 min using the gold layer as an etching mask (step 4). This results in channels of PEDOT:PSS covered with gold of the desired width. To define also the length of the transistor channel, a second e-beam lithography step opens a small liquid channel into the PMMA (step 5). The openings of the PMMA layer finally allow etching the gold on top of the channel using wet chemical etching in iodine/potassium iodide solution (step 6). The remaining PMMA layer was used as a protection layer to minimize leakage currents from the gate electrode to the source and drain contacts when measuring in a liquid environment. The resulting

array consists of 48 OECTs with dimensions ranging from approximately 400 nm x 400 nm to $1\,\mu$m x $1\,\mu$m. Figure 5.3b shows an optical micrograph of three OECTs resulting from the fabrication process described above. The three OECTs share a common drain contact. The liquid channel openings in the PMMA layer allow operation of the devices in liquid. Figure 5.3c shows the structure of six OECTs and a scanning electron microscopy (SEM) graph of the close up of the middle device as an inset. A brief electrical characterization of the resulting OECTs is given next.
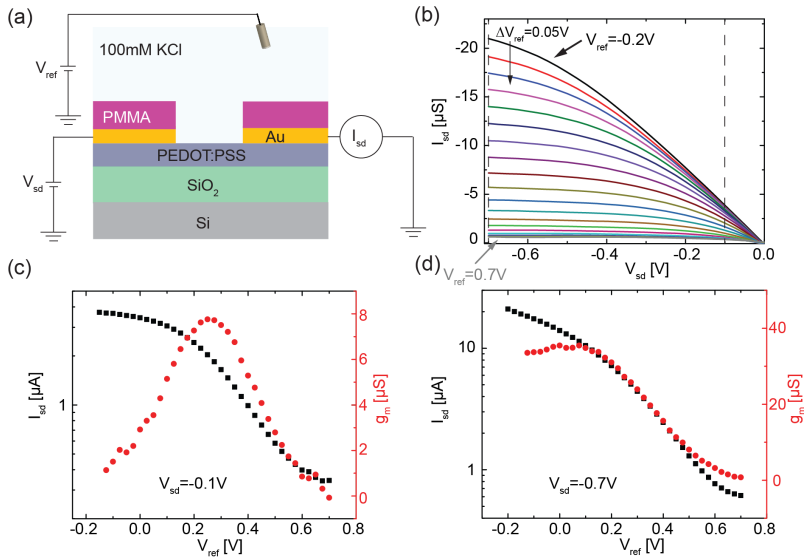
Basic Characterization

Figure 5.4: Measurement schematic and transistor characteristics. (a) A liquid-gate voltage V_{ref} is applied to the immersed reference electrode to gate the transistor to different conductance values. A constant source-drain voltage V_{sd} is applied and the source-drain current I_{sd} is measured. (b) I-V characteristic (I_{sd} versus V_{sd}). (c) Transfer characteristic at $V_{sd} = -0.1$ V. Source-drain current I_{sd} (black squares, left axis) and transconductance g_m (red circles, right axis) versus liquid-gate potential V_{ref}. (d) Transfer characteristic at $V_{sd} = -0.7$ V.

Figure 5.4a shows the measurement setup. A *Keithley 2636A* source meter is used to apply a source-drain voltage V_{sd} and to measure the source-

drain current I_{sd}. The gate potential V_{ref} is applied to a Ag/AgCl reference electrode immersed in the liquid. Figure 5.4b shows the I-V characteristic of the OECT shown in the inset of Figure 5.3c with dimensions of $1\,\mu$m x $1\,\mu$m. The source-drain current decreases for increasing positive gate voltage due to electrochemical de-doping process described in the previous section and studied by Bernards et al.[148] The resulting transfer curve is given in Figure 5.4c at $V_{sd} = -0.1\,$V. It shows the conductance G (black squares, left axis) and transconductance g_m (red dots, right axis) of the device. As discussed in Section 1.1.3, the transconductance scales ideally with V_{sd}. The normalized transconductance g_m^* is $\approx 80\,\mu$S/V (best case $\approx 100\,\mu$S/V) which is approximately an order of magnitude lower compared to state of the art OECTs of larger area fabricated using the process described in Section 5.2.1, as we will see in Chapter 6. The origin of this discrepancy might lie in the relatively high leakage currents observed for the nanoscale OECTs. The high leakage current is directly observed in Figure 5.4c at high positive gate voltage since depletion stops already at $I_{sd} \approx 0.2\,\mu$A. Therefore, I_{sd} is only modulated over 1-2 orders of magnitudes compared to 3-4 orders of magnitudes observed for state of the art OECTs[132]. Finally, Figure 5.4d shows the transfer curve at $V_{sd} = -0.7\,$V. The transconductance increases linearly with the source-drain voltage.

In conclusion, OECTs fabricated with the novel approach presented in this section show a transistor behavior. The normalized transconductance g_m^* was found $\approx 100\,\mu$S/V which is an order of magnitude lower than expected[132]. The transistor operation may also suffer from PEDOT:PSS degradation during the different fabrication steps. The chosen layout with the gold on top of the organic material leads to relatively high leakage currents from the gate electrode to the gold contacts. These leakage currents could be minimized by replacing the PMMA protection layer by a chemically more stable resist such as SU-8 similar to the SiNW arrays. Due to further device degradation during storage of the samples in ambient, only the noise data of the OECT shown in Figure 5.3c with channel area $\approx 1\,\mu$m^2 was obtained. The corresponding data is shown in Figure 6.3a together with the noise data of state of the art OECTs fabricated with the process described in Section 5.2.1.

5.3 Summary

This chapter introduced the working principle of OECTs and discussed two different fabrication protocols. State of the art OECTs are fabricated using

the process described in Section 5.2.1. The smallest dimension obtained with this process is $5\,\mu$m. To further reduce the channel dimensions, the process presented in Section 5.2.2 was established. However, the resulting OECTs did not show transfer characteristics comparable to the state of the art devices possibly due to material degradation during the process and leakage currents from the gate electrode to the contacts. Therefore, mostly state of the art OECTs with larger dimensions were used for the noise study presented in the following chapter.

6

1/f Noise of PEDOT:PSS Organic Electrochemical Transistors

As discussed in Section 1.3.3, noise is a key parameter of a sensor and was investigated in Section 3.2 for SiNWs. The low-frequency noise has also been studied for other biosensors based on liquid-gated graphene[150] and single-walled carbon nanotube (SWCNTs) transistors[151]. In the field of OECTs, noise has been mostly ignored. This is surprising since the noise allows comparing different materials regarding their potential for sensing applications and determines the resolution of the device.

In this section, we compensate this lack of knowledge by investigating the low-frequency noise of PEDOT:PSS OECTs introduced in the previous chapter. We present the noise scaling behavior with gate voltage, channel dimensions and polymer thickness. We demonstrate that the noise does not follow the α-noise model (introduced in Section 1.3.3), which assumes homogenous noise generation within the sample. Instead, the noise follows the charge-noise model (formally similar to the trap state noise model of Section 1.3.3), which depends only on the area of the channel rather than on its volume. In fact, we show that the noise scales with 1/area. These results suggest the use of large area PEDOT:PSS in order to maximize the signal-to-noise ratio (SNR) for biochemical and electrostatic sensing applications. Comparison with literature and our SiNW platform shows that the magnitude of the noise in PEDOT:PSS- based OECTs is similar to that observed in graphene transistors, but higher compared to SWCNTs and our SiNW devices. This chapter has been prepared as a manuscript for submission.

6.1 Methods

Device Fabrication   Arrays of PEDOT:PSS OECTs with channel dimensions (width x length) ranging from $5\,\mu$m x $5\,\mu$m to $250\,\mu$m x $250\,\mu$m and constant thickness $d = 110$ nm were fabricated based on the protocol presented in Section 5.2.1. Using the process presented in Section 5.2.2, a few noise data points were additionally achieved for an OECT with area $\approx 1\,\mu$m^2.

Noise Setup   Figure 6.1a depicts the device layout and the noise measurement setup. A liquid-gate voltage V_{ref} is applied to a Ag/AgCl reference electrode immersed in a 100 mM KCl aqueous solution to adjust the conductance of the PEDOT:PSS channel. Throughout this work, a constant source-drain voltage $V_{sd} = 100$ mV is applied to bias the transistor. At each gate potential, the time-dependent source-drain current $I_{sd}(t)$ is measured. The current fluctuations of $I_{sd}(t)$ are converted to voltage fluctuations by a current-voltage amplifier with variable gain from -10^5 to -10^9 V/A and measured using a National Instrument DAQ board. The time-dependent voltage fluctuations were converted to a noise power spectral density via fast Fourier transform using National Instrument Labview software. As a result, the fluctuations of the current $I_{sd}(t)$ are transformed into a noise power spectral density $S_{Isd}(f)$. $S_{Isd}(f)$ is referred to as current noise in the following.
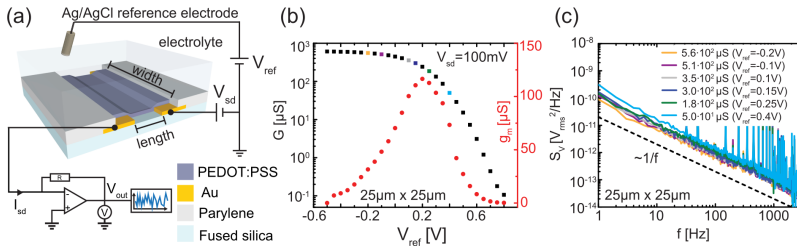

Figure 6.1: (a) Device schematic and measurement setup of the noise characterization. (b) Conductance G (black, left axis) and transconductance g_m (red, right axis) versus liquid-gate potential V_{ref} measured for a $25\,\mu$m (width) x $25\,\mu$m (length) OECT. (c) Power spectral density of the voltage fluctuations S_V versus frequency f. The black dashed line indicates the $1/f$ dependence.

6.2 Results and Discussion

Figure 6.1b shows a typical transfer curve of a $25\,\mu$m x $25\,\mu$m OECT fabricated using the process described in Section 5.2.1. The PEDOT:PSS film is highly conductive at zero applied gate voltage ($V_{ref} = 0\,$V) due to the intrinsic doping by PSS[133]. With increasing positive V_{ref}, potassium cations K^+ from the electrolyte enter the organic film partially compensating the pendant sulphonate anions of the PSS, effectively decreasing the conductance as described in the previous chapter. The maximum transconductance is $g_m \approx 120\,\mu$S at $V_{sd} = 100\,$mV; if normalized with the source-drain voltage, this yields a value in the order of $g_m^* \approx 1\,$mS/V, as observed for state of the art OECTs[132]. For each gate potential applied, the current noise $S_{Isd}(f)$ is recorded. Hence, from the measured current noise, the corresponding voltage noise power spectral density can be calculated via $S_V(f) = S_{Isd}(f) \cdot R^2$ with $R = 1/G$ the channel resistance. $S_V(f)$ is the voltage noise at the source-drain contacts if the transistor was current biased and is commonly used to compare the noise of a transistor adjusted to different resistance values via the gate[48,67,68,152]. Figure 6.1c shows the voltage noise $S_V(f)$ of the $25\,\mu$m x $25\,\mu$m channel transistor for 6 different gate voltages. The spectrum shows a clear $1/f$ characteristic, indicating that no process taking place at a specific timescale dominates[67]. It is commonly accepted that $1/f$ noise is caused by resistance fluctuations, and hence it should scale with bias squared: $S_V \propto V_{sd}^2$ and $S_{Isd} \propto I_{sd}^2$[66,153]. This bias dependence is observed in our OECTs (see Appendix D) confirming that the investigated noise is also caused by resistance fluctuations.

As introduced in Section 1.3.3, $1/f$ noise follows Hooge's empirical law $S_V/V_{sd}^2 = S_{Isd}/I_{sd}^2 = \alpha/(f \cdot N)$, with α the dimensionless Hooge's constant and N the number of fluctuators[66]. We use the α-noise model as a possible model for the noise of OECTs. It is given by Equation 1.37 and assumes that the noise is generated by mobility fluctuations distributed homogeneously within the sample volume[67]:

$$\frac{S_{Isd}}{I_{sd}^2} = \frac{\alpha e \mu V_{sd}}{f I_{sd} L^2} \qquad (6.1)$$

with e the elementary charge and μ the hole mobility, W, L and d the OECT channel width, length and thickness.

For a constant source-drain voltage, the α-noise model predicts $S_{Isd}/I_{sd}^2 \propto 1/I_{sd}$ as shown by the green line in Figure 6.2. Clearly, the α-noise model cannot explain our data and hence mobility fluctuations can be excluded as the origin of the noise in OECTs.
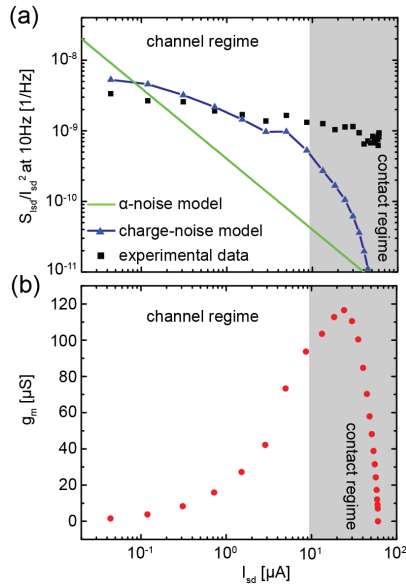
Figure 6.2: (a) Normalized source-drain current noise S_{Isd}/I_{sd}^2 versus source-drain current I_{sd} at $10\,\text{Hz}$ of the $25\,\mu\text{m} \times 25\,\mu\text{m}$ OECT biased at $V_{sd} = 100\,\text{mV}$ (black symbols). The green solid line shows the prediction following from the α-noise model. The blue triangular symbols are calculated using the charge-noise model which fits the experimental data well up to $I_{sd} = 9\,\mu\text{A}$. For larger source-drain currents, the noise deviates from the charge-noise model due to additional contributions from the contacts (contact regime). (b) Transconductance g_m versus source-drain current I_{sd}.

As alternative to the α-noise model we applied the charge-noise model[154] shown as the blue fit line in Figure 6.2. This model relates the current noise with the gate referred voltage noise S_{Vg} through the transistor transconductance $S_{Isd} = g_m^2 \cdot S_{Vg}$[48,70,155] similar to the trap state noise model introduced in Section 1.3.3. The gate referred voltage noise allows the direct comparison of the noise with the signal of the gate voltage thereby yielding the signal-to-noise ratio $SNR = \Delta V_{lg}/\sqrt{S_{Vg}}$[95]. The charge-noise model was successfully applied to describe $1/f$ noise measured for liquid-gated SWCNTs[151,156] and single/bilayer graphene[150,157] where the channel material is in direct contact with the electrolyte[68,132]. Two main noise sources were suggested: For substrate-bound SWCNT[151,156] and graphene[150] devices, the dominant noise source was identified as charge fluctuations in the substrate. For suspended carbon nanotubes (CNTs)[151] and graphene devices[157] charge fluctuations due to the Brownian motion of ions of the electrolyte were identified as the origin of the noise. As introduced in Section 1.3.3 and further discussed in Section 3.2, also the $1/f$ noise measured in liquid-gated SiNWs follows the charge-noise model where the noise source is associated with either trapping/de-trapping at the silicon/oxide interface[48] or fluctuations of the ions in the electrolyte[70].

Independent of the exact noise source, the charge-noise model assumes a charge noise spectral power density $S_q(f)$ in close proximity to the transport material which couples with an effective gate capacitance C_{gate} to the device, thereby modulating the carrier density. The fluctuating quantity is not the mobility as in the case of the α-noise model but the number of charge carriers. This is expressed by

$$\frac{S_{Isd}(f)}{I_{sd}^2} = \frac{g_m^2 \cdot S_{Vg}(f)}{I_{sd}^2} = \frac{g_m^2}{I_{sd}^2}\frac{S_q(f)}{C_{gate}^2}. \tag{6.2}$$

Measured at a specific frequency, both S_q and C_{gate} are constant for a device with given geometry, therefore $S_{Vg} = S_q/C_{gate}^2$ is also constant[150,154]. Consequently, the charge-noise model predicts $S_{Isd}/I_{sd}^2 \propto g_m^2/I_{sd}^2$. As shown in Figure 6.2, the charge-noise model (blue fit) agrees well with the experimental data for sufficiently small source-drain currents. In this regime, the transistor behavior is fully determined by the properties of the PEDOT:PSS channel, while the influence of the contact resistance is negligible. In the following, we will refer to this regime as the channel regime, as indicated in Figure 6.2. The deviation from the model at high source-drain currents is an expected transition from the channel regime to the contact regime highlighted by the grey shaded area in Figure 6.2. In the contact regime, the electrode contacts start to contribute significantly to the noise

because the resistance of the PEDOT:PSS channel becomes smaller than the contact resistance. The transition between the two regimes can be observed near the maximum of the transconductance g_m shown in Figure 6.2b, as described previously [48].

As proposed by Tersoff and Heller et al. the contact noise can be included by adding a noise contribution from a gate-independent series resistance [150,154]. However, we will not further investigate the contact regime in the following because we will show that the best (lowest) noise is only achieved in the channel regime. Furthermore, to compare different channel materials we use the value of the gate referred voltage noise which is only constant in the channel regime as we will show in the following. Our measurements suggest that the low-frequency $1/f$ noise in OECTs is due to fluctuations in the number of charge carriers as proposed by the charge-noise model. Interestingly, this is also observed in graphene and CNTs transistors. However, in strong contrast to these devices where a well-defined, sharp interface exists between electrolyte and active material, in OECTs, the electrolyte penetrates into the conducting polymer channel. This unique property raises the question about the origin of the noise in OECTs. We will address this point by determining the scaling of the noise with area and thickness of the channel in the following.

Figure 6.3a shows the gate referred voltage noise S_{Vg} versus resistance R for devices with varying channel width and length but constant film thickness ($d = 110$ nm). We find S_{Vg} to be independent of the resistance value as long as the transistor is operated in the channel regime, in agreement with the charge-noise model. As soon as the contacts also contribute to the noise, at low resistance values, the gate referred noise increases drastically as observed in Figure 6.3a. As the contact resistance is expected to scale with the inverse channel width W, the contact regime shifts towards lower resistance on the horizontal axis for increasing W, as highlighted by the grey area. We observe that the gate referred voltage noise decreases for increasing channel area indicated by the horizontal lines in Figure 6.3a.

We further investigated the scaling of the noise with channel volume, measuring samples with two different thicknesses of $d^{thin} \approx 60$ nm and $d^{thick} \approx 800$ nm but same width and length (5 μm and 100 μm, respectively). Figure 6.3b shows the gate referred voltage noise S_{Vg} versus resistance R for the two types of devices. As expected from the device geometry, the thick sample exhibits both lower channel and lower contact resistance. Therefore, we find a lower noise for the thick PEDOT:PSS in the contact regime. When operating the transistor in accumulation, thick OECTs are

preferred in agreement with a recent publication by Rivnay et al. [134] However, in the channel regime we observe no significant difference in noise for the two thicknesses. It means that for achieving the best SNR, thin OECT are as good as their thicker counterparts.

The observed dependence of S_{Vg} on the channel area but not on the channel thickness needs further discussion. Since $S_{Vg} = S_q/C_{gate}^2$, the scaling of S_{Vg} with geometry depends on the corresponding scaling of the charge noise S_q and the gate capacitance C_{gate}. Our experimental data could be explained by assuming that both C_{gate} and S_q scale only with area leading to $S_{Vg} \propto 1/WL$ as it is commonly accepted for liquid-gated CNTs and graphene transistors [150,151,155–157]. However, the absence of a clear interface between the polymer channel and the electrolyte might lead to a different geometry scaling of S_{Vg}. In particular, it has recently been demonstrated that the gating process of PEDOT:PSS OECTs involves the whole channel volume due to the ionic permeability of the polymer. Therefore both transconductance and effective gate capacitance depend on the channel thickness leading to $g_m \propto Wd/L$ and $C_{gate} \propto WLd$ [133]. The ionic permeability and volumetric gating behavior unique to OECTs could also result in a volume-dependent noise source $S_q \propto WLd$. In this picture, the noise originates from doping/de-doping processes within the bulk of the material where the Brownian motion of cations leads to $S_q(f) = S_q^* \cdot WLd/f$ with S_q^* the noise power density per volume. The charge-noise S_q couples to the active material via the volume-dependent gate capacitance C_{gate} which leads to the observed gate referred voltage noise S_{Vg}. In this case $S_{Vg} \propto 1/WLd$ is expected.

This proposed scaling with the inverse of the thickness d is not observed in Figure 6.3b. However, we would like to stress that the two devices with different thickness shown in Figure 6.3b originate from two different production runs. Batch-to-batch variation in the quality of the organic film might be responsible for the fact that the expected inverse scaling with channel thickness is not observed. This is in contrast to the data shown in Figure 6.3a where all devices were fabricated in the same production run and share the same glass substrate. We therefore cannot rule out a volume dependent noise source but a more detailed understanding of the volumetric gating behavior of PEDOT:PSS OECTs at the microscopic level is needed to finally determine the noise source. Note that independent of the exact noise mechanism $S_{Vg} \propto 1/WL$ is expected, as we will verify experimentally in the following.

Figure 6.3c shows the value of the plateau of the gate referred voltage
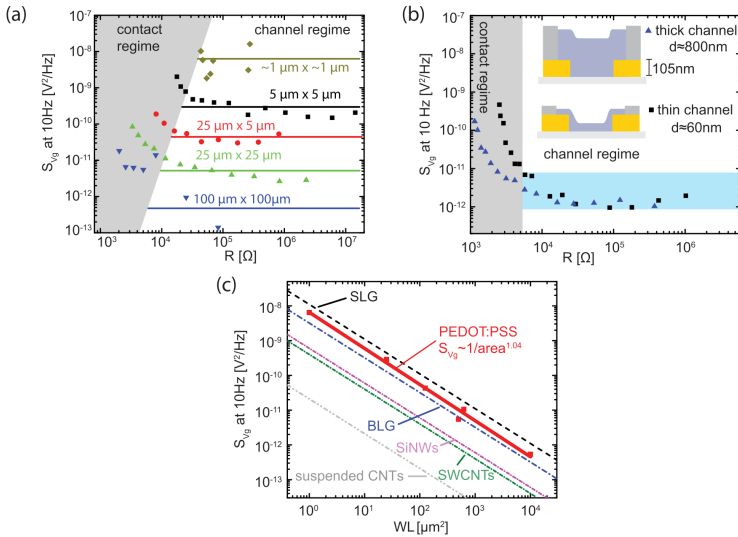
Figure 6.3: (a) Gate referred voltage noise S_{Vg} versus resistance R for five OECTs with different dimensions. For very small resistance values, S_{Vg} increases due to additional contributions from the contact resistance (contact regime). (b) Gate referred voltage noise S_{Vg} versus WL reveals a $1/WL$-dependence. The dashed lines represent the theoretical values obtained in[150] for single-layer and bilayer graphene respectively, SWCNTs[151] and our SiNWs[48].

noise of Figure 6.3a measured for devices of constant thickness $d = 110\,\text{nm}$ versus channel area $= WL$. The thickness of $d = 110\,\text{nm}$ represents a practical trade-off between high transconductance and fast response times [132,134]. As proposed by the charge-noise model, we indeed find that the gate referred voltage noise scales with $S_{Vg} \propto 1/WL$. Furthermore, we compare the value of the gate referred voltage noise with values obtained in literature for transistors based on single- and bi-layer graphene [150], SiNWs [48], substrate-bound SWCNTs [151] and suspended CNTs [155], represented by the dashed colored lines in Figure 6.3b (S_{Vg} for graphene and SWCNT measured at $1\,\text{Hz}$ has been converted to S_{Vg} at $10\,\text{Hz}$ to allow a direct comparison). Interestingly, we find that the noise of OECTs with thickness $d = 110\,\text{nm}$ is comparable with graphene devices while it is slightly higher compared to SiNWs and substrate-bound SWCNTs transistors. Suspending the CNTs has been shown to significantly reduce the noise, an indication that the charge noise caused by the substrate is significantly contributing to the $1/f$ noise [155].

The measured gate referred voltage noise needs to be compared to typical signals of OECTs in sensing applications in order to evaluate the SNR. Recently, analogous OECTs have been modified with K^+-selective membranes to achieve a selective potassium sensor [16]. As discussed in Section 1.1.4, the membrane potential ϕ_M of such ion-sensitive membranes changes according to the Nernst equation by $59.6\,\text{mV/dec}$ in K^+ concentration. In combination with a transistor, ϕ_M acts as an additional gating signal modulating the current of the transistor. The response is given by the change in membrane potential upon a change in target concentration from c_1 to c_2. As defined in Equation 1.27 the response is given by $\Delta\phi_M/\log(c_2/c_1)$ by replacing the surface potential Ψ_0 of the SiNWs with the membrane potential ϕ_M. To calculate the SNR, the change in membrane potential has to be compared to the smallest detectable change in membrane potential $\Delta\phi_{M,min}$ which is given by the gate referred noise $\Delta\phi_{M,min} = \sqrt{S_{Vg}}$.

Assuming a $25\,\mu\text{m}$ x $25\,\mu\text{m}$ OECT modified with a membrane which exhibits a Nernstian response to potassium ions from $1\,\mu\text{M}$ to $1\,\text{M}$, we determine the SNR for an one-order increase in concentration: $SNR = \Delta\phi_M/\sqrt{S_{Vg}} = 59.6\,\text{mV}/\sqrt{1 \cdot 10^{-11}\,\text{V}^2/\text{Hz}} = 18816/\sqrt{\text{Hz}}$ at $10\,\text{Hz}$ with $1\,\text{Hz}$ bandwidth. To calculate the LOD, we remember that the smallest LOD is achieved at the lowest background concentration. Here we simply assume that the lowest concentration is at $c_1 = 1\,\mu\text{M}$. Using Equation 1.28 we find $\log a_{2,min} = \Delta\Psi_{0,min}/response(\Delta\log a) + \log a_1 = \sqrt{1 \cdot 10^{-11}V^2}/59.6\,\text{mV/dec} - 6 \approx 5.9999469$ resulting in $c_{2,min} = 1.000122\,\mu\text{M}$. This means, an increase of $\Delta c = c_{2,min} - c_1 = 122\,\text{pM}$ could

be detected with SNR=1 at the background concentration of $c_1 = 1\,\mu$M.

6.3 Conclusion

In conclusion, we have studied the low-frequency $1/f$ noise in PEDOT:PSS-based OECTs. We were able to quantify for the first time the signal-to-noise ratio and the limit of detection of an OECT in a typical ion-sensing measurement. A comparison with literature shows that the noise of PEDOT:PSS OECTs with typical thickness of $d = 110\,$nm is comparable to graphene FETs and slightly higher compared to SiNWs and substrate-bound SWC-NTs FETs. The experimental data are in good agreement with the charge-noise model, while the α-noise model does not apply. Our results establish a new design rule for the application of OECTs in biochemical/electrostatic sensing experiments, recommending the use of large area polymer channels to maximize the SNR. A comparison with literature shows that the noise of PEDOT:PSS OECTs is comparable to graphene FETs but higher compared to SWCNTs FETs and our SiNWs. Therefore, SiNWs are preferred if high integration is needed due to their low noise. However, for applications where the dimension of the sensor is of secondary importance, large-area OECTs might be an interesting alternative.

7

Conclusions and Outlook

The emerging demand for cheap, portable and label-free biochemical sensors has led to various novel concepts for biochemical sensing. In the presented work, the potential of SiNW ISFETs (Part I) and PEDOT:PSS OECTs (Part II) has been investigated, focusing on the former. Arrays of SiNWs were demonstrated to be good pH sensors with responses at the Nernst limit. The sensing capability can be expanded to other ionic species by surface functionalization as demonstrated in this thesis. The parameters influencing the sensor performance were discussed, focusing on competing surface reactions (usually involving pH) and the noise of the transistor. The platform's potential for monitoring the binding kinetics of protein-ligand interactions was demonstrated. Finally, noise studies of PEDOT:PSS OECTs were performed to evaluate their potential as alternative approach for biochemical sensing.

The major findings of this thesis are summarized in the following: SiNW ISFETs have been developed into a promising sensing platform. The devices fabricated by a top-down approach show good transistor behavior such as high transconductance, low subthreshold swing and small leakage currents. For successful pH sensing, gate dielectrics with a high density of surface hydroxyl groups such as Al_2O_3 or HfO_2 are required. This is explained by the site-binding model which assumes protonation and deprotonation of the surface hydroxyl groups as the surface potential determining process. The observed Nernstian response originates from the local pH buffering intrinsic to a surface with a high density of hydroxyl groups. The model describes the Nernstian response as a uniform process which depends only on the density of the hydroxyl groups and the equilibrium constants of the reactions, but not on the device geometry. This prediction is experimentally validated for

SiNW with widths ranging from 100 nm to 1μm: The pH response does not depend on the nanowire width. While the pH response remains unaffected by the device geometry, the noise decreases for larger structures. Charge trap states at the silicon/oxide interface are identified as the main source of the noise.

For the specific detection of ionic species, the sensor surface needs to be modified with functional groups which selectively bind the target analyte. Unfortunately, the high pH sensitivity of oxide surfaces greatly complicates the detection of any target other than pH. This is due to the coupling of the reactions via the surface potential. In the worst case (given by a highly pH sensitive surface), the target analyte signal is fully suppressed. To circumvent this problem, we propose the use of an additional coating with a material with minimal sensitivity to pH. We find that gold is a promising candidate easily applied for this purpose. The gold layer allows immobilizing ligands via the well-established thiol-based chemistry thereby providing a platform suitable for surface functionalization. Although the gold layer exhibits a residual pH response, this reduced pH sensitivity allows the detection of sodium, fluoride and calcium ions. This is demonstrated with a differential setup having both functionalized and control NWs on the same sample. Furthermore, we find that the residual pH response of the gold layer still influences the detection of the targeted species by affecting the effective binding constant via the surface potential. To take this effect into account, an extended site binding model was proposed. Finally, we show that SiNWs have the potential to monitor binding kinetics of ligand-protein systems and to obtain concentration dependent signals for the clinically relevant FimH protein. Besides SiNWs, organic materials offer great promises for future biosensing applications. We extend our noise study to the conductive polymer PEDOT:PSS operated as an OECT. The measured gate referred noise is higher than our SiNWs. Interestingly, the noise of both devices follows the same scaling with 1/area. Therefore, our finding that the noise is lower for larger structures is confirmed even for different materials.

In the introductory chapter of this thesis, we motivate SiNW arrays as potential candidates for inexpensive, integrated biochemical sensors. During this PhD project, we have critically evaluated how close ISFETs have reached this ideal. The integration of ISFET devices is currently still limited by the lack of a truly integrated external reference electrode. A purely solid state reference electrode has not been demonstrated, yet. However, thanks to advances in mircofluidics, on chip miniaturized Ag/AgCl reference electrodes have recently become available[158,159]. Passivated SiNWs insensitive to pH and any other species could also be used as quasi ref-

erence electrodes in a differential measurement [51,83,160]. The applicability of these approaches to real sensing tasks will greatly determine the future success of the platform. For the integration of the platform, the off-chip extended gate concept is very promising [161,162]. It creates a highly modular sensing platform by spatially separating the sensing layer from the transistor. This approach might further reduce the cost of the device since it allows reusing the same transistor array with different sensing electrodes. Despite the promising pH sensing experiments with extended gates [163,164], it has to be considered that the high modularity comes with additional interference effects due to the parasitic capacitances of the connecting leads. In the case of the SiNW ISFETs studied here, this effect is minimized by having the sensing layer directly on top of the transistor.

During this PhD project, important steps towards an integrable biochemical sensing platform based on SiNWs have been achieved. For pH sensing, the original idea of the ISFET as a miniaturized chemical sensor can be considered accomplished. The pH response of the devices is preserved even at the nanoscale. The fact that the noise increases for smaller NWs might limit the use of very small structures to certain applications. However, the intrinsic limitation of small sensors can be compensated by integrating many sensors in an array. Besides the averaged signal having an improved SNR, the signals of the individual sensors carry additional information useful for spatial and temporal correlations of local pH measurements. In my view, arrays of highly integrated pH sensors offer a big potential and its exploitation has just started; A prominent example is the successful ion torrent DNA sequencer which measures the release of protons upon incorporating of the complementary nucleobase to the DNA sequence of interest [13]. Using a highly integrated array, the system allows parallelizing this principle, drastically increasing the throughput. Further applications based on indirect detection schemes are expected in the near future.

Expanding the sensing capabilities of the ISFET to ionic species other than protons remains a challenging task. However, promising results have been obtained with SAMs of functional molecules. The gold surface reduces the competing effect of pH while allowing densities of the functional SAM high enough for responses up to $40\,mV/dec$. This is still lower than typical responses achieved by ISEs which follow the Nernst equation over a large range of concentration. From our measurements, we conclude that achieving a self-assembled monolayer with a density high enough for a Nernstian response is demanding. The density limit is given by the size of the molecules which have not been optimized in this respect during this PhD project. Using optimized molecules and functionalization protocols, further

increase of the density might be possible. Moving from a monolayer to a thin membrane covalently bound to the surface could be an additional approach for increasing the effective density of sensitive sites.

The application of membranes is mainly restricted to small ionic species and is difficult to be combined with the detection of large biomolecules [20,54]. The capacitive sensor interface provided by the ISFET is therefore of particular interest for biosensing applications. So far, biosensing experiments have been focused on DNA [8–12,165] and streptavidin-biotin [3,8,166] detection. The reliable detection of such large molecules remains a difficult task due to electric field screening and competing surface reactions. Our FimH detection experiments using gold-coated SiNWs highlight again the importance of the sensor material. The reduced density of surface hydroxyl groups due to the additional gold layer allows the successful FimH detection. Despite the utility of the gold layer, the search for new sensing materials must not be neglected. The experience gained in our group in particular with graphene, raises the hope that more suitable materials for sensing can be found. This is justified by the fact that graphene is insensitive to pH [167] but allows surface functionalizations [168]. Future efforts should also extend the theoretical modeling to provide a deeper understanding of the complex sensor/solution interface.

More than 40 years after the ISFET's invention, the development of integrated biochemical sensors remains a dynamic field of applied research. SiNW ISFET are promising devices towards this goal, their compatibility with CMOS technology being a key advantage. However, alternative approaches including organic materials may expand the possibilities. The future success of the presented sensing concepts depends highly on the application. A detailed understanding of the limiting factors and the corresponding workarounds are crucial to find the optimum sensor for a certain application. The presented work is intended to contribute to this task of bringing the ISFET from the lab to the actual application.

Bibliography

[1] N. S. Foundation, "The sensor revolution." online. Accessed: 2015-08-25.

[2] P. Bergveld, "Development of an ion-sensitive solid-state device for neurophysiological measurements," *IEEE Trans. Biomed. Eng.*, vol. BME-17, no. 1, pp. 70–71, 1970.

[3] Y. Cui, Q. Wei, H. Park, and C. M. Lieber, "Nanowire nanosensors for highly sensitive and selective detection of biological and chemical species," *Science*, vol. 293, no. 5533, pp. 1289–1292, 2001.

[4] O. Knopfmacher, A. Tarasov, W. Fu, M. Wipf, B. Niesen, M. Calame, and C. Schönenberger, "Nernst limit in dual-gated Si-nanowire FET sensors," *Nano Lett.*, vol. 10, no. 6, pp. 2268–2274, 2010.

[5] S. Chen, J. G. Bomer, E. T. Carlen, and A. van den Berg, "Al_2O_3/silicon nanoISFET with near ideal nernstian response," *Nano Lett.*, vol. 11, no. 6, pp. 2334–2341, 2011.

[6] C. Duarte-Guevara, F.-L. Lai, C.-W. Cheng, B. J. Reddy, E. Salm, V. Swaminathan, Y.-K. Tsui, H. C. Tuan, A. Kalnitsky, Y.-S. Liu, and R. Bashir, "Enhanced biosensing resolution with foundry fabricated individually addressable dual-gated ISFETs," *Anal. Chem.*, vol. 86, no. 16, pp. 8359–8367, 2014.

[7] M. Wipf, *Chemical and Biochemical Sensors Based on Silicon Nanowire Field-Effect Transistor Arrays.* PhD thesis, University of Basel, 05 2014.

[8] X. Duan, Y. Li, N. K. Rajan, D. A. Routenberg, Y. Modis, and M. A. Reed, "Quantification of the affinities and kinetics of protein interactions using silicon nanowire biosensors," *Nat. Nanotechnol.*, vol. 7, no. 6, pp. 401–407, 2012.

117

[9] Z. Li, Y. Chen, X. Li, T. I. Kamins, K. Nauka, and R. S. Williams, "Sequence-specific label-free DNA sensors based on silicon nanowires," *Nano Lett.*, vol. 4, no. 2, pp. 245–247, 2004.

[10] L. Benini, C. Guiducci, and C. Paulus, "Electronic detection of DNA hybridization: Toward CMOS microarrays," *IEEE Des. Test Comput.*, vol. 24, no. 1, pp. 38–48, 2007.

[11] S. Ingebrandt, Y. Han, F. Nakamura, A. Poghossian, M. Schöning, and A. Offenhäusser, "Label-free detection of single nucleotide polymorphisms utilizing the differential transfer function of field-effect transistors," *Biosens. Bioelectron.*, vol. 22, no. 12, pp. 2834 – 2840, 2007.

[12] A. Gao, N. Lu, Y. Wang, P. Dai, T. Li, X. Gao, Y. Wang, and C. Fan, "Enhanced sensing of nucleic acids with silicon nanowire field effect transistor biosensors," *Nano Lett.*, vol. 12, no. 10, pp. 5262–5268, 2012.

[13] J. M. Rothberg, W. Hinz, T. M. Rearick, J. Schultz, W. Mileski, M. Davey, J. H. Leamon, K. Johnson, M. J. Milgrew, M. Edwards, J. Hoon, J. F. Simons, D. Marran, J. W. Myers, J. F. Davidson, A. Branting, J. R. Nobile, B. P. Puc, D. Light, T. A. Clark, M. Huber, J. T. Branciforte, I. B. Stoner, S. E. Cawley, M. Lyons, Y. Fu, N. Homer, M. Sedova, X. Miao, B. Reed, J. Sabina, E. Feierstein, M. Schorn, M. Alanjary, E. Dimalanta, D. Dressman, R. Kasinskas, T. Sokolsky, J. A. Fidanza, E. Namsaraev, K. J. McKernan, A. Williams, G. T. Roth, and J. Bustillo, "An integrated semiconductor device enabling non-optical genome sequencing," *Nature*, vol. 475, no. 7356, pp. 348–352, 2011.

[14] P. Lin, F. Yan, and H. L. W. Chan, "Ion-sensitive properties of organic electrochemical transistors," *ACS Appl. Mater. Interfaces*, vol. 2, no. 6, pp. 1637–1641, 2010.

[15] P. Lin and F. Yan, "Organic thin-film transistors for chemical and biological sensing," *Adv. Mater.*, vol. 24, no. 1, pp. 34–51, 2012.

[16] M. Sessolo, J. Rivnay, E. Bandiello, G. G. Malliaras, and H. J. Bolink, "Ion-selective organic electrochemical transistors," *Adv. Mater.*, vol. 26, no. 28, pp. 4803–4807, 2014.

[17] R. Piosik, R. Peper, and W. Jansen, "100 Jahre Glaselektrode. The centenary of the glass electrode," *CHEMKON*, vol. 17, no. 1, pp. 19–24, 2010.

[18] A. Belyustin, "The centenary of glass electrode: From Max Cremer to F. G. K. Baucke," *J. Solid State Electrochem.*, vol. 15, no. 1, pp. 47–65, 2011.

[19] F. Baucke, "Fundamental and applied electrochemistry at an industrial glass laboratory: An overview," *J. Solid State Electrochem.*, vol. 15, no. 1, pp. 23–46, 2011.

[20] M. J. Madou and S. R. Morrison, *Chemical Sensing with Solid State Devices*. Academic Press, INC., 1989.

[21] S. D. Moss, J. Janata, and C. C. Johnson, "Potassium ion-sensitive field effect transistor," *Anal. Chem.*, vol. 47, no. 13, pp. 2238–2243, 1975.

[22] P. Bergveld, "Thirty years of isfetology: What happened in the past 30 years and what may happen in the next 30 years," *Sens. Actuators, B*, vol. 88, no. 1, pp. 1–20, 2003.

[23] J. Janata, "Historical review. Twenty years of ion-selective field-effect transistors," *Analyst*, vol. 119, pp. 2275–2278, 1994.

[24] J. Janata and R. J. Huber, eds., *Solid State Chemical Sensors*. Academic Press, INC., 1985.

[25] J. Sutter, A. Radu, S. Peper, E. Bakker, and E. Pretsch, "Solid-contact polymeric membrane electrodes with detection limits in the subnanomolar range," *Anal. Chim. Acta*, vol. 523, no. 1, pp. 53 – 59, 2004.

[26] E. Bakker, P. Bühlmann, and E. Pretsch, "Carrier-based ion-selective electrodes and bulk optodes. 1. General characteristics," *Chem. Rev.*, vol. 97, no. 8, pp. 3083–3132, 1997.

[27] S. M. Sze, *Physics of Semiconductor Devices*. Wiley-Interscience, 2006.

[28] V. Bagotsky, *Fundamentals of Electrochemistry*. The ECS Series of Texts and Monographs, John Wiley & Sons: Hoboken, 2005.

[29] J. Janata, "Chemical sensors," *Anal. Chem.*, vol. 64, no. 12, pp. R196–R219, 1992.

[30] J. R. Sandifer, "Theory of interfacial potential differences: effects of adsorption onto hydrated (gel) and nonhydrated surfaces," *Anal. Chem.*, vol. 60, no. 15, pp. 1553–1562, 1988.

[31] A. Mulchandani, P. Mulchandani, S. Chauhan, I. Kaneva, and W. Chen, "A potentiometric microbial biosensor for direct determination of organophosphate nerve agents," *Electroanalysis*, vol. 10, no. 11, pp. 733–737, 1998.

[32] A. Radomska, E. Bodenszac, S. Głąb, and R. Koncki, "Creatinine biosensor based on ammonium ion selective electrode and its application in flow-injection analysis," *Talanta*, vol. 64, no. 3, pp. 603 – 608, 2004.

[33] K. Y. Chumbimuni-Torres, Z. Dai, N. Rubinova, Y. Xiang, E. Pretsch, J. Wang, and E. Bakker, "Potentiometric biosensing of proteins with ultrasensitive ion-selective microelectrodes and nanoparticle labels," *J. Am. Chem. Soc.*, vol. 128, no. 42, pp. 13676–13677, 2006.

[34] D. E. Yates, S. Levine, and T. W. Healy, "Site-binding model of the electrical double layer at the oxide/water interface," *J. Chem. Soc., Faraday Trans.*, vol. 70, pp. 1807–1818, 1974.

[35] R. van Hal, J. Eijkel, and P. Bergveld, "A general model to describe the electrostatic potential at electrolyte oxide interfaces," *Adv. Colloid Interface Sci.*, vol. 69, no. 1-3, pp. 31–62, 1996.

[36] W. Siu and R. Cobbold, "Basic properties of the electrolyte SiO_2 Si system: Physical and theoretical aspects," *IEEE Trans. Electron Devices*, vol. 26, no. 11, pp. 1805–1815, 1979.

[37] L. Bousse, N. F. D. Rooij, and P. Bergveld, "The influence of counterion adsorption on the ψ_0/pH characteristics of insulator surfaces," *Surf. Sci.*, vol. 135, no. 3, pp. 479 – 496, 1983.

[38] L. Bousse, N. De Rooij, and P. Bergveld, "Operation of chemically sensitive field-effect sensors as a function of the insulator-electrolyte interface," *IEEE Trans. Electron Devices*, vol. 30, no. 10, pp. 1263–1270, 1983.

[39] J. Janata, "Graphene bio-field-effect transistor myth," *ECS Solid State Lett.*, vol. 1, no. 6, pp. M29–M31, 2012.

[40] R. K. Iler, *The Chemistry of Silica: Solubility, Polymerization, Colloid and Surface Properties and Biochemistry of Silica.* Wiley, 1979.

[41] A. Cao, M. Mescher, D. Bosma, J. H. Klootwijk, E. J. R. Sudhölter, and L. C. d. Smet, "Ionophore-containing siloprene membranes: Direct comparison between conventional ion-selective electrodes and silicon nanowire-based field-effect transistors," *Anal. Chem.*, vol. 87, no. 2, pp. 1173–1179, 2015.

[42] J. Knight, "Microfluidics: Honey, I shrunk the lab," *Nature*, vol. 418, pp. 474–475, Aug. 2002.

[43] R. Sivakumarasamy, K. Nishiguchi, A. Fujiwara, D. Vuillaume, and N. Clément, "A simple and inexpensive technique for PDMS/silicon chip alignment with sub-μm precision," *Anal. Methods*, vol. 6, pp. 97–101, 2014.

[44] X. P. A. Gao, G. Zheng, and C. M. Lieber, "Subthreshold regime has the optimal sensitivity for nanowire FET biosensors," *Nano Lett.*, vol. 10, no. 2, pp. 547–552, 2010.

[45] E. Stern, J. F. Klemic, D. A. Routenberg, P. N. Wyrembak, D. B. Turner-Evans, A. D. Hamilton, D. A. LaVan, T. M. Fahmy, and M. A. Reed, "Label-free immunodetection with CMOS-compatible semiconducting nanowires," *Nature*, vol. 445, no. 7127, pp. 519–522, 2007.

[46] P. E. Sheehan and L. J. Whitman, "Detection limits for nanoscale biosensors," *Nano Lett.*, vol. 5, no. 4, pp. 803–807, 2005.

[47] K. Bedner, V. A. Guzenko, A. Tarasov, M. Wipf, R. L. Stoop, D. Just, S. Rigante, W. Fu, R. A. Minamisawa, C. David, M. Calame, J. Gobrecht, and C. Schönenberger, "pH response of silicon nanowire sensors: Impact of nanowire width and gate oxide," *Sens. Mater.*, vol. 25, no. 8, pp. 567–576, 2013.

[48] K. Bedner, V. A. Guzenko, A. Tarasov, M. Wipf, R. L. Stoop, S. Rigante, J. Brunner, W. Fu, C. David, M. Calame, J. Gobrecht, and C. Schönenberger, "Investigation of the dominant 1/f noise source in silicon nanowire sensors," *Sens. Actuators, B*, vol. 191, no. 0, pp. 270 – 275, 2014.

[49] K. Bedner, *Fabrication and Characterization of Ion-Sensitive Field-Effect Transistors using Silicon-on-Insulator Technology*. PhD thesis, University of Basel, Paul Scherrer Institut, 2013.

[50] O. S. Knopfmacher, *Sensing with Silicon Nanowire Field-Effect Transistors*. PhD thesis, University of Basel, Department of Physics, 2011.

[51] A. Tarasov, M. Wipf, K. Bedner, J. Kurz, W. Fu, V. A. Guzenko, O. Knopfmacher, R. L. Stoop, M. Calame, and C. Schönenberger, "True reference nanosensor realized with silicon nanowires," *Langmuir*, vol. 28, no. 25, pp. 9899–9905, 2012.

[52] M. Wipf, R. L. Stoop, A. Tarasov, K. Bedner, W. Fu, M. Calame, and C. Schönenberger, "Potassium sensing with membrane-coated silicon nanowire field-effect transistors," in *2013 Transducers Eurosensors XXVII: The 17th International Conference on Solid-State Sensors, Actuators and Microsystems*, pp. 1182–1185, 2013.

[53] A. Tarasov, M. Wipf, R. L. Stoop, K. Bedner, W. Fu, V. A. Guzenko, O. Knopfmacher, M. Calame, and C. Schönenberger, "Understanding the electrolyte background for biochemical sensing with ion-sensitive field-effect transistors," *ACS Nano*, vol. 6, no. 10, pp. 9291–9298, 2012.

[54] R. Schasfoort, P. Bergveld, R. Kooyman, and J. Greve, "Possibilities and limitations of direct detection of protein charges by means of an immunological field-effect transistor," *Anal. Chim. Acta*, vol. 238, pp. 323–329, 1990.

[55] P. Bergveld, "A critical evaluation of direct electrical protein detection methods," *Biosens. Bioelectron.*, vol. 6, no. 1, pp. 55 – 72, 1991.

[56] L. Meixner and S. Koch, "Simulation of isfet operation based on the site-binding model," *Sens. Actuators, B*, vol. 6, no. 13, pp. 315 – 318, 1992.

[57] P. T. Mcbride, J. Janata, P. A. Comte, S. D. Moss, and C. C. Johnson, "Ion-selective field effect transistors with polymeric membranes," *Anal. Chim. Acta*, vol. 101, no. 2, pp. 239 – 245, 1978.

[58] L. Park, Y. Hur, and B. Sohn, "Effect of membrane structure on the performance of field-effect transistor potassium-sensitive sensor," *Sens. Actuators, A*, vol. 57, no. 3, pp. 239–243, 1996.

[59] E. J. R. Sudhölter, P. D. van der Wal, M. Skowronska-Ptasinska, A. van den Berg, and D. N. Reinhoudt, "Ion-sensing using chemically-modified ISFETs," *Sens. Actuators*, vol. 17, no. 1-2, pp. 189–194, 1989.

[60] L. Luo, J. Jie, W. Zhang, Z. He, J. Wang, G. Yuan, W. Zhang, L. C. M. Wu, and S.-T. Lee, "Silicon nanowire sensors for Hg^{2+} and Cd^{2+} ions," *Appl. Phys. Lett.*, vol. 94, no. 19, p. 193101, 2009.

[61] B. Dorvel, B. J. Reddy, and R. Bashir, "Effect of biointerfacing linker chemistries on the sensitivity of silicon nanowires for protein detection," *Anal. Chem.*, vol. 85, no. 20, pp. 9493–9500, 2013.

[62] B. K. Wunderlich, P. A. Neff, and A. R. Bausch, "Mechanism and sensitivity of the intrinsic charge detection of biomolecular interactions by field effect devices," *Appl. Phys. Lett.*, vol. 91, no. 8, p. 083904, 2007.

[63] R. L. Stoop, M. Wipf, S. Müller, K. Bedner, I. A. Wright, C. J. Martin, E. C. Constable, W. Fu, A. Tarasov, M. Calame, and C. Schönenberger, "Competing surface reactions limiting the performance of ion-sensitive field-effect transistors," *Sens. Actuators, B*, vol. 220, no. 0, pp. 500 – 507, 2015.

[64] A. Watts, ed., *Protein-Lipid Interactions*. Elsevier: Amsterdam, 1993.

[65] M. von Hartman, *Low-Frequency Noise in Advanced MOS Devices*. Springer, 2007.

[66] F. N. Hooge, T. G. M. Kleinpenning, and L. K. J. Vandamme, "Experimental studies on 1/f noise," *Reports on Progress in Physics*, vol. 44, no. 5, p. 479, 1981.

[67] F. N. Hooge, "l/f noise sources," *IEEE Trans. Electron Devices*, 1994.

[68] M. von Haartman and M. Östling, *Low-Frequency Noise in Advanced MOS Devices*. Analog Circuits and Signal Processing, Springer, 2007.

[69] L. Vandamme, X. Li, and D. Rigaud, "1/f noise in MOS devices, mobility or number fluctuations?," *IEEE Trans. Electron Devices*, vol. 41, no. 11, pp. 1936–1945, 1994.

[70] N. K. Rajan, K. Brower, X. Duan, and M. A. Reed, "Limit of detection of field effect transistor biosensors: Effects of surface modification and size dependence," *Appl. Phys. Lett.*, vol. 104, no. 8, p. 084106, 2014.

[71] A. Tarasov, W. Fu, O. Knopfmacher, J. Brunner, M. Calame, and C. Schönenberger, "Signal-to-noise ratio in dual-gated silicon nanorib-bon field-effect sensors," *Appl. Phys. Lett.*, vol. 98, no. 1, p. 012114, 2011.

[72] N. Clément, K. Nishiguchi, A. Fujiwara, and D. Vuillaume, "One-by-one trap activation in silicon nanowire transistors," *Nat. Commun.*, vol. 1, p. 92, 2010.

[73] N. Clément, K. Nishiguchi, J. F. Dufreche, D. Guerin, A. Fujiwara, and D. Vuillaume, "A silicon nanowire ion-sensitive field-effect tran-sistor with elementary charge sensitivity," *Appl. Phys. Lett.*, vol. 98, no. 1, p. 014104, 2011.

[74] P. R. Nair and M. A. Alam, "Screening-limited response of nanobiosensors," *Nano Lett.*, vol. 8, no. 5, pp. 1281–1285, 2008.

[75] A. Vacic, J. M. Criscione, N. K. Rajan, E. Stern, T. M. Fahmy, and M. A. Reed, "Determination of molecular configuration by Debye length modulation," *J. Am. Chem. Soc.*, vol. 133, no. 35, pp. 13886–13889, 2011.

[76] K. Shoorideh and C. O. Chui, "On the origin of enhanced sensitivity in nanoscale FET-based biosensors," *Proc. Natl. Acad. Sci. U. S. A.*, vol. 111, no. 14, pp. 5111–5116, 2014.

[77] G. S. Kulkarni and Z. Zhong, "Detection beyond the Debye screen-ing length in a high-frequency nanoelectronic biosensor," *Nano Lett.*, vol. 12, no. 2, pp. 719–723, 2012.

[78] N. Gao, W. Zhou, X. Jiang, G. Hong, T.-M. Fu, and C. M. Lieber, "General strategy for biodetection in high ionic strength solutions using transistor-based nanoelectronic sensors," *Nano Lett.*, vol. 15, no. 3, pp. 2143–2148, 2015.

[79] N. Elfström, A. E. Karlström, and J. Linnros, "Silicon nanoribbons for electrical detection of biomolecules," *Nano Lett.*, vol. 8, no. 3, pp. 945–949, 2008.

[80] G. Zheng, F. Patolsky, Y. Cui, W. U. Wang, and C. M. Lieber, "Mul-tiplexed electrical detection of cancer markers with nanowire sensor arrays," *Nat. Biotechnol.*, vol. 23, no. 10, pp. 1294–1301, 2005.

[81] E. J. Sudhölter, P. D. van der Wal, M. Skowronska-Ptasinska, A. van den Berg, P. Bergveld, and D. N. Reinhoudt, "Modification of ISFETs by covalent anchoring of poly(hyroxyethyl methacrylate) hydrogel. introduction of a thermodynamically defined semiconductor-sensing membrane interface," *Anal. Chim. Acta*, vol. 230, no. 0, pp. 59 – 65, 1990.

[82] H. Perrot, N. Jaffrezic-Renault, N. D. Rooij, and H. V. D. Vlekkert, "Ionic detection using differential measurement between an ion-sensitive FET and a reference FET," *Sens. Actuators*, vol. 20, no. 3, pp. 293–299, 1989.

[83] M. Wipf, R. L. Stoop, A. Tarasov, K. Bedner, W. Fu, I. A. Wright, C. J. Martin, E. C. Constable, M. Calame, and C. Schönenberger, "Selective sodium sensing with gold-coated silicon nanowire field-effect transistors in a differential setup," *ACS Nano*, vol. 7, no. 7, pp. 5978–5983, 2013.

[84] M. Lohrengel and J. Schultze, "Electrochemical properties of anodic gold oxide layers-i: Potentiostatic oxide growth and double layer capacity," *Electrochim. Acta*, vol. 21, no. 11, pp. 957–965, 1976.

[85] H. Ron and I. Rubinstein, "Alkanethiol monolayers on preoxidized gold. encapsulation of gold oxide under an organic monolayer," *Langmuir*, vol. 10, no. 12, pp. 4566–4573, 1994.

[86] H. Ron, S. Matlis, and I. Rubinstein, "Self-assembled monolayers on oxidized metals. 2. gold surface oxidative pretreatment, monolayer properties, and depression formation," *Langmuir*, vol. 14, no. 5, pp. 1116–1121, 1998.

[87] J. Steed and J. Atwood, *Supramolecular Chemistry*. John Wiley & Sons, 2009.

[88] R. Williams, "pKa data compiled by R. Williams," (accessed September 2, 2014).

[89] R. Y. Tsien, "New calcium indicators and buffers with high selectivity against magnesium and protons: Design, synthesis, and properties of prototype structures," *Biochemistry*, vol. 19, no. 11, pp. 2396–2404, 1980.

[90] R. B. Schasfoort, W. de Lau, A. van der Kooi, H. Clevers, and G. H. Engbers, "Method for estimating the single molecular affinity," *Anal. Biochem.*, vol. 421, no. 2, pp. 794 – 796, 2012.

[91] S. Rigante, P. Scarbolo, M. Wipf, R. L. Stoop, K. Bedner, E. Buitrago, A. Bazigos, D. Bouvet, M. Calame, C. Schönenberger, and A. M. Ionescu, "Sensing with advanced computing technology: Fin field-effect transistors with high-k gate stack on bulk silicon," *ACS Nano*, vol. 9, no. 5, pp. 4872–4881, 2015.

[92] G. S. Wilson and R. Gifford, "Biosensors for real-time in vivo measurements," *Biosens. Bioelectron.*, vol. 20, no. 12, pp. 2388 – 2403, 2005.

[93] M. M.-C. Cheng, G. Cuda, Y. L. Bunimovich, M. Gaspari, J. R. Heath, H. D. Hill, C. A. Mirkin, A. J. Nijdam, R. Terracciano, T. Thundat, and M. Ferrari, "Nanotechnologies for biomolecular detection and medical diagnostics," *Curr. Opin. Chem. Biol.*, vol. 10, no. 1, pp. 11 – 19, 2006.

[94] M. A. Cooper, "Optical biosensors in drug discovery," *Nat. Rev. Drug Discovery*, vol. 1, no. 7, pp. 515–528, 2002.

[95] N. K. Rajan, X. Duan, and M. A. Reed, "Performance limitations for nanowire/nanoribbon biosensors," *Wiley Interdiscip. Rev.: Nanomed. Nanobiotechnol.*, vol. 5, pp. 629–645, 2013.

[96] M. Curreli, R. Zhang, F. Ishikawa, H.-K. Chang, R. Cote, C. Zhou, and M. E. Thompson, "Real-time, label-free detection of biological entities using nanowire-based FETs," *IEEE Trans. Nanotechnol.*, vol. 7, no. 6, pp. 651–667, 2008.

[97] E. Stern, A. Vacic, and M. A. Reed, "Semiconducting nanowire field-effect transistor biomolecular sensors," *IEEE Trans. Electron Devices*, vol. 55, no. 11, pp. 3119–3130, 2008.

[98] Y. L. Bunimovich, Y. S. Shin, W.-S. Yeo, M. Amori, G. Kwong, and J. R. Heath, "Quantitative real-time measurements of dna hybridization with alkylated nonoxidized silicon nanowires in electrolyte solution," *J. Am. Chem. Soc.*, vol. 128, no. 50, pp. 16323–16331, 2006.

[99] J. DeChancie and K. N. Houk, "The origins of femtomolar protein-ligand binding: Hydrogen-bond cooperativity and desolvation energetics in the biotin-(strept)avidin binding site," *J. Am. Chem. Soc.*, vol. 129, no. 17, pp. 5419–5429, 2007.

[100] N. Sharon, "Lectins: Carbohydrate-specific reagents and biological recognition molecules," *J. Biol. Chem.*, vol. 282, no. 5, pp. 2753–2764, 2007.

[101] H. Ghazarian, B. Idoni, and S. B. Oppenheimer, "A glycobiology review: carbohydrates, lectins, and implications in cancer therapeutics," *Acta Histochem.*, vol. 113, no. 3, pp. 236–247, 2010.

[102] L. Zhang and B. Foxman, "Molecular epidemiology of escherichia coli mediated urinary tract infections," *Front. Biosci.*, vol. 8, pp. E235–E244, 2003.

[103] L. Cegelski, G. R. Marshall, G. R. Eldridge, and S. J. Hultgren, "The biology and future prospects of antivirulence therapies," *Nat. Rev. Micro.*, vol. 6, no. 1, pp. 17–27, 2008.

[104] T. Klein, D. Abgottspon, M. Wittwer, S. Rabbani, J. Herold, X. Jiang, S. Kleeb, C. Lüthi, M. Scharenberg, J. Bezençon, E. Gubler, L. Pang, M. Smiesko, B. Cutting, O. Schwardt, and B. Ernst, "FimH antagonists for the oral treatment of urinary tract infections: From design and synthesis to in vitro and in vivo evaluation," *J. Med. Chem.*, vol. 53, no. 24, pp. 8627–8641, 2010.

[105] X. Jiang, D. Abgottspon, S. Kleeb, S. Rabbani, M. Scharenberg, M. Wittwer, M. Haug, O. Schwardt, and B. Ernst, "Antiadhesion therapy for urinary tract infections – a balanced pK/pD profile proved to be key for success," *J. Med. Chem.*, vol. 55, no. 10, pp. 4700–4713, 2012.

[106] L. Pang, S. Kleeb, K. Lemme, S. Rabbani, M. Scharenberg, A. Zalewski, F. Schädler, O. Schwardt, and B. Ernst, "FimH antagonists: Structure-activity and structure-property relationships for biphenyl α-d-mannopyranosides," *ChemMedChem*, vol. 7, no. 8, pp. 1404–1422, 2012.

[107] S. Kleeb, L. Pang, K. Mayer, D. Eris, A. Sigl, R. C. Preston, P. Zihlmann, T. Sharpe, R. P. Jakob, D. Abgottspon, A. S. Hutter, M. Scharenberg, X. Jiang, G. Navarra, S. Rabbani, M. Smiesko,

N. Lüdin, J. Bezençon, O. Schwardt, T. Maier, and B. Ernst, "FimH antagonists: Bioisosteres to improve the in vitro and in vivo pK/pD profile," *J. Med. Chem.*, vol. 58, no. 5, pp. 2221–2239, 2015.

[108] P. Livi, A. Shadmani, M. Wipf, R. L. Stoop, J. Rothe, Y. Chen, M. Calame, C. Schönenberger, and A. Hierlemann, "Sensor system including silicon nanowire ion sensitive FET arrays and CMOS read-out," *Sens. Actuators, B*, vol. 204, pp. 568–577, 2014.

[109] S. Rabbani, X. Jiang, O. Schwardt, and B. Ernst, "Expression of the carbohydrate recognition domain of FimH and development of a competitive binding assay," *Anal. Biochem.*, vol. 407, no. 2, pp. 188 – 195, 2010.

[110] M. Scharenberg, X. Jiang, L. Pang, G. Navarra, S. Rabbani, F. Binder, O. Schwardt, and B. Ernst, "Kinetic properties of carbohydrate – lectin interactions: FimH antagonists," *ChemMedChem*, vol. 9, no. 1, pp. 78–83, 2014.

[111] B. N. Anderson, A. M. Ding, L. M. Nilsson, K. Kusuma, V. Tchesnokova, V. Vogel, E. V. Sokurenko, and W. E. Thomas, "Weak rolling adhesion enhances bacterial surface colonization," *J. Bacteriol.*, vol. 189, no. 5, pp. 1794–1802, 2007.

[112] O. Yakovenko, S. Sharma, M. Forero, V. Tchesnokova, P. Aprikian, B. Kidd, A. Mach, V. Vogel, E. Sokurenko, and W. E. Thomas, "FimH forms catch bonds that are enhanced by mechanical force due to allosteric regulation," *J. Biol. Chem.*, vol. 283, no. 17, pp. 11596–11605, 2008.

[113] M. J. Cannon, G. A. Papalia, I. Navratilova, R. J. Fisher, L. R. Roberts, K. M. Worthy, A. G. Stephen, G. R. Marchesini, E. J. Collins, D. Casper, H. Qiu, D. Satpaev, S. F. Liparoto, D. A. Rice, I. I. Gorshkova, R. J. Darling, D. B. Bennett, M. Sekar, E. Hommema, A. M. Liang, E. S. Day, J. Inman, S. M. Karlicek, S. J. Ullrich, D. Hodges, T. Chu, E. Sullivan, J. Simpson, A. Rafique, B. Luginbühl, S. N. Westin, M. Bynum, P. Cachia, Y.-J. Li, D. Kao, A. Neurauter, M. Wong, M. Swanson, and D. G. Myszka, "Comparative analyses of a small molecule/enzyme interaction by multiple users of biacore technology," *Anal. Biochem.*, vol. 330, no. 1, pp. 98 – 113, 2004.

[114] P. S. Katsamba, I. Navratilova, M. Calderon-Cacia, L. Fan, K. Thornton, M. Zhu, T. V. Bos, C. Forte, D. Friend, I. Laird-Offringa,

G. Tavares, J. Whatley, E. Shi, A. Widom, K. C. Lindquist, S. Klakamp, A. Drake, D. Bohmann, M. Roell, L. Rose, J. Dorocke, B. Roth, B. Luginbühl, and D. G. Myszka, "Kinetic analysis of a high-affinity antibody/antigen interaction performed by multiple biacore users," *Anal. Biochem.*, vol. 352, no. 2, pp. 208 – 221, 2006.

[115] D. G. Myszka, X. He, M. Dembo, T. A. Morton, and B. Goldstein, "Extending the range of rate constants available from biacore: Interpreting mass transport-influenced binding data," *Biophys. J.*, pp. 583–594, 1998.

[116] R. S. Gaster, L. Xu, S.-J. Han, R. J. Wilson, D. A. Hall, S. J. Osterfeld, H. Yu, and S. X. Wang, "Quantification of protein interactions and solution transport using high-density GMR sensor arrays," *Nat. Nanotechnol.*, vol. 6, no. 5, pp. 314–320, 2011.

[117] G. Zardeneta, H. Mukai, V. Marker, and S. B. Milam, "Protein interactions with particulate teflon: Implications for the foreign body response," *J. Oral Maxillofac. Surg.*, vol. 54, no. 7, pp. 873 – 878, 1996.

[118] T. Sikanen, S. K. Wiedmer, L. Heikkilä, S. Franssila, R. Kostiainen, and T. Kotiaho, "Dynamic coating of SU-8 microfluidic chips with phospholipid disks," *Electrophoresis*, vol. 31, no. 15, pp. 2566–2574, 2010.

[119] M. F. Mora, C. E. Giacomelli, and C. D. Garcia, "Electrophoretic effects of the adsorption of anionic surfactants to poly(dimethylsiloxane)-coated capillaries," *Anal. Chem.*, vol. 79, no. 17, pp. 6675–6681, 2007.

[120] D. Habauzit, J. Chopineau, and B. Roig, "SPR-based biosensors: a tool for biodetection of hormonal compounds," *Anal. Bioanal. Chem.*, vol. 387, no. 4, pp. 1215–1223, 2007.

[121] M. Rabe, D. Verdes, and S. Seeger, "Understanding protein adsorption phenomena at solid surfaces," *Advances in Colloid and Interface Science*, vol. 162, no. 1–2, pp. 87 – 106, 2011.

[122] P. Roach, D. Farrar, and C. C. Perry, "Interpretation of protein adsorption: Surface-induced conformational changes," *J. Am. Chem. Soc.*, vol. 127, no. 22, pp. 8168–8173, 2005.

[123] S. Liu and X. Guo, "Carbon nanomaterials field-effect-transistor-based biosensors," *NPG Asia Mater.*, vol. 4, p. e23, 2012.

[124] S. H. Kim, K. Hong, W. Xie, K. H. Lee, S. Zhang, T. P. Lodge, and C. D. Frisbie, "Electrolyte-gated transistors for organic and printed electronics," *Adv. Mater.*, vol. 25, no. 13, pp. 1822–1846, 2013.

[125] H. Shirakawa, E. J. Louis, A. G. MacDiarmid, C. K. Chiang, and A. J. Heeger, "Synthesis of electrically conducting organic polymers: Halogen derivatives of polyacetylene, (ch)," *J. Chem. Soc., Chem. Commun.*, pp. 578–580, 1977.

[126] G. Malliaras and R. Friend, "An organic electronics primer," *Phys. Today*, vol. 58, pp. 53–58, May 2005.

[127] M. Berggren and A. Richter-Dahlfors, "Organic bioelectronics," *Adv. Mater.*, vol. 19, no. 20, pp. 3201–3213, 2007.

[128] J. Rivnay, R. M. Owens, and G. G. Malliaras, "The rise of organic bioelectronics," *Chem. Mater.*, vol. 26, no. 1, pp. 679–685, 2014.

[129] B. Sakmann and E. Neher, "Patch clamp techniques for studying ionic channels in excitable membranes," *Annu. Rev. Physiol.*, vol. 46, no. 1, pp. 455–472, 1984.

[130] X. Cui, V. A. Lee, Y. Raphael, J. A. Wiler, J. F. Hetke, D. J. Anderson, and D. C. Martin, "Surface modification of neural recording electrodes with conducting polymer/biomolecule blends," *J. Biomed. Mater. Res.*, vol. 56, no. 2, pp. 261–272, 2001.

[131] H. S. White, G. P. Kittlesen, and M. S. Wrighton, "Chemical derivatization of an array of three gold microelectrodes with polypyrrole: Fabrication of a molecule-based transistor," *J. Am. Chem. Soc.*, vol. 106, no. 18, pp. 5375–5377, 1984.

[132] D. Khodagholy, J. Rivnay, M. Sessolo, M. Gurfinkel, P. Leleux, L. H. Jimison, E. Stavrinidou, T. Hervé, S. Sanaur, R. M. Owens, and G. G. Malliaras, "High transconductance organic electrochemical transistors," *Nat. Commun.*, vol. 4, 2013.

[133] J. Rivnay, P. Leleux, M. Sessolo, D. Khodagholy, T. Hervé, M. Fiocchi, and G. G. Malliaras, "Organic electrochemical transistors with maximum transconductance at zero gate bias," *Adv. Mater.*, vol. 25, no. 48, pp. 7010–7014, 2013.

[134] J. Rivnay, P. Leleux, M. Ferro, M. Sessolo, A. Williamson, D. A. Koutsouras, D. Khodagholy, M. Ramuz, X. Strakosas, R. M. Owens, C. Benar, J.-M. Badier, C. Bernard, and G. G. Malliaras, "High-performance transistors for bioelectronics through tuning of channel thickness," *Sci. Adv.*, vol. 1, no. 4, 2015.

[135] D. A. Bernards, D. J. Macaya, M. Nikolou, J. A. DeFranco, S. Takamatsu, and G. G. Malliaras, "Enzymatic sensing with organic electrochemical transistors," *J. Mater. Chem.*, vol. 18, pp. 116–120, 2008.

[136] L. Kergoat, B. Piro, D. T. Simon, M.-C. Pham, V. Noël, and M. Berggren, "Detection of glutamate and acetylcholine with organic electrochemical transistors based on conducting polymer/platinum nanoparticle composites," *Adv. Mater.*, vol. 26, no. 32, pp. 5658–5664, 2014.

[137] C. Liao, C. Mak, M. Zhang, H. L. W. Chan, and F. Yan, "Flexible organic electrochemical transistors for highly selective enzyme biosensors and used for saliva testing," *Adv. Mater.*, vol. 27, no. 4, pp. 676–681, 2015.

[138] L. H. Jimison, S. A. Tria, D. Khodagholy, M. Gurfinkel, E. Lanzarini, A. Hama, G. G. Malliaras, and R. M. Owens, "Measurement of barrier tissue integrity with an organic electrochemical transistor," *Adv. Mater.*, vol. 24, no. 44, pp. 5919–5923, 2012.

[139] A. Campana, T. Cramer, D. T. Simon, M. Berggren, and F. Biscarini, "Electrocardiographic recording with conformable organic electrochemical transistor fabricated on resorbable bioscaffold," *Adv. Mater.*, vol. 26, no. 23, pp. 3874–3878, 2014.

[140] X. Strakosas, M. Bongo, and R. M. Owens, "The organic electrochemical transistor for biological applications," *J. Appl. Polym. Sci.*, vol. 132, no. 15, 2015.

[141] P. Leleux, J. Rivnay, T. Lonjaret, J.-M. Badier, C. Bénar, T. Hervé, P. Chauvel, and G. G. Malliaras, "Organic electrochemical transistors for clinical applications," *Adv. Healthcare Mater.*, vol. 4, no. 1, pp. 142–147, 2015.

[142] W. Salaneck, R. Friend, and J. Brédas, "Electronic structure of conjugated polymers: Consequences of electron-lattice coupling," *Phys. Rep.*, vol. 319, no. 6, pp. 231 – 251, 1999.

[143] L. Groenendaal, F. Jonas, D. Freitag, H. Pielartzik, and J. R. Reynolds, "Poly(3,4-ethylenedioxythiophene) and its derivatives: Past, present, and future," *Adv. Mater.*, vol. 12, no. 7, pp. 481–494, 2000.

[144] D. Nilsson, N. Robinson, M. Berggren, and R. Forchheimer, "Electrochemical logic circuits," *Adv. Mater.*, vol. 17, no. 3, pp. 353–358, 2005.

[145] N. Kim, H. Kang, J.-H. Lee, S. Kee, S. H. Lee, and K. Lee, "Highly conductive all-plastic electrodes fabricated using a novel chemically controlled transfer-printing method," *Adv. Mater.*, vol. 27, no. 14, pp. 2317–2323, 2015.

[146] A. Elschner, ed., *PEDOT - Principles and Application of a Intrinsic Conductive Polymer*. CRC Press, 2011.

[147] C. M. Palumbiny, C. Heller, C. J. Schaffer, V. Körstgens, G. Santoro, S. V. Roth, and P. Müller-Buschbaum, "Molecular reorientation and structural changes in cosolvent-treated highly conductive PEDOT:PSS electrodes for flexible indium tin oxide-free organic electronics," *J. Phys. Chem. C*, vol. 118, no. 25, pp. 13598–13606, 2014.

[148] D. Bernards and G. Malliaras, "Steady-state and transient behavior of organic electrochemical transistors," *Adv. Funct. Mater.*, vol. 17, no. 17, pp. 3538–3544, 2007.

[149] M. Sessolo, D. Khodagholy, J. Rivnay, F. Maddalena, M. Gleyzes, E. Steidl, B. Buisson, and G. G. Malliaras, "Easy-to-fabricate conducting polymer microelectrode arrays," *Adv. Mater.*, vol. 25, no. 15, pp. 2135–2139, 2013.

[150] I. Heller, S. Chatoor, J. Männik, M. A. G. Zevenbergen, J. B. Oostinga, A. F. Morpurgo, C. Dekker, and S. G. Lemay, "Charge noise in graphene transistors," *Nano Lett.*, vol. 10, no. 5, pp. 1563–1567, 2010.

[151] J. Männik, I. Heller, A. M. Janssens, S. G. Lemay, and C. Dekker, "Charge noise in liquid-gated single-wall carbon nanotube transistors," *Nano Lett.*, vol. 8, no. 2, pp. 685–688, 2008.

[152] P. Dutta and P. M. Horn, "Low-frequency fluctuations in solids: $\frac{1}{f}$ noise," *Rev. Mod. Phys.*, vol. 53, pp. 497–516, 1981.

[153] M. B. Weissman, "$\frac{1}{f}$ noise and other slow, nonexponential kinetics in condensed matter," *Rev. Mod. Phys.*, vol. 60, pp. 537–571, 1988.

[154] J. Tersoff, "Low-frequency noise in nanoscale ballistic transistors," *Nano Lett.*, vol. 7, no. 1, pp. 194–198, 2007.

[155] T. Sharf, J. W. Kevek, T. DeBorde, J. L. Wardini, and E. D. Minot, "Origins of charge noise in carbon nanotube field-effect transistor biosensors," *Nano Lett.*, vol. 12, no. 12, pp. 6380–6384, 2012.

[156] Z. Cheng, J. Hou, Q. Zhou, T. Li, H. Li, L. Yang, K. Jiang, C. Wang, Y. Li, and Y. Fang, "Sensitivity limits and scaling of bioelectronic graphene transducers," *Nano Lett.*, vol. 13, no. 6, pp. 2902–2907, 2013.

[157] Z. Cheng, Q. Li, Z. Li, Q. Zhou, and Y. Fang, "Suspended graphene sensors with improved signal and reduced noise," *Nano Lett.*, vol. 10, no. 5, pp. 1864–1868, 2010.

[158] J. Zhou, K. Ren, Y. Zheng, J. Su, Y. Zhao, D. Ryan, and H. Wu, "Fabrication of a microfluidic Ag/AgCl reference electrode and its application for portable and disposable electrochemical microchips," *ELECTROPHORESIS*, vol. 31, no. 18, pp. 3083–3089, 2010.

[159] T. Monteiro, S. Cardoso, L. Goncalves, and G. Minas, "PDMS encasing system for integrated lab-on-chip Ag/AgCl reference electrodes," in *Bioengineering (ENBENG), 2015 IEEE 4th Portuguese Meeting on*, pp. 1–4, 2015.

[160] E. Salm, Y. Zhong, B. Reddy, C. Duarte-Guevara, V. Swaminathan, Y.-S. Liu, and R. Bashir, "Electrical detection of nucleic acid amplification using an on-chip quasi-reference electrode and a PVC REFET," *Anal. Chem.*, vol. 86, no. 14, pp. 6968–6975, 2014.

[161] L.-L. Chi, J.-C. Chou, W.-Y. Chung, T.-P. Sun, and S.-K. Hsiung, "Study on extended gate field effect transistor with tin oxide sensing membrane," *Mater. Chem. Phys.*, vol. 63, no. 1, pp. 19 – 23, 2000.

[162] L.-T. Yin, J.-C. Chou, W.-Y. Chung, T.-P. Sun, and S.-K. Hsiung, "Study of indium tin oxide thin film for separative extended gate ISFET," *Mater. Chem. Phys.*, vol. 70, no. 1, pp. 12 – 16, 2001.

[163] W. Guan, N. Rajan, X. Duan, and M. Reed, "Quantitative probing of surface charges at dielectric-electrolyte interfaces.," *Lab Chip*, vol. 13, no. 7, pp. 1431–1436, 2013.

[164] A. Das, D. H. Ko, C.-H. Chen, L.-B. Chang, C.-S. Lai, F.-C. Chu, L. Chow, and R.-M. Lin, "Highly sensitive palladium oxide thin film extended gate FETs as pH sensor," *Sens. Actuators, B*, vol. 205, pp. 199 – 205, 2014.

[165] T. C. Nguyen, M. Schwartz, X. T. Vu, J. Blinn, and S. Ingebrandt, "Handheld readout system for field-effect transistor biosensor arrays for label-free detection of biomolecules," *Phys. Status Solidi A*, vol. 212, no. 6, pp. 1313–1319, 2015.

[166] X. Vu, R. GhoshMoulick, J. Eschermann, R. Stockmann, A. Offen-häusser, and S. Ingebrandt, "Fabrication and application of silicon nanowire transistor arrays for biomolecular detection," *Sens. Actuators, B*, vol. 144, no. 2, pp. 354 – 360, 2010.

[167] W. Fu, C. Nef, O. Knopfmacher, A. Tarasov, M. Weiss, M. Calame, and C. Schönenberger, "Graphene transistors are insensitive to pH changes in solution," *Nano Lett.*, vol. 11, no. 9, pp. 3597–3600, 2011.

[168] W. Fu, C. Nef, A. Tarasov, M. Wipf, R. Stoop, O. Knopfmacher, M. Weiss, M. Calame, and C. Schönenberger, "High mobility graphene ion-sensitive field-effect transistors by noncovalent functionalization," *Nanoscale*, vol. 5, pp. 12104–12110, 2013.

Appendix A

Fabrication Protocols

The fabrication protocol is adapted from the PhD thesis of Kristine Bedner[49] and Mathias Wipf[7].

Device Fabrication

SOI wafer characteristics

Wafer:	8" silicon-on-insulator (SOI)
Supplier:	SOITEC France
Device layer:	
Orientation:	(100)
Dopant:	p-type, boron
Resistivity:	$8.5 - 11.5\,\Omega$cm
Thickness:	$88\,$nm
Buried oxide (SiO$_2$)	
Thickness:	$145\,$nm
Silicon handle wafer:	
Type:	CZ, p-type
Resistivity:	$8 - 22\,\Omega$cm
Thickness:	$725\,\mu$m

Thinning

- 1. Sample cleaning

- Piranha solution: H_2O_2:H_2SO_4 - 2 : 1, for 10 min at 95°C

- HF dip

2. Thermal oxidation of silicon device layer to grow a 10 nm oxide mask for TMAH etching

Alignment marker fabrication

- 1. Spin coating:
  PMMA 672.11, 1500 rpm, thickness $\approx 3\,\mu$m
  Bake on hotplate for 5 min at 175°C
  Gradual cooling of the sample to avoid cracks in PMMA

  2. Electron-beam lithography: Vistec EBPG 5000$^+$
  Resolution = $0.03\,\mu$m, beam step size = $0.03\,\mu$m
  Beam current = 150 nA, dose = $1000\,\mu$C/cm^2
  Marker size: $10\,\mu$m × $10\,\mu$m

  3. Development: Hamatech
  IPA:MIBK - 3 : 1, 2 min, rinse in IPA 30 s

  4. Reactive ion etching (RIE): Oxford RIE 100

     - *Top SiO$_2$:* CHF$_3$ 12 sccm, Ar 38 sccm, 30 mTorr, 100 W, 300 K, V_{DC} = 485 V for 2 min

     - *Device Si layer:* CHF$_3$ 12 sccm, SF$_6$ 4 sccm, O$_2$ 3 sccm, 50 mTorr, 100 W, 300 K, V_{DC} = 365 V for 5 min

     - *Buried SiO$_2$:* CHF$_3$ 12 sccm, Ar 38 sccm, 30 mTorr, 100 W, 300 K, V_{DC} = 485 V for 8 min

     - *Si handle wafer:* CHF$_3$ 30 sccm, SF$_6$ 30 sccm, O$_2$ 2 sccm, 50 mTorr, 100 W, 300 K, V_{DC} = 365 V for 21 min

     - Resulting alignment marker depth: $\approx 1\,\mu$m

  5. Sample cleaning: Remove PMMA in acetone and then in Piranha solution H_2O:H_2SO_4 - 2 : 1 for 10 min at 95°C Piranha

Electron-beam lithography: Device pattern

- 1. Spin coating:
  Ti primer, 4000 rpm, bake for 1 min at 110°C
  nLOF:EBR : 4, 4000 rpm, bake for 1 min at 110°C

2. Exposure:

   - *SiNWs:* Resolution = $0.005\,\mu$m, beam step size = $0.005\,\mu$m, beam current $2\,$nA, dose $180\,\mu$C/cm^2

   - *Large structures:* Resolution = $0.005\,\mu$m, beam step size = $0.03\,\mu$m, beam current $50\,$nA, dose $165\,\mu$C/cm^2

3. Post exposure bake: $1\,$min at 110°C

4. Development: AZ MIF 826 for $25\,$s, rinse in DI-water

Device etching

- 1. RIE etching of SiO$_2$ top oxide: Oxford RIE 100; CHF$_3$ $12\,$sccm, Ar $38\,$sccm, $30\,$mTorr, $100\,$W, $300\,$K, $V_{DC} = 485\,$V for $27\,$s

  2. Buffered HF dip to remove remaining oxide

  3. Chemical wet etching of Si device layer: Tetramethylammonium hydroxide (TMAH) and IPA ($10\,$vol%) for $2\,$min at 45°C

  4. Sample cleaning: Piranha solution H$_2$O$_2$:H$_2$SO$_4$ $2:1$ for $10\,$min at 95°C

Contact fabrication I

- 1. Spin coating PMMA 672.08, 3000 rpm, bake for $30\,$min at 175°C, gradual cooling of the sample

  2. Electron-beam lithography: Vistec EBPG 5000$^+$

     - *SiNWs:* Resolution = $0.005\,\mu$m, beam step size = $0.005\,\mu$m, beam current $2\,$nA, dose $850\,\mu$C/cm^2

     - *Large structures:* Resolution = $0.005\,\mu$m, beam step size = $0.03\,\mu$m, beam current $190\,$nA, dose $850\,\mu$C/cm^2

  3. Development: Hamatech; IPA:MIBK $3:1$ $2\,$min, rinse in IPA $30\,$s

  4. Ion implantation at Ion Beam Services (IBS), Peynier, France; BF$_2^+$, energy = $43\,$keV, dose = $2.3 \cdot 10^{15}\,$cm^{-2}

  5. Removal of PMMA implantation mask in acetone

  6. Sample cleaning: RIE O$_2$, $40\,$sccm, $200\,$mTorr, $30\,$W, afterwards Piranha solution

7. Thermal activation of dopants: PPC Process Product Corporation annealing oven; annealing for 6 min at 950°C in forming gas and N_2

RCA cleaning and ALD deposition

- 1. Piranha solution H_2O_2:H_2SO_4 2 : 1 for 10 min at 95°C

  2. Buffered HF for 35 s to remove thermal top oxide layer

  3. RCA 1 cleaning: H_2O:H_2O_2:NH_4OH 20 : 4 : 1 for 10 min at 65°C

  4. Buffered HF dip

  5. RCA 2 cleaning: H_2O:H_2O_2:HCl 20 : 1 : 1 for 10 min at 65°C

  6. Atomic layer deposition (ALD) at 225°C for Al_2O_3 and at 200°C for HfO_2

Contact fabrication II

- 1. Dehydration bake for 10 min at 200°C

  2. Spin coating: HMDS, 4000 rpm, bake for 1 min at 110°C

  3. Optical lithography: Karl Süss MJB 3, 6 s

  4. Development: AZ MIF 826 for 80 s

  5. Opening of the contact window in the gate oxide:
     - Al_2O_3 200 deposition cycles: Buffered HF 35 s
     - HfO_2 200 deposition cycles: Buffered HF ≈ 5 min

  6. Metallization by electron beam evaporation (BAK 600), AlSi (1 %) 300 nm

  7. Lift-off in n-methyl-2-pyrrolidon (NMP) at room temperature

  8. Annealing of contact metal and ALD oxide: Annealing for 10 min at 450°C in forming gas

SU-8 protection layer and liquid opening

- 1. Dehydration bake for 10 min at 200°C

  2. Spin coating: SU-8 2002, 4000 rpm, bake 1 min at 95°C

  3. Optical lithography, 18 s

4. Post exposure bake: 1 min at 110°C

5. Development: EC 11 90 s, rinse in IPA

6. Hard bake of SU-8 on hotplate: Bake sample for 25 min at 180°C, gradual cooling of the sample

Dicing

- 1. Spin coating of microposit S1813, 1000 rpm, bake 2 min at 110°C

  2. Sawing: Disco DAT 341 or Esec 8003, sample size 9 mm × 9 mm

  3. Removal of resist with acetone

Packaging

- 1. Scratch back side of the sample with diamond scriber, glue the sample in 64 pin chip carrier (IPK64F1-2219A, NTK Technologies Inc.) by silver epoxy

  2. Aluminum wire wedge bonding: MEI Marpet Enterprises Inc

  3. PDMS microchannel
     - Mix polydimethylsiloxane (PDMS, *SYLGARD 184 Silicone Elastomer*) with curing agent (10 : 1)
     - Pour PDMS onto SU-8 patterned Si wafers, keep at room temperature for ≈ 1 h until all the bubbles have cleared
     - Heating at 60°C for 2 h.
     - Pierce inlets with *Harris Uni-Core* 0.75 mm for tubing
     - Cut PDMS with razor blade and align to sample

  4. Epoxy sealing: Epotek 353ND, degas, bake for 5 min at 120°C

  5. Tubing: Polytetrafluoroethylene (PTFE) 0.3 mm ID × 0.76 mm OD

Au-film for gold-coated SiNWs

1. Spin coating:
   - O_2 plasma: RIE O_2, 40 sccm, 200 mTorr, 30 W, 300 K, $V_{DC} = 87$ V, 8 s

- Spin coating of PMMA 669.04, 6000 rpm, thickness $\approx 220\,\mathrm{nm}$
- Bake on hotplate for 3 min at 175°C

2. Electron-beam lithography: Vistec EBPG 5000$^+$, resolution = $0.01\,\mu\mathrm{m}$, beam step size = $0.01\,\mu\mathrm{m}$, beam current 2 nA, dose $850\,\mu\mathrm{C/cm}^2$

3. Development: Hamatech, IPA:MIBK 3 : 1, 2 min, rinse in IPA 65 s
   O$_2$ plasma: O$_2$ 40 sccm, 200 mTorr, 30 W, 300 K, $V_{DC} = 87\,\mathrm{V}$, 8 s

4. Metal evaporation: Electron-beam evaporation with UNIVEX, Cr 5 nm, Au 20 nm

5. Lift-off in acetone for several hours

SU-8 structures for PDMS microchannels

1. Clean oxidized Si wafer in DI water, acetone, IPA

2. Dehydration bake for 10 min at 200°C

3. Spin coating: SU-8 50 (1250 rpm for $100\,\mu\mathrm{m}$ and 2000 rpm for $50\,\mu\mathrm{m}$ thick layers), bake 10 min at 65°C

4. Electron-beam lithography: Vistec EBPG 5000$^+$, resolution = $0.05\,\mu\mathrm{m}$, beam step size = $0.05\,\mu\mathrm{m}$, beam current = 1 nA, dose = $5\,\mu\mathrm{C/cm}^2$

5. Post exposure bake: 90 s at 110°C

6. Development: EC 11 12 min, rinse in IPA

7. Hard bake of SU-8 on hotplate: Bake sample for 20 min at 180°C, gradual cooling of the sample

Appendix B

Salt Response of Gold-Coated NWs at Different pH

Figure B.1 shows the response to $CaCl_2$ from $1\,mM$ to $1\,M$ of a $25\,\mu m$-wide gold-coated NW at pH 3, pH 7 and pH 10. For all three pH values, the curves shift to more positive threshold voltages with increasing electrolyte concentration. Similar results were obtained for Al_2O_3 and HfO_2 as discussed in a previous work[53]. The shift indicates adsorption of negative charge. Since pH is constant, the adsorption of Cl^- ions is proposed. However, the same response is obtained using other anions, such as fluoride F^-. Although the microscopic picture of this adsorption process is not fully understood, Figure B.1 clearly demonstrates that the shift due to changes in background electrolyte concentration does not depend on the pH and therefore the surface potential. We refer to this response as a linear effect which can be taken into account by a differential measurement. Thereby, we assume that the unspecific response to changes in the electrolyte concentration is the same for the active as for the control NWs. However, this is only a meaningful approximation if the unspecific background response does not depend on the surface potential as indeed observed experimentally.
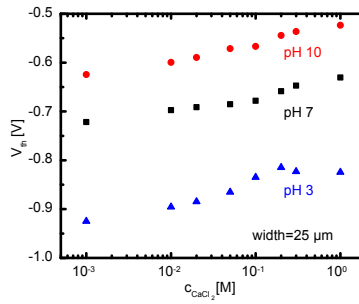
Figure B.1: Threshold voltage V_{th} versus background electrolyte concentration $c_{\mathbf{CaCl_2}}$ for a $25\,\mu$m-wide nanowire.

Appendix C

Competing Surface Reactions and FimH Detection

In Figure 4.3c, theoretical curves of the change in surface potential $-\Delta\Psi_0$ due to FimH adsorption for two NWs of different pH sensitivities are shown. The curves are based on the following FimH adsorption model including the competing effect of pH: Besides the ligands immobilized on the surface, additional hydroxyl groups (MOH) are assumed due to the residual pH response of the gold surface[83]. Analyte ([A], FimH protein) adsorption, as well as deprotonation and protonation of MOH change the surface charge and hence the surface potential. The system can be described by three equilibrations[63]:

$$
\begin{aligned}
\text{MOH} &\rightleftharpoons \text{MO}^- + \text{H}^+,\ K_a \\
\text{MOH}_2^+ &\rightleftharpoons \text{MOH} + \text{H}^+,\ K_b \\
[\text{AB}] &\rightleftharpoons [\text{A}] + [\text{B}],\ K_D.
\end{aligned}
\tag{C.1}
$$
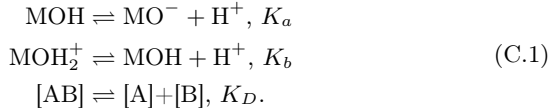
K_a, K_b and K_D are the equilibrium dissociation constants. [A] is the analyte concentration, [B] is the number of free ligands per unit area. The surface potential is related to the surface charge by: $\Psi_0 = \sigma_0 / C_{dl}^{\square}$ where σ_0 is the total number of surface charge per unit area and $C_{dl}^{\square}$ is the double layer capacitance per unit area. Including the Boltzmann distribution for the proton activity, $a_{H_s^+} = a_{H^+} \exp(-e\Psi_0/kT)$, with e as elementary charge, k the Boltzmann constant and T as absolute temperature, we get

$$
\Psi_0 = \frac{q_A}{C_{dl}^{\square}} [\text{B}]_0 \frac{[\text{A}]}{[\text{A}] + K_D} + \frac{e}{C_{dl}^{\square}} N_s \frac{a_{\text{H}^+}^2 - K_a K_b e^{-e\Psi_0/kT}}{a_{\text{H}^+}^2 + a_{\text{H}^+} K_b e^{e\Psi_0/kT} + K_a K_b e^{2e\Psi_0/kT}},
\tag{C.2}
$$

where the first term is given by the protein adsorption with q_A being the charge per protein and $[B]_0$ being the total number of surface bound ligands per unit area. For simplicity a uniform distribution of surface and bulk proteins can be assumed, since the protein size is larger as the Debye length. The second term describes the intrinsic proton sensitivity.

Appendix D

Bias Dependence of $1/f$ Noise of PEDOT:PSS OECTs

$1/f$ noise caused by resistance fluctuations is characterized by the fact that it can be measured as voltage fluctuations when a constant current is passed through the sample or as current fluctuations when a constant bias voltage is applied [66]:

$$\frac{S_V}{V_{sd}^2} = \frac{S_{Isd}}{I_{sd}^2} = \frac{S_R}{R^2} = \frac{S_G}{G^2} = \frac{C}{f} \tag{D.1}$$

where S_V, S_{Isd}, S_R, S_G, are the voltage, current, resistance and conductance noise power spectral densities. C is a quantity of the noise of the sample and is constant for an ohmic sample of a fixed resistance R. The right hand side of the above equation with the term C/f was proposed by Hooge who also redefined C using the number of fluctuators N and Hooge's parameter α_H: $C = \alpha_H/N$. As long as the number of fluctuators is kept constant, Hooge's law predicts $S_V \propto V_{sd}^2$, $S_{Isd} \propto I_{sd}^2$ which has been confirmed experimentally [66]. Therefore, the proportionality of $S_V \propto V_{sd}^2$ or $S_{Isd} \propto I_{sd}^2$ is commonly used to demonstrate that the observed noise is caused by resistance fluctuations. For a transistor, where the resistance of the device can be adjusted via the gate, the same bias dependence is observed if the transistor is gated to a fixed resistance value by applying a constant gate voltage V_{ref} at the gate electrode. Figure D.1a shows the same schematic of the noise measurement setup as described in Figure 6.1a. Figure D.1b shows the scaling of the voltage noise S_V versus V_{sd} of a 25 μm x 25 μm OECT ($d = 100$ nm) gated to a resistance value of 675 kΩ. As expected for resistance fluctuations, we find $S_V \propto V_{sd}^2$ which demonstrates that the observed noise originates from resistance fluctuations. In other

words, the applied source-drain voltage does not generate the noise, but allows measuring it[66].
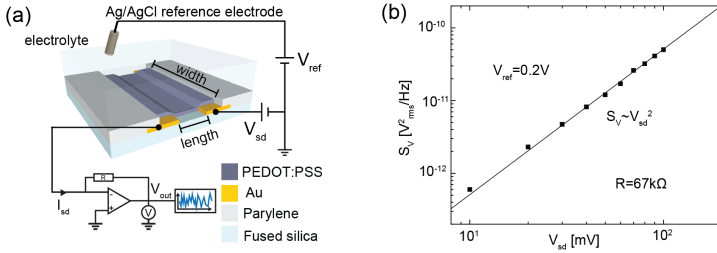
Figure D.1: (a) Schematic of the noise measurement setup identical to the setup shown in Figure 6.1a. (b) Voltage noise S_V versus source-drain voltage V_{sd} for a $25\,\mu$m x $25\,\mu$m OECT gated to a resistance value of $R = 67\,$kΩ. Clearly, S_V scales with V_{sd}^2 demonstrating that the observed noise is caused by resistance fluctuations.

Publication List

Peer-Reviewed Journal Publications

1. J. Kupec, R. L. Stoop and B. Witzigmann. Light Absorption and Emission in Nanowire Array Solar Cells. *Opt. Express 18*, 27589–27605 (2010)

2. A. Tarasov, M. Wipf, K. Bedner, J. Kurz, W. Fu, V.A. Guzenko, O. Knopfmacher, R. L. Stoop, M. Calame and C. Schönenberger. True Reference Nanosensor Realized with Silicon Nanowires. *Langmuir 28*, 9899–9905 (2012)

3. A.Tarasov, M. Wipf, R. L. Stoop, K. Bedner, W. Fu, V. A. Guzenko, O. Knopfmacher, M. Calame and C. Schönenberger. Understanding the Electrolyte Background for Biochemical Sensing with Ion-Sensitive Field-Effect Transistors. *ACS Nano 6*, 9291–9298 (2012)

4. R. L. Stoop, V. Saase, C. Wagner, B. Stoop and R. Stoop. Beyond Scale-Free Small-World Networks: Cortical Columns for Quick Brains. *Phys. Rev. Lett. 110*, 108105 (2013)

5. K. Bedner, V. A. Guzenko, A. Tarasov, M. Wipf, R. L. Stoop, D. Just, S. Rigante, W. Fu, R. A. Minamisawa, C. David, M. Calame, J. Gobrecht and C. Schönenberger. pH Response of Silicon Nanowire Sensors: Impact of Nanowire Width and Gate Oxide. *Sens. Mater. 25*, 567–576 (2013)

6. M. Wipf, R. L. Stoop, A. Tarasov, K. Bedner, W. Fu, I. A. Wright, C. J. Martin, E. C. Constable, M. Calame and C. Schönenberger. Selective Sodium Sensing with Gold-Coated Silicon Nanowire Field-Effect Transistors in a Differential Setup. *ACS Nano 7*, 5978–5983 (2013)

7. R. Stoop, P. Nüesch, R. L. Stoop and L. A. Bunimovich. At Grammatical Faculty of Language, Flies Outsmart Men. *PLOS One 8*,

e70284 (2013)

8. W. Fu, C. Nef, A. Tarasov, M. Wipf, R. L. Stoop, O. Knopfmacher, M. Weiss, M. Calame and C. Schönenberger. High mobility graphene ion-sensitive field-effect transistors by noncovalent functionalization. *Nanoscale 5*, 12104–12110 (2013)

9. K. Bedner, V. A. Guzenko, A. Tarasov, M. Wipf, R. L. Stoop, S. Rigante, J. Brunner, W. Fu, C. David, M. Calame, J. Gobrecht and C. Schönenberger. Investigation of the dominant 1/f noise source in silicon nanowire sensors. *Sens. Actuators, B 191*, 270 – 275 (2014)

10. F. Gomez, R. L. Stoop and R. Stoop. Universal dynamical properties preclude standard clustering in a large class of biochemical data. *Bioinformatics 30*, 2486–2493 (2014)

11. P. Livi, A. Shadmani, M. Wipf, R. L. Stoop, J. Rothe, Y. Chen, M. Calame, C. Schönenberger and A. Hierlemann. Sensor System including Silicon Nanowire Ion Sensitive FET Arrays and CMOS readout. *Sens. Actuators, B 204*, 568–577 (2014)

12. S. Rigante, P. Scarbolo, M. Wipf, R. L. Stoop, K. Bedner, E. Buitrago, A. Bazigos, D. Bouvet, M. Calame, C. Schönenberger and A. M. Ionescu. Sensing with Advanced Computing Technology: Fin Field-Effect Transistors with High-k Gate Stack on Bulk Silicon. *ACS Nano 9*, 4872–4881 (2015)

13. R. L. Stoop, M. Wipf, S. Müller, K. Bedner, I. A. Wrigth, C. J. Martin, E. C. Constable, W. Fu, M. Calame and C. Schönenberger. Competing Surface Reactions Limiting the Performance of Ion-Sensitive Field-Effect Transistors. *Sens. Actuators, B 220*, 500-507 (2015)

14. M. Wipf, R. L. Stoop, G. Navarra, S. Rabbani, B. Ernst, K. Bedner, C. Schönenberger and M. Calame. Label-Free FimH Protein Interaction Analysis Using Silicon Nanoribbon BioFETs. *submitted*

Conference Proceedings

1. W. Fu, C. Nef, A. Tarasov, M. Wipf, R. L. Stoop, O. Knopfmacher, M. Weiss, M. Calame and C. Schönenberger. Sensing with Liquid-Gated Graphene Field-Effect Transistors. Conference on Nanotechnology *(12th IEEE-NANO)*. 2012; pp 1–2

2. M. Wipf, R. L. Stoop, A. Tarasov, K. Bedner, W. Fu, M. Calame and C. Schönenberger. Potassium Sensing with Membrane-Coated Silicon

Nanowire Field-Effect Transistors. *Transducers Eurosensors XXVII:* The 17th International Conference on Solid-State Sensors, Actuators and Microsystems. 2013; pp 1182–1185

3. S. Rigante, M. Wipf, A. Tarasov, D. Bouvet, K. Bedner, R. L. Stoop and A. Ionescu. Integrated FinFET Based Sensing in a Liquid Environment. *Transducers Eurosensors XXVII:* The 17th International Conference on Solid-State Sensors, Actuators and Microsystems. 2013; pp 681–684

4. P. Livi, M. Wipf, A. Tarasov, R. L. Stoop, K. Bedner, J. Rothe, Y. Chen, A. Stettler, C. Schönenberger and A. Hierlemann. Silicon Nanowire Ion-Sensitive Field-Effect Transistor Array Integrated with a CMOS-based readout chip. *Transducers Eurosensors XXVII:* The 17th International Conference on Solid-State Sensors, Actuators and Microsystems. 2013; pp 1751–1754

Talks

1. R. L. Stoop, M. Wipf, A. Tarasov, K. Bedner, W. Fu, M. Calame and C. Schönenberger. Chemical sensing with silicon nanowire field-effect transistors. *Annual Meeting of the Swiss Physical Society.* 2012

2. R. L. Stoop, M. Wipf, A. Tarasov, K. Bedner, W. Fu, M. Calame and C. Schönenberger. Silicon Nanowire Field-Effect Transistors for Sensing Applications. *Complex Systems Conference.* 2012

3. R. L. Stoop, M. Wipf, A. Tarasov, K. Bedner, J. Kurz, W. Fu, M. Calame and C. Schönenberger. Sensing with Silicon Nanowire Field-Effect Transistors. *Eurosensors 12 Conference.* 2012

4. R. L. Stoop, M. Wipf, A. Tarasov, K. Bedner, W. Fu, M. Calame and C. Schönenberger. Sensing with Silicon Nanowire Field-Effect Transistors. *Spring Meeting of the European Materials Research Society 13.* 2013

5. R. L. Stoop, M. Wipf, A. Tarasov, K. Bedner, W. Fu, M. Calame and C. Schönenberger. Biochemical Sensors Based on Silicon Nanowire Transistors. *Annual Meeting of the Swiss Nanoscience Institute.* 2014

6. R. L. Stoop, M. Wipf, A. Tarasov, K. Bedner, W. Fu, M. Calame and C. Schönenberger. Sensing with Silicon Nanowire Field-Effect Transistors. *40th Conference on Micro- and Nano Engineering.* 2014

7. R. L. Stoop. Was ist Nano? *Berufswahlschule Bülach.* 2014

8. R. L. Stoop, M. Wipf, A. Tarasov, K. Bedner, W. Fu, C. Schönenberger and M. Calame. Arrays of Silicon Nanowire Field-Effect Transistors for Biochemical Sensing. *Lunch Meeting of the NCCR Molecular Systems Engineering.* 2015

Poster Contributions

1. R. L. Stoop, M. Wipf, A. Tarasov, K. Bedner, W. Fu, M. Calame and C. Schönenberger. Silicon Nanowire Field-Effect Transistors for Specific Ion Sensing. *Swiss Nanoconvention.* 2013

2. R. L. Stoop, M. Wipf, A. Tarasov, K. Bedner, W. Fu, M. Calame and C. Schönenberger. The Essential Requirements of ISFET Sensors for Biochemical Sensing. *Swiss Nanoconvention.* 2014

3. R. L. Stoop, A. Fanget, M. Wipf, S. Müller, E. C. Constable, G. Navarra, B. Ernst, C. Schönenberger and M. Calame. Biochemical Sensing Based on an ISFET Platform. *Annual Meeting of the NCCR Molecular Systems Engineering.* 2015

Curriculum Vitae

Date of birth	February 6, 1986
Place of birth	Winterthur, Switzerland
Nationality	Swiss
Hometown	Schänis (SG), Switzerland
Family status	Single

━━━ Education

10/2011– **PhD in Experimental Physics**, *Nanoelectronics Group (Prof. Dr. Christian*
10/2015 *Schönenberger)*, Department of Physics, University of Basel, Switzerland.
Topic: Understanding silicon nanowire field-effect transistors for biochemical sensing

09/2008– **MSc ETH in Electrical Engineering and Information Technology**, *ETH Zurich*,
03/2011 Switzerland.

01/2009- **Exchange Studies in Applied Physics**, *Lund University*, Sweden.
07/2009

10/2004– **BSc ETH in Electrical Engineering and Information Technology**, *ETH Zurich*,
08/2008 Switzerland.

08/2000– **Matura**, *Kantonsschule Büelrain*, Winterthur, Switzerland.
09/2004

━━━ Professional Experience

10/2011– **Research and Teaching Assistant**, *Department of Physics, University of Basel*,
10/2015 Switzerland.
Nanostructured biochemical sensors, ion-sensitive field-effect transistors, organic transistors

02/2011– **Research Assistant**, *Institute of Neuroinformatics, University of Zurich*,
09/2011 Switzerland.
Dynamical systems theory, neural networks

01/2010– **Internship**, *Sensirion AG, Stäfa*, Switzerland.
05/2010 Benchmarking of humidity sensors

06/2009– **Internship**, *Institute for Building Materials, ETH Zurich*, Switzerland.
08/2009 Numerical simulations and data analysis

Acknowledgements

versity of Valencia, Michele Sessolo and Henk Bolink. Michele, it was a great pleasure to stay in the lab until the next morning during your visit! Furthermore, I would like to thank Nicolas Clément and Sven Ingebrandt for reviewing my thesis.

Every day I had a lot of fun with the people from office 0.23: 'Sweet' Maria El Abbassi whose big appetite for chocolate is only surpassed by her incredible negotiation skills. Jan Overbeck for his help and his great enthusiasm for an after work beer. Kishan Thodkar for the many jokes and good laughs that we had. Anton Vladyka for sharing all pictures of his travels with us (and google) and his unique personality. Cornelia Nef for the weekly train rides back to eastern Switzerland. Toni Fröhlich for the cross-country skiing events and Jan Brunner for countless discussions. And Oliver Braun for representing Switzerland in the office in the best possible way: Open-minded, helpful and funny.

I further would like to thank all members of the nanoelectronics group who made the numerous group workshops, excursions and skiings so enjoyable: Andreas Baumgartner, Claire Barrett, Minkyung Jung, Romain Maurand, Péter Makk, Markus Weiss, Gulibusitan Abulizi, Samuel d'Hollosy, Gabor Fabian, Frank Freitag, Jörg Gramich, Clevin Handschin, Mihai-Cezar Harabula, Thomas Hasler, Jan Mayer, Stefan Nau, Vishal Ranjan, Peter Rickhaus, Christian Jünger, Julia Samm, Jens Schindele, Samuel Vogel, Lujun Wang and Simon Zihlmann. I would also like to thank the technical staff Heinz Breitenstein, Sascha Martin, Daniel Sacker and Michael Steinacher. Our secretaries Barbara Kammermann and Astrid Kalt for taking care of all administrative things and their kind help.

Last but not least, I would like to thank my family who always believed in me and for having good times whenever we meet. And of course you Nana, for all your patience and for being such a wonderful person.